Alma Mater Studiorum · University of Bologna

School of Science
Department of Physics and Astronomy
Master Degree in Physics

Improving track reconstruction in the ICARUS detector

Supervisor:
Dr. Gabriele Sirri

Co-supervisor:
Dr. Francesco Poppi
Dr. Laura Pasqualini

Submitted by:
Marco Scarnera

Academic Year 2023/2024

Abstract

The Short-Baseline Neutrino (SBN) program at Fermilab investigates anomalies that deviate from the standard three-neutrino oscillation model, suggesting a possible sterile neutrino. The ICARUS detector, located at the SBN far site 600 m from the Booster Neutrino Beam proton target, comprises three subsystems: a 470 t Liquid Argon Time Projection Chamber (LArTPC), a photon detection system in LAr, and a Cosmic Ray Tagger (CRT) based on scintillators.

This thesis focuses on calibrating the Top CRT and enhancing track reconstruction in the TPC. The CRT calibration aims to ensure uniform detector response by estimating and equalizing pedestal and gain values for each CRT channel, maintaining consistent performance over time. Enhancing track reconstruction accuracy in the TPC addresses issues where single particle trajectories are mistakenly segmented into multiple tracks. A track stitching algorithm was developed and validated through Monte Carlo simulations to improve track reconstruction accuracy and momentum estimation.

The analysis showed that applying a 20-degree collinearity cut in the algorithm optimizes momentum estimation, significantly reducing bias (up to 15%) and slightly improving resolution ($\tilde{1}$%) for about 10% of the track sample.

Contents

Introduction

Since the mid-1990s, several neutrino experiments at short baselines have observed anomalies in their data that deviate from the predictions made by the standard three-neutrino model: the Reactor Neutrino Anomaly, the Gallium Anomaly, the LSND Anomaly, MiniBooNE's Low-Energy Excess, and the more recently identified Neutrino-4 Anomaly. This disagreement from expected results suggest the possible existence of a sterile neutrino, which does not participate in the standard weak interactions, and their only interaction is gravitational.

To investigate these anomalies, the Short-Baseline Neutrino (SBN) program at Fermilab uses three Liquid Argon Time Projection Chambers (LArTPCs): SBND, MicroBooNE, and ICARUS. Located along the 0.8 GeV muon neutrino Booster Neutrino Beamline (BNB), these detectors are strategically placed to measure ν_μ to ν_e neutrino oscillations and explore the potential existence of sterile neutrinos at the eV mass-scale, testing neutrino oscillations at short baselines where these anomalies have been previously observed.

The far detector, ICARUS-T600, has an active mass of 476 tons and is located 600 meters from the BNB proton target. ICARUS is the only detector in the SBN program currently taking data. The experiment, in a standalone physics program, is exploring the potential presence of a Neutrino-4 oscillation signal that should be visible by ICARUS in both ν_μ and ν_e disappearance channels. For this oscillation analysis, measuring the neutrino energy and its flavor is crucial.

Situated just below the surface, the ICARUS detector is subject to a large flux of cosmic particles, which may induce several additional and uncorrelated triggers during the $\sim$1 ms drift time. On average, $\sim$11 cosmic tracks are expected over the full T600 volume during the drift time window, creating a background that must be disentangled from the neutrino event tracks. To mitigate this cosmogenic induced background, ICARUS is surrounded by an external Cosmic Ray Tagger (CRT) system divided into three subsystems: Bottom, Side, and Top, below a 3 m concrete overburden (6 m water equivalent).

The ICARUS detector is designed to identify and analyze both neutrino and cosmic ray interactions using data collected from the TPC, PMT, and CRT subsystems. The TPC is crucial for reconstructing events, utilizing topological and calorimetric information to create three-dimensional track and shower objects, identifying and characterizing the particles involved.

As part of this thesis work, I first focused on the calibration of the Top CRT. The primary objective of the calibration analysis was to estimate the pedestal and gain values of each Top CRT channel, to monitor and equalize the detector response over time.

After this, the thesis work concentrated on improving track reconstruction inside the TPC. Hardware-related issues and inefficiencies at the reconstruction level can compromise the accuracy of event reconstruction, leading to single particle trajectories being erroneously segmented into multiple tracks. This problem was analyzed for Monte Carlo simulated data, and a solution, the track stitching algorithm, was proposed to improve track reconstruction and momentum estimation.

The thesis is organized as follows: Chapter 1 introduces neutrino oscillation physics, focusing on the anomalies observed in several experiments. In Chapter 2 the Short-Baseline Neutrino Program is described, with an overview of the LArTPC technology and the SBN detectors. Chapter 3 provides a detailed overview of the ICARUS detector and its subsystems. The ICARUS Cosmic Ray Tagger is described in Chapter4, along with the methodology and results of the CRT calibration. Chapter 5 focuses on the event reconstruction in the TPC, with a description of the developed stitching algorithm to improve track reconstruction accuracy in the TPC.

Chapter 1

Neutrino oscillations and light sterile neutrinos

1.1 Introduction

In December 1930, W. Pauli postulated the existence of a neutral particle, today recognized as the *neutrino*. He introduced it as a "desperate remedy ... to save the law of conservation of energy", addressing the problem of the continuous spectrum observed in β-decays [1]. Enrico Fermi adopted Pauli's hypothesis to develop, in 1934, the theory of β-decay known as Fermi theory [2]. Fermi's model described the process as a 4-fermion interaction, with a direct coupling of the neutron with a proton, an electron and a neutrino, and suggested a new fundamental force characterized by the strength G_F. This theory also implied the potential for neutrino interactions with matter, via the inverse β-decay process $\overline{\nu}p \rightarrow ne^+$.

The first successful detection of antineutrinos in 1956 by F. Reines and C.L. Cowan at the Savannah River Plant in South Carolina [3, 4] confirmed this theory (see Figure 1.1). Prompted by Bruno Pontecorvo's early 1950s suggestion to use high neutrino fluxes for detection [5], their experiment was the first reactor-neutrino experiment. Reines was awarded with the Nobel Prize for the discovery in 1996.

Over the years, further experiments have improved our understanding of neutrinos' properties. In 1958 M.Goldhaber, L.Grodzins and A.W.Sunyar [6] demonstrated that neutrinos are polarized in the opposite direction to their motion, supporting the 1957 hypothesis by L. Landau, T.D. Lee, C.N. Yang, and A. Salam [7–9] that neutrinos could be described as left-handed Weyl spinors. These findings were later integrated into the V-A theory of weak interactions and ultimately into the Standard Model (SM) of particle

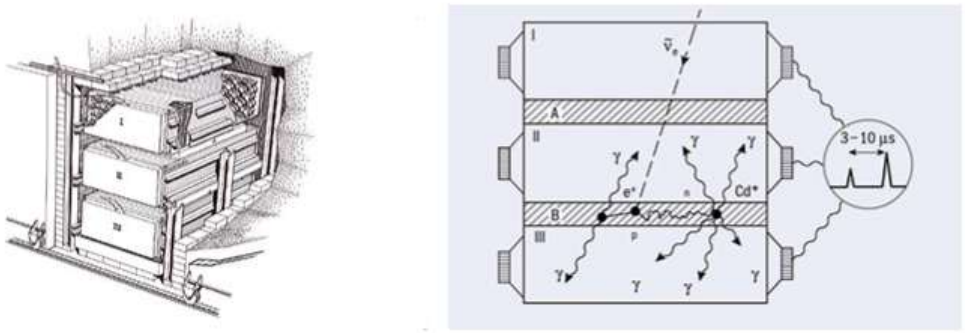

Figure 1.1: (Left) The Savannah River detector. Placed in a cavity about 11 m from the nuclear reactor core, it used two plastic tanks with 200 liters of water and 40 kg of dissolved $CdCl_2$ dissolved in it. The water tanks were positioned between three liquid scintillator tanks (1400 liters each). (Right) The $\overline{\nu}$ detection technique exploits the emission of a prompt scintillator signal due to positron annihilation and a second delayed signal due to the capture of the moderated neutron.

physics [10–12]. In 1963, Lederman, Schwartz, and Steinberg [13] identified at the Brookhaven National Laboratory, with the first accelerator neutrino experiment, a new type of neutrino distinct from the electron neutrino and associated with muons, thus known as the muon neutrino ν_μ. This discovery set the stage for classifying electron and muon neutrinos into distinct lepton families (or generations). The number of generations was fixed at three in 1989, following the analysis of the Z boson invisible width [14] by the Large Electron–Positron Collider (LEP) experiment at CERN (see Figure 1.2). A third neutrino, associated with the τ lepton, was indeed observed in 2000 by the DONUT experiment [15] at Fermilab, confirming the existence of the last lepton predicted by the SM. So far, no experiment has detected large deviations from the SM, except neutrino oscillation experiments, which have shown that neutrinos are massive and mixed. The answer to how neutrinos gain their small masses and how they are mixed must be found in the theory beyond the SM.

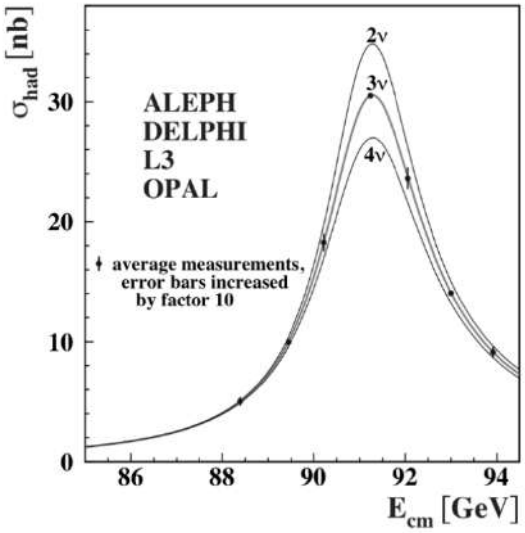

Figure 1.2: Measurement of the hadron production cross-section as a function of the LEP centre-of-mass energy around the Z-boson resonance. The curves on the graph represent the predictions based on the presence of two, three, and four neutrino species.

1.2 The Standard Electroweak Theory of leptons

1.2.1 The Standard Model

The Standard Model of particle physics is a gauge theory that describes, in the framework of quantum field theory, the strong, electromagnetic and weak interactions of elementary particles. It is based on the local symmetry group $SU(3)_C \otimes SU(2)_L \otimes U(1)_Y$, where the subscripts C, L, Y refer to the color charge, left-handed chirality and weak hypercharge, respectively. The $SU(3)_C$ gauge group describes the strong interactions, mediated by eight massless gluons g. The symmetry group $SU(2)_L \otimes U(1)_Y$ describes the electroweak sector of the SM, in which four gauge bosons are responsible for electroweak interactions: the three massive $W^{\pm}$, Z^0 bosons and the massless photon γ. The matter content of the SM is given in Table 1.1, where the elementary fermions (half-integer spin) are divided in two categories, quarks and leptons, both classified in three different generations [16]. In addition to these particles, the SM contains a scalar field associated with a spin-0 particle: the Higgs boson.

Particles	$SU(3)$	$SU(2)_L$	$U(1)_Y$
Leptons			
$\begin{pmatrix} \nu_e \\ e \end{pmatrix}_L, \begin{pmatrix} \nu_\mu \\ \mu \end{pmatrix}_L, \begin{pmatrix} \nu_\tau \\ \tau \end{pmatrix}_L$	1	2	-1/2
e_R, μ_R, τ_R	1	1	-1
Quarks			
$\begin{pmatrix} u \\ d \end{pmatrix}_L, \begin{pmatrix} c \\ s \end{pmatrix}_L, \begin{pmatrix} t \\ b \end{pmatrix}_L$	3	2	1/6
u_R, c_R, t_R	3	1	2/3
d_R, s_R, b_R	3	1	-1/3

Table 1.1: Representation of the fermionic content of the SM, with respect to the groups $SU(3)_C$, $SU(2)_L$, and $U(1)_Y$ [17].

The symmetry group, relevant to describe neutrino interactions in the SM, is in this case $SU(2)_L \otimes U(1)_Y$, where $SU(2)_L$ is called weak isospin and $U(1)_Y$ hypercharge. The subscript L indicates that the $SU(2)$ transformations operate only on the left-handed (LH) chiral components of the fermion fields (the right-handed chiral components are singlets under weak isospin transformations) [18]. Every four-component fermion field ψ can be split into its left and right chiral components: $\psi = \psi_L + \psi_R$, where $\psi_L \equiv P_L\psi = (1-\gamma_5)\psi/2$ and $\psi_R \equiv P_R\psi = (1+\gamma_5)\psi/2$ [19]. Following the notation used in [18], the left-handed chiral components of the lepton fields, grouped into weak isospin doublets, and the right-handed (RH) weak isospin singlets are then defined as

$$L'_{\alpha L} = \begin{pmatrix} \nu'_{\alpha L} \\ \ell'_{\alpha L} \end{pmatrix}, \quad \nu'_{\alpha R}, \quad \ell'_{\alpha R}. \tag{1.1}$$

In this notation the index α refers to the lepton flavours e, μ, τ. The leptonic electroweak SM Lagrangian is thus expressed as follows

$$\begin{aligned} \mathcal{L} = & \, i \sum_\alpha \overline{L'_{\alpha L}} \not{D} L'_{\alpha L} + i \sum_\alpha \overline{\ell'_{\alpha R}} \not{D} \ell'_{\alpha R} - \frac{1}{4} \underline{A}_{\mu\nu} \underline{A}^{\mu\nu} - \frac{1}{4} B_{\mu\nu} B^{\mu\nu} \\ & + (D^\rho \phi)^\dagger (D_\rho \phi) - \mu^2 \phi^\dagger \phi - |\lambda| (\phi^\dagger \phi)^2 \\ & - \sum_{\alpha,\beta=e,\mu,\tau} \left(Y'^{\ell}_{\alpha\beta} \overline{L'_{\alpha L}} \phi \ell'_{\beta R} + Y'^{\ell *}_{\alpha\beta} \overline{\ell'_{\beta R}} \phi L'_{\alpha L} \right). \end{aligned} \tag{1.2}$$

Within this equation the vector gauge boson fields weak $A^\mu_a (a = 1, 2, 3)$ and

hypercharge B^μ are introduced. These enter in the field-strength tensors $\underline{A}^{\mu\nu} \equiv (A_1^{\mu\nu}, A_2^{\mu\nu}, A_3^{\mu\nu})$ and $B^{\mu\nu}$ [16]. Before going to the next section, it is worth noting that the Lagrangian (1.2) does not include any right-handed components for neutrino fields. In the SM, it is assumed that neutrino fields exclusively consist of left-handed components. This assumption aligns with the two-component theory originally proposed by Landau [7], Lee and Yang [8], and Salam [9], which implies that neutrinos are massless and described by left-handed Weyl spinors.

1.2.2 Neutrinos in the Standard Model

As pointed out in Section 1.2.1, the Standard Model was developed as a gauge chiral theory, wherein neutrino fields have only the left-handed component $\nu_{\alpha L}$. Consequently, neutrinos remain massless, as the presence of the right-handed components $\nu_{\beta R}$ is necessary for the Dirac mass terms $\overline{\nu_{\alpha R}}\nu_{\beta L}$. In the Dirac Lagrangian describing the dynamics of free fermions, the mass term reads indeed

$$-m\overline{\psi}\psi = -m\left(\overline{\psi}_L\psi_R + \overline{\psi}_R\psi_L\right). \tag{1.3}$$

However this mass term is excluded in the SM, since it is not gauge invariant under the tranformations of $SU(2)_L \times U(1)_Y$, and charged fermion masses originate from the Brout-Englert-Higgs (BEH) mechanism [18]. Left-handed neutrinos interact via the weak force according to the charged current (CC) and neutral current (NC) terms in the SM Lagrangian [17]:

$$\begin{aligned}\mathcal{L}^{\nu}_{SM} &= \mathcal{L}^{(CC)}_{\nu,L} + \mathcal{L}^{(NC)}_{\nu,L} = -\frac{g}{2\sqrt{2}} j^{\mu}_{W,L} W_\mu - \frac{g}{2\cos\theta_W} j^{\mu}_{Z,\nu L} Z_\mu + h.c. \\ &= -\frac{g}{\sqrt{2}} \sum_{\alpha=e,\mu,\tau} \overline{\nu}'_{\alpha L}\gamma^\mu \ell'_{\alpha L} W_\mu - \frac{g}{2\cos\theta_W} \sum_{\alpha=e,\mu,\tau} \overline{\nu}'_{\alpha L}\gamma^\mu \nu'_{\alpha L} Z_\mu + h.c.\end{aligned} \tag{1.4}$$

where g is the $SU(2)_L$ coupling, θ_W is the Weinberg angle [10], $j^{\mu}_{W,L}$,$j^{\mu}_{Z,\nu L}$ the leptonic weak charged current and neutrino neutral current, respectively. The three neutrino fields ν_e, ν_μ, ν_τ (obtained upon diagonalization of Y'^{ℓ} in 1.2) are called flavour neutrino fields, and in the SM they are also mass eigenstates. Each of them couples only with the corresponding charged lepton field in the charged weak current term in (1.4).

With the discovery of neutrino oscillations in 1998 through the Super-Kamiokande atmospheric neutrino experiment [20], it became evident that an extension of the Standard Model is necessary to account for neutrino mass eigenstates. Formally a Dirac neutrino mass can also be generated by the standard Higgs mechanism [21] that gives masses to quarks and charged leptons in the SM. In the sometimes called *minimally extended Standard Model*,

the SM asymmetry between lepton and quark sectors due to the absence of right-handed neutrino fields $\nu_{\alpha R}$ (with $\alpha = e, \mu, \tau$) is eliminated [18]. These fields are singlets under the $SU(2)_L \times U(1)_Y$ gauge transformations (with hypercharge $Y = 0$), and do not take part in the SM weak interaction. Thus they are called *sterile* and their only interaction is gravitational. On the other hand, the standard left-handed neutrino fields, which are involved in weak interactions, are typically referred to as *active neutrinos*. In the minimally extended SM with three right-handed neutrino fields (the number of right-handed neutrino fields is actually not constrained by the theory), the SM Higgs-lepton Yukawa Lagrangian in (1.2) is extended:

$$\mathcal{L}_{H,L} = - \sum_{\alpha,\beta=e,\mu,\tau} Y'^{\ell}_{\alpha\beta} \overline{L'_{\alpha L}} \phi \ell'_{\beta R} - \sum_{\alpha,\beta=e,\mu,\tau} Y'^{\nu}_{\alpha\beta} \overline{L'_{\alpha L}} \tilde{\phi} \nu'_{\beta R} + h.c., \tag{1.5}$$

where Y'^{ν} is a new matrix of Yukawa couplings and $\tilde{\phi} = i\tau_2 \phi^*$ is the conjugated Higgs doublet. In the unitary gauge, after diagonalizing Y'^{ν}, this takes the form

$$\mathcal{L}_{H,L} = - \left(\frac{v + H}{\sqrt{2}} \right) \left[\sum_{\alpha=e,\mu,\tau} y^{\ell}_{\alpha} \overline{\ell_{\alpha L}} \ell_{\alpha R} + \sum_{k=1}^{3} y^{\ell}_{k} \overline{\nu_{kL}} \nu_{kR} \right] + \text{h.c.} \tag{1.6}$$

By expanding its terms and using the Dirac neutrino fields $\nu_k = \nu_{kL} + \nu_{kR}$ we obtain the Higgs-neutrino coupling terms and the neutrino mass is $m_k = y^{\nu}_k v/\sqrt{2}$ $(k = 1, 2, 3)$. While Dirac neutrino masses can be incorporated into the Standard Model, this scenario appears highly unlikely. The main concern is associated with the smallness of neutrino masses and neutrino Yukawa couplings. Before going to the next section, it is crucial to bear in mind that for massive neutrinos the flavour fields do not have a definite mass and are not independent.

1.3 Neutrinos Beyond the Standard Model

Neutral fermions could be either of Dirac or Majorana type, as theorized by Ettore Majorana in 1937 [22]. In particular, among known elementary fermions only neutrinos are neutral and thus can be Majorana particles. Starting from a Dirac mass term for a Dirac neutrino field $\nu = \nu_L + \nu_R$

$$\mathcal{L}^{\text{D}}_{\text{mass}} = -m\bar{\nu}\nu = -m\left(\overline{\nu_R}\nu_L + \overline{\nu_L}\nu_R\right) = -m\overline{\nu_R}\nu_L + \text{ h.c. }, \tag{1.7}$$

the RH neutrino field can be substituted by $\nu^C_L = C\overline{\nu_L}^T$, that is a right-handed function of ν_L which transforms as ν_L under Lorentz transformations.

This leads to the Majorana mass term

$$\mathcal{L}^{\mathrm{M}}_{\mathrm{mass}} = -\frac{1}{2} m \overline{\nu_L^C} \nu_L + \text{ h.c. } . \tag{1.8}$$

If one defines the Majorana field as $\nu = \nu_L + \nu_L^C$, which satisfies the Majorana condition $\nu^C = \nu$, equation (1.8) can be rewritten as $\mathcal{L}^{\mathrm{M}}_{\mathrm{mass}} = -\frac{1}{2} m \overline{\nu} \nu$. It is crucial to notice that, even if the Majorana mass term (1.8) involves only the neutrino left-handed field ν_L, which is present in the SM, such a possibility is forbidden by the $SU(2)_L \times U(1)_Y$ symmetries. Thus, it is not possible in the SM to have a renormalizable Lagrangian term which can generate a Majorana neutrino mass. From this perspective, neutrino masses and mixing represent the first evidence that the SM is incomplete. In presence of both ν_L and ν_R fields, in the one-generation most general case, is possible to have a Dirac-Majorana mass term

$$\begin{aligned} \mathcal{L}^{D+M}_{\mathrm{mass}} &= \mathcal{L}^{D}_{\mathrm{mass}} + \mathcal{L}^{M,L}_{\mathrm{mass}} + \mathcal{L}^{M,R}_{\mathrm{mass}} \\ &= -\frac{1}{2} \begin{pmatrix} \overline{\nu_L} & \overline{\nu_R^C} \end{pmatrix} \begin{pmatrix} m_{M,L} & m_D \\ m_D & m_{M,R} \end{pmatrix} \begin{pmatrix} \nu_L \\ \nu_R^C \end{pmatrix} + \text{ h.c. } . \end{aligned} \tag{1.9}$$

By diagonalizing the mass matrix, we obtain two Majorana neutrino fields , with masses

$$m_{2,1} = \frac{1}{2} \left[m_L + m_R \pm \sqrt{(m_L - m_R)^2 + 4 m_{\mathrm{D}}^2} \right] . \tag{1.10}$$

In the simplest scenarios, where the Dirac mass term is much smaller than the right-handed Majorana mass term $m_D \ll m_R$ and the left-handed Majorana mass term (m_L) is zero, the *see-saw type-I mechanism* [23–25] predicts a very light neutrino mass (m_1) and a much heavier mass (m_2) for the second neutrino:

$$\begin{aligned} m_1 &\simeq \frac{m_{\mathrm{D}}^2}{m_R} \\ m_2 &\simeq m_R \end{aligned} \tag{1.11}$$

The name see-saw is derived indeed to illustrate the inverse relationship between the heavy mass $m_2 \simeq m_R$ of ν_2, that is responsible for the lightness of ν_1. Moreover, this model suggests that the lighter neutrino ν_1 is mostly the active left-handed neutrino ν_L, and the heavier neutrino ν_2 is predominantly the sterile right-handed neutrino ν_R. The seesaw formula can provide a natural explanation for the observed tiny neutrino masses. In the presented framework, right-handed neutrinos are sterile and largely irrelevant to low-energy physics due to their very small coupling and the strongly suppressed

mixing with light neutrinos. However, not all right-handed neutrino fields need to be heavy and some might be light, belonging to low-energy BSM physics [19]. In the next sections, we will consider sterile neutrinos at the eV scale, which are relevant for neutrino oscillations measurable in Short Baseline experiments.

1.4 Neutrino Oscillations

The phenomenon of neutrino oscillation is a quantum mechanical process first proposed in the late 1950s by Bruno Pontecorvo [26, 27]. Due to the presence of leptonic mixing and non-degenerate neutrino masses, neutrino oscillations are the result of interference between various massive neutrino states, which are produced and detected coherently due to their extremely small mass differences. At the time of Pontecorvo's proposal, only the electron neutrino was known, which led him to conceptualize the idea of a sterile neutrino [28]. The muon neutrino was discovered in 1962 by Lederman, Schwartz, Steinberger, *et al.* [29] validating Pontecorvo's earlier predictions and opening up the possibility of oscillations among different active neutrino flavours.

The concept of neutrino mixing and the notion that neutrinos must be massive and mixed for oscillations to occur were developed further in 1962 by Maki, Nakagawa, and Sakata [30]. Pontecorvo's prediction of the Solar Neutrino Problem [28], with the hypothesis of $\nu_e \rightarrow \nu_\mu$ (or $\nu_e \rightarrow \nu_{\text{sterile}}$) transitions, was in agreement with the first measurements of the solar electron neutrino flux [31]. It was indeed found by the Sudbury Neutrino Observatory (SNO) experiment [32] that only about one-third of the number of neutrinos predicted by the Standard Solar Model (SSM) were reaching the detector on Earth.

The underlying principle is that neutrinos, produced and detected as flavour states, are coherent superpositions of massive states with slightly varying masses. As these massive components travel, their phases diverge slightly, altering the state over distance. At the point of detection, this can result in the observation of a different neutrino flavour compared to the initial one. This oscillatory behavior, sustained by coherence during propagation, is made possible due to the neutrinos weakly interacting nature, allowing them to traverse vast distances without significant interference.

The oscillations are due to the mixing between the flavour eigenstates (ν_e, ν_μ, ν_τ) and the mass eigenstates (ν_1, ν_2, ν_3). Therefore, the flavour eigenstates ν_α ($\alpha = e, \mu, \tau$) can be descibed as a linear combination of mass

eigenstates ν_k (k = 1, 2, 3):

$$|\nu_\alpha\rangle = \sum_k U^*_{\alpha k} |\nu_k\rangle \quad (\alpha = e, \mu, \tau). \tag{1.12}$$

Here the proportion of each ν_k is determined by the weights proportional to $U^*_{\alpha k}$, where U is the so-called Pontecorvo-Maki-Nakagawa-Sakata (PMNS) unitary matrix. This matrix, that relates the mass and the flavour basis, is often parametrized as [33, 34]:

$$U_{\alpha k} = \begin{pmatrix} c_{12}c_{13} & s_{12}c_{13} & s_{13}e^{-i\delta} \\ -s_{12}c_{23} - c_{12}s_{23}s_{13}e^{i\delta} & c_{12}c_{23} - s_{12}s_{23}s_{13}e^{i\delta} & s_{23}c_{13} \\ s_{12}s_{23} - c_{12}c_{23}s_{13}e^{i\delta} & -c_{12}s_{23} - s_{12}c_{23}s_{13}e^{i\delta} & c_{23}c_{13} \end{pmatrix} \cdot \mathcal{P}, \tag{1.13}$$

where we define $c_{kj} \equiv \cos\theta_{kj}$ and $s_{kj} \equiv \sin\theta_{kj}$, with $\theta_{kj} \in [0, 90°]$. In this notation, δ is the Dirac CPV phase $\delta \in [0, 360°]$ and $\mathcal{P}$ is a diagonal phase matrix $\mathcal{P} \equiv \text{diag}\left(1, e^{i\frac{\lambda_{21}}{2}}, e^{i\frac{\lambda_{31}}{2}}\right)$ which embeds the two Majorana CPV phases $\lambda_{21}, \lambda_{31}$. The massive neutrino states $|\nu_k\rangle$ are eigenstates of the Hamiltonian, with energy eigenvalues $E_k = \sqrt{\vec{p}^2 + m_k^2}$. From Schrödinger equation, these states evolve in time as plane waves:

$$|\nu_k(t)\rangle = e^{-iE_k t} |\nu_k\rangle . \tag{1.14}$$

From equations (1.12) and (1.14), the neutrino produced at $t = 0$ with flavour state ν_α, evolves in time as:

$$|\nu_\alpha(t)\rangle = \sum_k U^*_{\alpha k} e^{-iE_k t} |\nu_k\rangle . \tag{1.15}$$

The unitarity of the PMNS matrix allows for the representation of massive states as a combination of flavour states, formulated as $|\nu_k\rangle = \sum_\alpha U_{\alpha k} |\nu_\alpha\rangle$. This leads to the observation that, for times $t > 0$, the superposition of massive neutrino states $|\nu_\alpha(t)\rangle$ becomes a superposition comprising various flavour states (if there is leptonic mixing i.e. U is not diagonal)

$$|\nu_\alpha(t)\rangle = \sum_{\beta=e,\mu,\tau} \left(\sum_k U^*_{\alpha k} e^{-iE_k t} U_{\beta k} \right) |\nu_\beta\rangle . \tag{1.16}$$

The probability of transitions $\nu_\alpha \to \nu_\beta$ with time t is, then, given by

$$P_{\nu_\alpha \to \nu_\beta}(t) = |\langle \nu_\beta \mid \nu_\alpha(t) \rangle|^2 = \sum_{k,j} U^*_{\alpha k} U_{\beta k} U_{\alpha j} U^*_{\beta j} e^{-i(E_k - E_j)t}. \tag{1.17}$$

In oscillation experiments neutrinos are ultrarelativistic, and one can approximate for $E \sim |\vec{p}|$

$$E_k - E_j \simeq \frac{\Delta m^2_{kj}}{2E} \tag{1.18}$$

with $\Delta m^2_{kj} \equiv m^2_k - m^2_j$ squared-mass difference. Moreover, since ultrarelativistic neutrinos propagate almost at the speed of light, one can take $t = L$, and the transition probability is

$$P_{\nu_\alpha \to \nu_\beta}(L, E) = \sum_{k,j} U^*_{\alpha k} U_{\beta k} U_{\alpha j} U^*_{\beta j} \exp\left(-i \frac{\Delta m^2_{kj} L}{2E}\right). \tag{1.19}$$

The oscillation probabilities with $\alpha \neq \beta$ are usually called *transition probabilities*, whereas the oscillation probabilities with $\alpha = \beta$ are usually called *survival probabilities*. In practice, neutrino oscillation experiments are classified by the type of measurement performed, in:

- *Appearance experiments* ($P(\nu_\alpha \to \nu_\beta)$, with $\alpha \neq \beta$), focus on detecting transitions between various neutrino flavours. These experiments are particularly effective when the neutrino flavour being detected is not initially present in the beam, leading to a significantly reduced background. This reduction enables these experiments to be sensitive to relatively small mixing angles.

- *Disappearance experiments* $\left(P(\nu_\alpha \to \nu_\alpha) = 1 - \sum_{\beta \neq \alpha} P(\nu_\alpha \to \nu_\beta)\right)$, aim to measure the survival probability of a specific neutrino flavour. This is done by counting the number of neutrino interactions in the detector and comparing this count to the expected number. However, due to statistical fluctuations in the detection process, even when no oscillations occur, it becomes challenging to detect a slight disappearance of neutrinos. As a result, disappearance experiments are generally less effective in measuring small mixing angles accurately.

From equation 1.19, it follows that oscillation experiments do not inform us on the absolute value of neutrino masses, but only on their squared-mass differences. The standard framework of neutrino oscillations, involving three active neutrinos, reveals two independent squared-mass differences - the solar and atmospheric Δm^2 - with values

$$\Delta m^2_{\text{SOL}} = \Delta m^2_{21} \simeq 7.4 \times 10^{-5} \text{eV}^2,$$
$$\Delta m^2_{\text{ATM}} = \left|\Delta m^2_{31}\right| \simeq \left|\Delta m^2_{32}\right| \simeq 2.5 \times 10^{-3} \text{eV}^2.$$

There are two possible scenarios for the ordering of neutrino masses consistent with the experimental measurements:

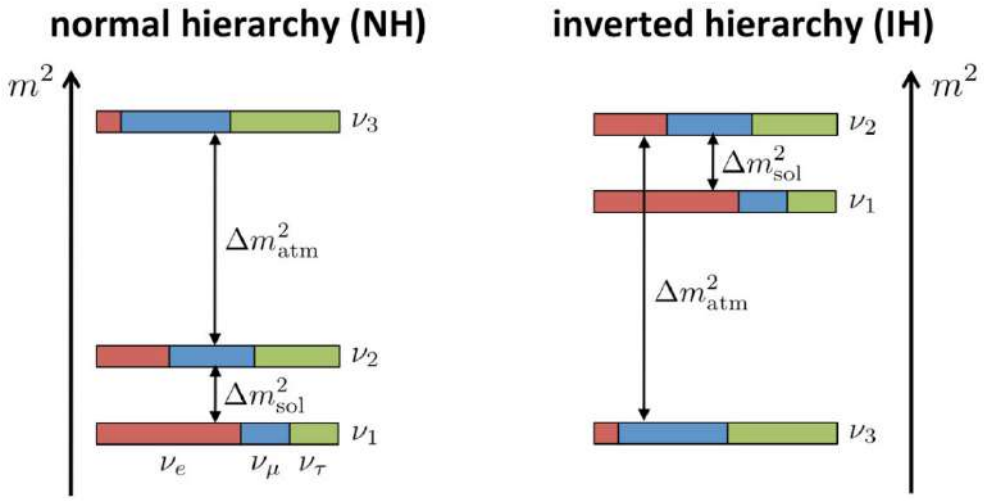

Figure 1.3: A visual representation of the two possible neutrino mass hierarchies. For each mass eigenstate the relative proportion of ν_e (red), ν_μ (blue) and ν_τ (green) are shown. Credits: JUNO collaboration.

- Normal Hierarchy (NH), with $m_1 < m_2 \ll m_3$; Hierarchy (IH), with $m_3 \ll m_2 < m_1$.

The two scenarios ca also be referred to as normal ordering (NO) or inverted ordering (IO). The two possible hierarchies for neutrino masses are shown in Figure 1.3.

1.4.1 Two-neutrino oscillations

If we neglect the coupling of the flavour neutrinos with the third massive neutrino, we obtain an effective model with two-neutrino mixing [18]. This simplified model is adopted in many experiments that are not sensitive to the influence of three-neutrino mixing. Considering two neutrino flavours ν_α and ν_β, , they can either be distinct flavour neutrinos (such as $\alpha, \beta = e, \mu$; $\alpha, \beta = e, \tau$; or $\alpha, \beta = \mu, \tau$), or they can be linear combinations of these pure flavour neutrinos. An example of such a combination is where $\nu_\alpha = \nu_e$ and ν_β is a mix of ν_μ and ν_τ, denoted as $c_\mu \nu_\mu + c_\tau \nu_\tau$, with the condition that $c_\mu^2 + c_\tau^2 = 1$. This scenario is particularly relevant in experiments involving the disappearance of electron neutrinos or in $\nu_e \to \nu_{\mu,\tau}$ experiments where ν_μ and ν_τ are not distinguished. The massive basis ν_1, ν_2 is related to the

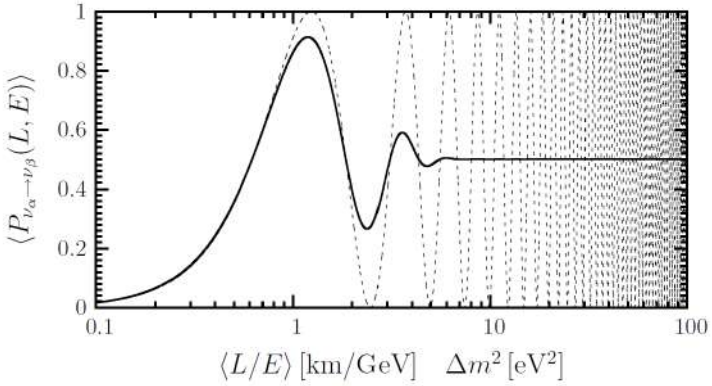

Figure 1.4: Transition probability of $\nu_\alpha \to \nu_\beta$ for $\sin^2 2\vartheta = 1$ as a function of $\langle L/E \rangle [km/GeV] \Delta m^2 [eV^2]$. Solid line: transition probability averaged over a Gaussian L/E distribution with $\sigma_{L/E} = 0.2\langle L/E \rangle$. Dashed line: unaveraged transition probability with $\langle L/E \rangle = L/E$ [18].

flavour basis ν_α, ν_β by the elements of the two-neutrino effective matrix

$$\begin{pmatrix} \nu_\alpha \\ \nu_\beta \end{pmatrix} = \begin{pmatrix} \cos\theta & \sin\theta \\ -\sin\theta & \cos\theta \end{pmatrix} \begin{pmatrix} \nu_1 \\ \nu_2 \end{pmatrix} \tag{1.20}$$

where θ is the mixing angle. From (1.19) we can express the probability for transitions $\nu_\alpha \to \nu_\beta$ with $\alpha \neq \beta$ as

$$P_{\nu_\alpha \to \nu_\beta}(L,E) = \sin^2 2\vartheta \sin^2 \left(\frac{\Delta m^2 L}{4E} \right) \quad (\alpha \neq \beta), \tag{1.21}$$

and thus the survival probability obtained by unitarity is $P_{\nu_\alpha \to \nu_\alpha}(L,E) = 1 - P_{\nu_\alpha \to \nu_\beta}(L,E)$. Here we have only one mass-squared difference $\Delta m^2 \equiv \Delta m^2_{21} \equiv m^2_2 - m^2_1$. For a given baseline, determined by the distance from the source to the detector, the energy at the peak of the first oscillation is governed by Δm^2. Expressing the argument in equation (1.21) in the relevant units of the experimental setting:

$$\frac{\Delta m^2 L}{4E} = 1.27 \frac{\Delta m^2 \left[\text{eV}^2\right] L[\text{m}]}{E[\text{MeV}]} = 1.27 \frac{\Delta m^2 \left[\text{eV}^2\right] L[\text{km}]}{E[\text{GeV}]} \tag{1.22}$$

The transition probability's behavior in equation (1.21) for $\sin^2 2\vartheta = 1$ as a function of L/E [km/GeV] Δm^2 $[eV^2]$ is depicted by the dashed line in Figure 1.4. Holding the squared-mass difference Δm^2 and energy E constant, the axis represents the distance L. The transition probability has its first

minimum at the oscillation length $L^{\text{osc}} = 2.47 \left(E\,[\text{GeV}]\ \ \Delta m^2\ \left[\text{eV}^2\right]\right)$ km and reaches a maximum when $\Delta m^2 L/4E = \pi/2$. The transition probability is minimal for $L \ll L^{\text{osc}}$ and oscillates rapidly for $L \gg L^{\text{osc}}$ on a logarithmic scale of L. Given that Δm^2 is a constant determined by nature, various experiments can be designed to detect different values of Δm^2 by selecting the values for the ratio L/E. The ability of an experiment to detect a specific value of Δm^2, known as its sensitivity to Δm^2, is defined for the value of Δm^2 at which:

$$\frac{\Delta m^2 L}{2E} \sim 1 \tag{1.23}$$

Different neutrino oscillation experiments are traditionally classified by their average value of the L/E, which dictates their sensitivity to Δm^2. They can be grouped into *Short Baseline* (SBL), *Long Baseline* (LBL), and *Very Long-Baseline* (VBL) categories, depending on the distance L. Additionally, these experiments can be divided based on the type of neutrino source they employ, which may be either artificial sources like reactors or accelerators, or natural sources such as solar or atmospheric neutrinos.

1.5 Experimental neutrino anomalies

Numerous neutrino experiments at short baselines observed several "anomalies" in their data, that challenge the conventional three-neutrino framework. These include the *Reactor Neutrino Anomaly*, the *Gallium Anomaly*, the *LSND Anomaly*, the *MiniBooNE Low-Energy Excess*, and the more recently identified *Neutrino-4 Anomaly*. A common interpretation of these anomalies suggests the need for an oscillation frequency of $\Delta m^2 \gtrsim 1\text{eV}^2$, pointing towards the addition of at least one sterile neutrino into the existing three-flavour mixing model. Despite this, the purely oscillatory explanation is disfavored due to various direct and indirect experimental results. Consequently, in recent years, alternative theoretical interpretations BSM have emerged along with an extensive and dedicated scientific program to definitely solve the puzzle of SBL anomalies.

1.5.1 The Reactor Antineutrino Anomaly

The Reactor Antineutrino Anomaly (RAA), identified in 2011 [35], emerged following new calculations by Mueller et al. [36] of the fluxes of reactor-produced $\overline{\nu_e}$, where the antineutrinos result from the decay chains of fissionable isotopes like ^{235}U, ^{238}U, ^{239}Pu, and ^{241}Pu. These updated calculations

predicted antineutrino fluxes about 5% higher than previous estimates. Consequently, the expected detection rates in several Short Baseline reactor neutrino experiments, with detectors placed 10 to 100 meters from the reactors, were found to be higher than the observed rates. These experiments are designed to detect $\overline{\nu_e}$ through the inverse β decay (IBD) process $\overline{\nu_e}+p \rightarrow n+e^+$. In particular the average ratio $\bar{R}$ of the measured (N_{exp}) and calculated N_{cal} number of ν_e events is $\bar{R} = 0.928 \pm 0.024$, which indicates a deficit with a statistical significance of 3.0σ [19]. The ratios of measured to the predicted IBD yields for different experiments are shown in Figure 1.5 (b). The possibility that this deficit could be attributed to oscillations involving sterile neutrinos, which would oscillate undetected at a frequency of approximately 1 eV^2, was considered a plausible explanation.

1.5.2 The Gallium Neutrino Anomaly

The Gallium Neutrino Anomaly consists in the disappearance of electron neutrinos ν_e measured in radioactive source experiments perfomed by the GALLEX [37] and SAGE [38] collaborations. In these experiments, intense artificial radioactive sources of ^{51}Cr and ^{37}Ar were used, producing ν_e through electron capture processes. The produced ν_e were then detected using the reaction $\nu_e + {}^{71}\text{Ga} \rightarrow {}^{71}Ge + e^-$, a process initially intended to identify solar neutrinos converting gallium into germanium isotopes. In these radiochemical experiments the produced ^{71}Ge isotopes are extracted through chemical processes. The total number of neutrino interactions with the detector is determined by the amount of ^{71}Ge extracted. The ratio R of the number of electron neutrino events measured in the GALLEX and SAGE experiments and that calculated with the Gamow-Teller coefficients has an average of $\bar{R} = 0.84 \pm 0.05$, as shown in Figure 1.5 (a), indicating a deficit with a statistical significance of 2.9 σ [19]. The average neutrino traveling distances in the GALLEX and SAGE experiments were $\langle L \rangle_{\text{GALLEX}} = 1.9$ m and $\langle L \rangle_{\text{SAGE}} = 0.6$ m respectively, and the neutrino energy was approximately 0.8 MeV. This anomaly is compatible with neutrino oscillations generated by $\Delta m^2_{SBL} \gtrsim 1\text{eV}^2$.

1.5.3 LSND and MiniBooNE

The LSND (Liquid Scintillator Neutrino Detector) experiment [39] was conducted at the Los Alamos Neutron Science Center from 1993 to 1998. In this experiment, an intense proton beam of approximately 1 mA and 798 MeV energy was directed at a target, producing a large number of pions. Due to the absorption of most π^- by the target nuclei, the neutrinos were primarily

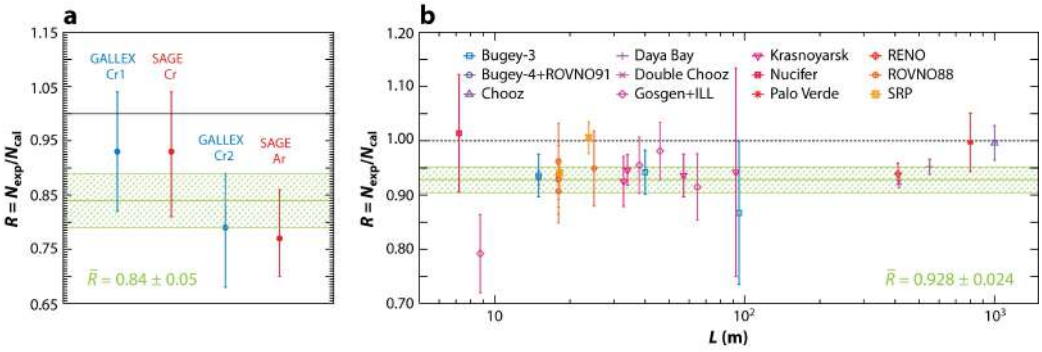

Figure 1.5: Plots showing the (a) gallium neutrino and (b) reactor antineutrino anomalies. The error bars on the data points indicate the uncorrelated experimental uncertainties. The solid green horizontal line and the shaded band represent the average ratio R and its associated uncertainties.

generated by the decays $\pi^+ \to \mu^+ + \nu_\mu$ and $\mu^+ \to e^+ + \nu_e + \overline{\nu_\mu}$, predominantly as decays at rest (DaR). Since no $\overline{\nu_e}$ is produced in these decays, the LSND detector, positioned 30 meters from the target and consisting of a tank filled with 167 tons of mineral oil doped with liquid scintillators, was designed to search for possible $\overline{\nu_\mu} \to \overline{\nu_e}$ oscillations by detecting $\overline{\nu_e}$ events through IBD, in the range $20 \lesssim E_e \lesssim 60$ MeV for the energy of the detected positron. The scintillation light readout was conducted using 1220 photomultiplier tubes uniformly distributed on the tank's inner surface. The LSND data showed an excess (see Figure 1.6) of $\overline{\nu_e}$-like events over the background at the level of approximately 3.8σ. These oscillations suggested the possibility of a $\Delta m^2_{SBL} \gtrsim 0.1\,\mathrm{eV}^2$.

Following the LSND findings, the MiniBooNE (Mini Booster Neutrino Experiment) at Fermilab [40, 41], which began operations in 2002, was designed to check the LSND anomaly. Unlike LSND, which relied on neutrinos produced from π^+ decaying at rest, MiniBooNE used an 8 GeV proton beam from Fermilab's booster to produce a beam of pions, focusing on π^+ decay-in-flight (DiF). This approach generated a ν_μ-dominated flux with a higher mean energy (~ 600 MeV), allowing for an independent test at a longer baseline. The MiniBooNE detector, located 541 meters from the target and filled with 818 tons of pure mineral oil (CH_2), was equipped with 1520 photomultiplier tubes to detect the Cherenkov light and isotropic scintillation produced by charged particles (see Figure 1.7) [40]. The event reconstruction method used Cherenkov rings detected on the inner surface of the detector to differentiate electrons, muons, and pions. The main limitations of MiniBooNE were that the interaction topologies were not directly reconstructed, and single

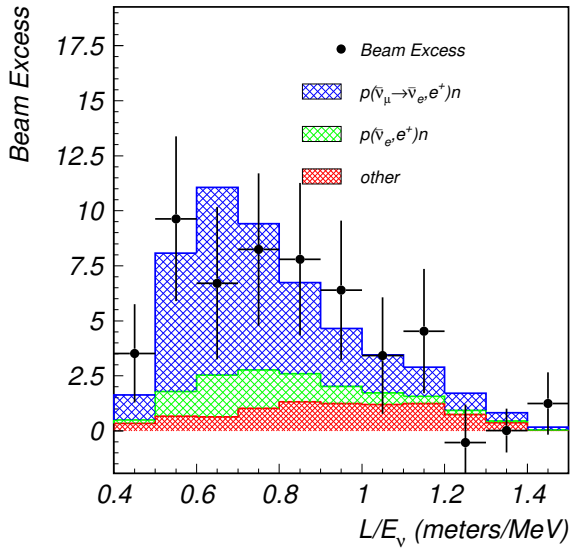

Figure 1.6: The LSND anomaly excess as a function of L/E_ν, for events with detected positron energy in the range $20 \lesssim E_e \lesssim 60$ MeV.

photons were indistinguishable from single electrons. Initially, MiniBooNE operated in "neutrino mode", focusing on a beam of π^+ that decayed in a tunnel, producing an almost pure beam of ν_μ. In its first phase, MiniBooNE considered data with $E \gtrsim 475$ MeV, citing that this threshold reduced several backgrounds while maintaining sensitivity to oscillations. However, no significant excess over the background was observed in this energy range, leading to a 98% exclusion of neutrino oscillation as the explanation for the LSND anomaly. Yet, an excess of ν_e-like events in both neutrino and antineutrino mode, referred to as the MiniBooNE "Low-Energy Excess" (LEE), was observed below the 475 MeV analysis threshold with a statistical significance of 4.8 σ. The final MiniBooNE allowed regions for events with $200 < E_\nu^{QE} < 3000$ MeV within a two-neutrino oscillation model is shown in Figure 1.8 [42]. This low-energy excess corresponds to L/E values mostly outside the LSND range and could potentially be attributed to single-photon events produced by neutral-current ν_μ-induced π^0 decays, where only one of the two decay photons is visible, a possibility that the Micro Booster Neutrino Experiment (MicroBooNE) experiment at Fermilab would later investigate. Additional interpretations of the excess, consider factors such as energy misreconstruction, incomplete estimation of backgrounds, and potentially other Beyond the Standard Model physics.

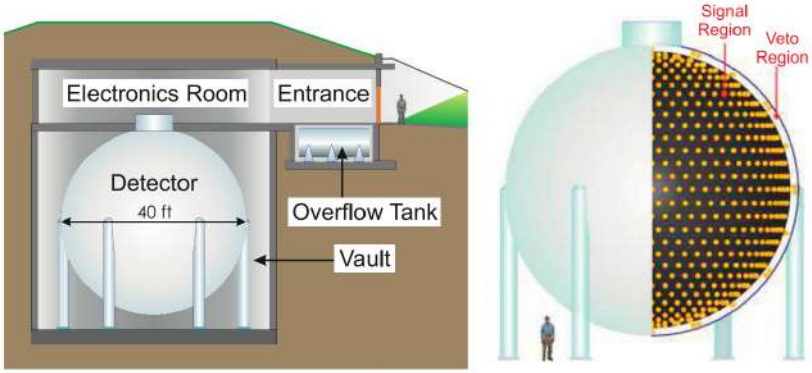

Figure 1.7: Schematic representation of the MiniBooNE detector, with a cut-away drawing showing the PMT's distribution in the signal and veto regions.

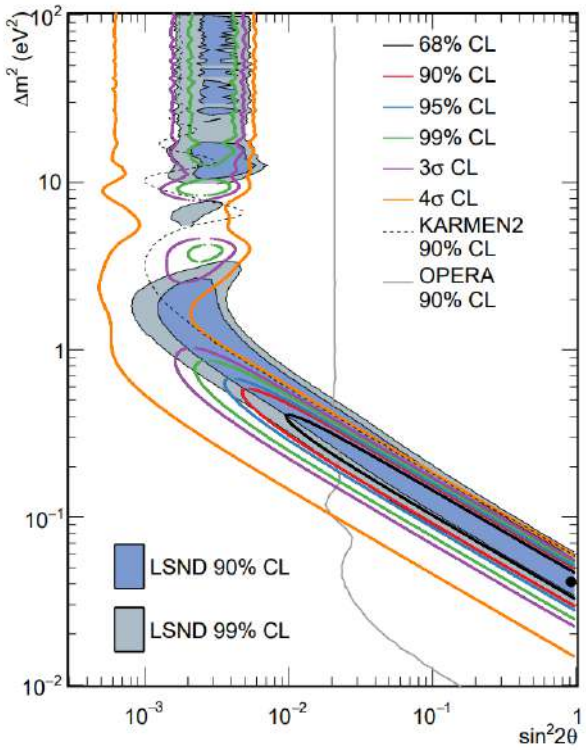

Figure 1.8: MiniBooNE allowed regions for a combined neutrino and antineutrino mode data sets, within a two-neutrino oscillation model. The shaded areas show the 90% and 99% C.L. LSND $\bar{\nu_\mu} \to \bar{\nu_e}$ allowed regions. The black point shows the MiniBooNE best fit point.

1.5.4 Neutrino 4

Neutrino-4 [43, 44] is a gadolinium-based liquid-scintillator experiment, situated near the powerful and compact 100 MW SM-3 research reactor in Dimitrovgrad, Russia. The experiment uses a 1.8 m^3 detector divided into 50 liquid-scintillator sections, arranged in 10 rows with 5 sections each. Mounted on a movable platform, the detector's baseline varies between 6 and 12 meters, allowing frequent changes in the detector's position relative to the reactor core to partially cancel systematic uncertainties. Due to its proximity to the surface, Neutrino-4 faces significant cosmogenic-induced backgrounds, resulting in a relatively low signal-to-background ratio of only 0.54. From 2016 to 2021, the experiment collected data at a rate of $\sim$ 300 events/day, corresponding to 720 (reactor on) and 860 (reactor off) days of data. The main result indicates an L/E dependence of IBD rate normalized to the rate averaged over all distances, fitting well with an oscillation signal characterized by $\sin^2 2\vartheta_{ee} = 0.35$ and $\Delta m^2_{41} = 7.22\text{eV}^2$, with a reported 3σ significance for the best-fit point. However, these results conflict with the limits obtained by other reactor measurements, such as PROSPECT and STEREO, and with the solar neutrino upper bound for $\sin^2 2\vartheta_{ee}$. Therefore, it is difficult to consider the Neutrino-4 data to be a reliable indication in favor of SBL neutrino oscillations [19].

1.5.5 eV-Scale Sterile Neutrinos

The SBL neutrino oscillation anomalies here discussed, can be explained with the assumptions that there is at least one additional squared-mass difference, notably larger than the solar and atmospheric ones:

$$\Delta m^2_{\text{SBL}} \sim 1\text{eV}^2$$

To accommodate this, the neutrino mixing framework must be extended to include at least one light massive neutrino beyond the three in the standard scheme. Taking into account the scenario with only light sterile neutrinos, the minimal scheme which can explain the anomalies in the neutrino sector found in some short-baseline experiments is the so called "3+1" model, where the mixing matrix is modified to include this additional neutrino:

$$\begin{pmatrix} \nu_e \\ \nu_\mu \\ \nu_\tau \\ \nu_s \end{pmatrix} = \begin{pmatrix} U_{e1} & U_{e2} & U_{e3} & U_{e4} \\ U_{\mu 1} & U_{\mu 2} & U_{\mu 3} & U_{\mu 4} \\ U_{\tau 1} & U_{\tau 2} & U_{\tau 3} & U_{\tau 4} \\ U_{s1} & U_{s2} & U_{s3} & U_{s4} \end{pmatrix} \begin{pmatrix} \nu_1 \\ \nu_2 \\ \nu_3 \\ \nu_4 \end{pmatrix} \tag{1.24}$$

This new scheme is compatible with existing solar, atmospheric, and long-baseline experimental data, as it perturbs only slightly the standard 3 neutrino mixing and the massive v_4 is predominantly sterile if

$$|U_{\alpha 4}|^2 \ll 1 \quad (\alpha = e, \mu, \tau). \tag{1.25}$$

In SBL experiments, it is possible to neglect the smaller $\Delta m^2_{\rm SOL}$ and $\Delta m^2_{\rm ATM}$, leading to effective SBL oscillation probabilities. Hence assuming $\Delta m^2_{41} \gg |\Delta m^2_{31}|, \Delta m^2_{21}$, these probabilities can be well described by a two-flavour vacuum oscillation formula

$$P_{\alpha\beta} = \delta_{\alpha\beta} - 4|U_{\alpha 4}|^2(\delta_{\alpha\beta} - |U_{\alpha 4}|^2)\sin^2\left(\frac{\Delta m^2_{41} L}{4E}\right), \tag{1.26}$$

where L is the baseline and E is the neutrino energy [45]. These probabilities are particularly relevant for distances where $L/E_\nu \approx 1$ m/MeV or 1 km/GeV, given $\Delta m^2_{41} \approx 1\text{eV}^2$. In these experiments the appearance and disappearance of ν_e and ν_μ depend on $|U_{e4}|^2$ and $|U_{\mu 4}|^2$ as

$$\nu_\mu \to \nu_e : \sin^2 2\theta_{\mu e} = 4|U_{\mu 4}|^2|U_{e4}|^2 \qquad \text{(LSND, MiniBooNE anomalies);} \tag{1.27}$$

$$\nu_e \to \nu_e : \sin^2 2\theta_{ee} = 4|U_{e4}|^2(1 - |U_{e4}|^2) \qquad \text{(Reactor, Gallium anomalies);} \tag{1.28}$$

$$\nu_\mu \to \nu_\mu : \sin^2 2\theta_{\mu\mu} = 4|U_{\mu 4}|^2(1 - |U_{\mu 4}|^2) \qquad \text{(no anomaly observed).} \tag{1.29}$$

A key observation is that the amplitudes of these oscillations, are determined exclusively by three elements in the last column of the neutrino mixing matrix. This dependency establishes a direct mathematical relationship between the probabilities of neutrino appearance and disappearance, that are related through $\sin^2 2\vartheta_{\alpha\beta} \simeq \frac{1}{4}\sin^2 2\vartheta_{\alpha\alpha}\sin^2 2\vartheta_{\beta\beta}$ [19], which holds true under the small mixing approximation (1.25). This relationship leads to a notable tension in current data, known as the appearance-disappearance tension.

To conclude two important aspects should be noticed in the context of sterile neutrino oscillations, crucial to test the sterile neutrino hypothesis. Firstly, the dependence of neutrino oscillations on $\sin^2(\Delta m^2_{41}/4E)$ offers a unique tool to distinguish these oscillations from other potential causes of observed anomalies. Secondly, short-baseline transitions such as $\nu_\mu \to \nu_e$, require non-zero values of U_{e4} and $U_{\mu 4}$ in the mixing matrix. This requirement results in both $\nu_\mu \to \nu_\mu$ and $\nu_e \to \nu_e$ having probabilities below 1. This scenario provides an opportunity to tightly constrain the range of possible parameters by simultaneously examining the appearance of ν_e and the disappearance of both ν_e and ν_μ in SBL experiments.

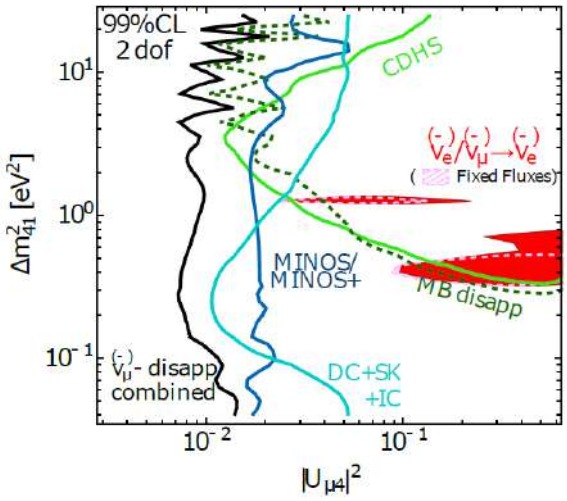

Figure 1.9: Constraints on the $3+1$ scenario from $\nu_\mu/\overline{\nu_\mu}$ disappearance. We show the allowed parameter regions, projected onto the plane spanned by the mixing matrix element $|U_{\mu 4}|^2$ and the mass squared difference Δm^2_{41}. The curve labelled DC+SK+IC combines all our atmospheric neutrino data. For comparison, we also show the parameter region favoured by ν_e disappearance and $\nu_\mu \to \nu_e$ appearance data (using LSND DaR+DiF). We show the allowed regions for the analyses with fixed and free reactor neutrino fluxes [46].

1.6 Current status and future perspectives

Several ongoing experiments aim to shed light on these anomalies, but despite these efforts a coherent picture is still missing. Notably, while anomalies have been observed in ν_e disappearance and $\nu_\mu \to \nu_e$ appearance channels, the $\nu_\mu/\overline{\nu_\mu}$ disappearance channel never observed anomalies. Strong constraints on this channel, as shown in Figure 1.9, have been provided by experiments like MINOS/MINOS+ and IceCube, limiting $|U_{\mu 4}|^2 \lesssim 10^{-2}$ across a broad Δm^2_{41} range. Atmospheric neutrino data, particularly from IceCube, offer strong constraints at $\Delta m^2_{41} \lesssim 10^{-2}$. Given these constraints and the reactor experiment limitations on $|U_{e4}|$, the values of $\sin^2 2\theta_{\mu e} \equiv 4\,|U_{e4}|^2\,|U_{\mu 4}|^2$, required by LSND and MiniBooNE, seem unattainable. This discrepancy has led to a significant tension of 4.7σ in global fits between appearance and disappearance data, as reported in Figure 1.10. It is worth to notice that these analyses integrate a wide array of experimental data, although the term "global" is somewhat indicative, as there's no consensus on the exact dataset to be included [19]. Consequently, the results of these global fits should be viewed as indicative rather than precise, pending confirmation by

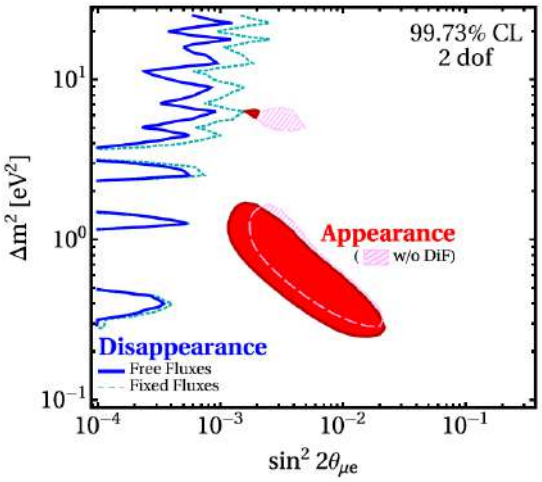

Figure 1.10: Appearance versus disappearance data in the parameter space spanned by the effective mixing angle $\sin^2 2\theta_{\mu e} \equiv 4\,|U_{e4}|^2\,|U_{\mu 4}|^2$ and the mass squared difference Δm^2_{41}. The blue curves show limits from the disappearance data sets using free reactor fluxes (solid) or fixed reactor fluxes (dashed), while the shaded contour are based on the appearance data sets using LSND DaR + DiF (red), Decay at Rest + Decay in Flight, and LSND DaR (pink) [46].

new experiments.

Chapter 2

The Short-Baseline Neutrino Program

The Short-Baseline Neutrino (SBN) program at the Fermi National Accelerator Laboratory in Illinois, is an experiment aimed at investigating the existence of sterile neutrinos at eV mass-scale. To this purpose, three Liquid Argon Time Projection Chambers (LArTPCs) are located along the 0.8 GeV muon neutrino Booster Neutrino Beamline (BNB), to measure $\nu_\mu \to \nu_e$ neutrino oscillations at at $L/E \sim 1$ km/1GeV. In addition, the physics program includes precision studies of the neutrino-argon interactions cross sections and searches for physics beyond the Standard Model.

2.1 The SBN Physics Program

The SBN experiment includes three LArTPC located on-axis along the Booster Neutrino Beam, as shown in Figure 2.1. The program emerged from a proposal [47] in 2015, to expose two LarTPC detectors to the Boost neutrino beam, in addition to the existing MicroBooNE. The Short-Baseline Near Detector (SBND), will be a 112 ton active mass LArTPC located 110 m from the neutrino production target. The SBND installation is underway, and the detector is expected to start collecting data by the end of 2024. The MicroBooNE detector, an 89 ton active mass LArTPC placed 470 m along the beam, recorded data from 2015 to 2021. The far detector, ICARUS-T600, has an active mass of 476 ton is located 600 m from the BNB proton target. ICARUS (Imaging Cosmic And Rare Underground Signals) successfully ran at Laboratori Nazionali del Gran Sasso (LNGS) from 2010 to 2013 and and has been refurbished and upgraded to optimize its performance in SBN.

The detectors locations were chosen to optimize sensitivity to neutrino

Figure 2.1: Approximate locations of the detectors superimposed on an aerial view of the Fermilab neutrino experimental area. The axis of the BNB is shown by the yellow dashed line. The pink line indicates the axis of the NuMI neutrino beam [47].

oscillations while minimizing flux systematic uncertainties. In particular, the role of the Near Detector is to characterize the neutrino beam before any oscillation, reducing the systematics uncertainties on neutrino flux and neutrino-nucleus interaction cross section. The larger far detector is installed downstream of MicroBooNE, to search for electron neutrino appearance and muon neutrino dissappearance signals. With SBND and ICARUS, the program aims to resolve the experimental anomalies in neutrino physics (see Section 1.5), performing the most sensitive search for sterile neutrinos at the eV mass-scale. This search covers the parameter regions allowed by past anomalies with 5σ sensitivity in 3 years of data taking, and will be conducted in both the $\nu_\mu \rightarrow \nu_e$ appearance and $\nu_\mu \rightarrow \nu_\mu$ disappearance channels [45]. The physics program has the following goals [48]:

- to understand the nature of MiniBooNE LEE, with MicroBooNE (Phase I);
- to search for sterile neutrinos both in appearance and disappearance channels, using SBND as near and ICARUS as far detector (Phase II);
- to further develop LArTPC technology and measure high-statistics $\nu-$

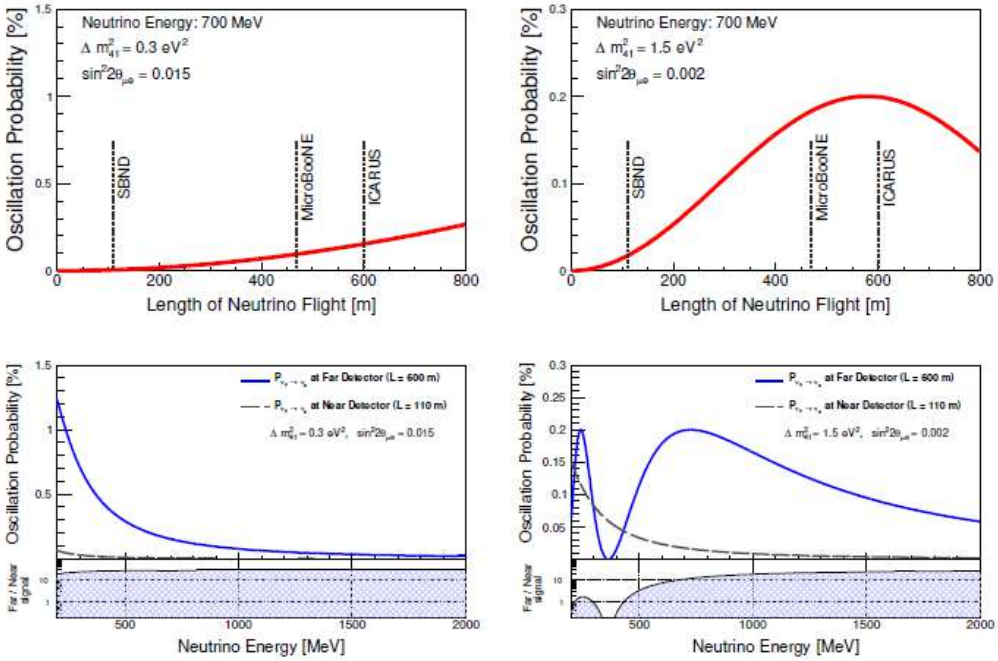

Figure 2.2: (Top) $\nu_\mu \to \nu_e$ oscillation probability, near the peak neutrino beam energy of 700 MeV, as a function of the baseline. Two different sets of parameter values are used, in a $3+1$ sterile neutrino scenario. (Bottom) $\nu_\mu \to \nu_e$ oscillation probabilities, at 110 m and 600 m, as a function of the neutrino energy for the same parameters values.

> *Ar* cross-sections in the GeV range, crucial for future long-baseline experiments like DUNE.

Beyond this, the SBN program has the potential to investigate a broad range of BSM physics: sterile neutrinos from the eV to the MeV scales, new interactions, extra dimensions, violations of Lorentz and CPT symmetries, and dark matter.

As can be seen in Figure 1.10, the global ν_e appearance data indicates a mass splitting, Δm^2_{41}, ranging from 0.3 eV^2 to 1.5 eV^2, coupled with a mixing strength within $0.002 \lesssim \sin^2(2\theta_{\mu e}) \lesssim 0.015$. Figure 2.2 illustrates the oscillation probability profile within the SBN detectors for parameter sets that span this range [45]. Far detectors measure oscillations across the entire parameter range identified by global analyses. Although a small oscillation signal may appear in the near detector at lower neutrino energies, for larger Δm^2, the very different shape and higher probability of oscillation at most

energies at the far detector maintain the experiment's strong sensitivity up to several eV^2. Highly correlated event rates in the SBN near and far detectors enable a significant reduction of uncertainties in neutrino fluxes and interaction cross sections ($10-30\%$ at BNB energies). Additionaly, SBN's use of LArTPC technology offers a crucial advantage by mitigating the main sources of backgrounds encountered in previous experiments like MiniBooNE. Specifically, the fine sampling calorimetry of LArTPC, with a spatial resolution of $\sim mm^3$, aids in distinguishing between electron-induced and photon-induced electromagnetic showers, allowing to separate ν_e signal from ν_μ NC background events in which the π_0 produced at the primary vertex decays into photons. With minimized flux and interaction uncertainties between the detectors, the focus shifts towards managing systematic differences in neutrino event selection and reconstruction.

The projected sensitivities to $\nu_\mu \to \nu_e$ appearance and ν_μ disappearance are presented,in the context of a $3+1$ sterile neutrino modelmodel, in Figure 2.3 These are derived, for SBND and ICARUS, assuming an exposure of 6.6×10^{20} protons on target (POT) delivered to the BNB target. The POT values, corresponding to approximately three years of operation for the near and far detectors, were specified in the SBN proposal [47]. The 5σ sensitivities are highlighted by the solid lines. To put it into perspective, several related results are superimposed for comparison. In the left panel, the full 99% allowed region of the LSND result is presented (shaded black), that SBN was designed to cover at $\geq 5\sigma$. Both SBND and ICARUS will exploit the BNB and Neutrinos at the Main Injector (NuMI) beams, respectively, to study the ν_e disappearance channel. SBND aims to collect over 2 million neutrino interactions annually within the full active volume (assuming 2.2×10^{20} POT), including 1.5 million ν_μ-CC events and 12,000 ν_e events per year. Similarly, ICARUS, located approximately 6° off-axis to the NuMI beam, collects a large sample of electron neutrino events in the $0-3$ GeV energy range.

2.2 The Booster Neutrino Beam

The SBN program exploits the Booster Neutrino Beam (BNB), generated by directing 8 GeV kinetic energy protons from the Booster accelerator toward a beryllium target, yielding a secondary beam primarily composed of hadrons, mainly pions [47]. These charged secondaries are directed by a single toroidal aluminum alloy focusing horn, receiving 174 kA in 143 μs pulses coinciding with proton delivery. The horn's polarity can be switched to focus either positive or negative charged mesons, while defocusing the other. The focused mesons travel down a 50 m long, 0.91 m radius air-filled

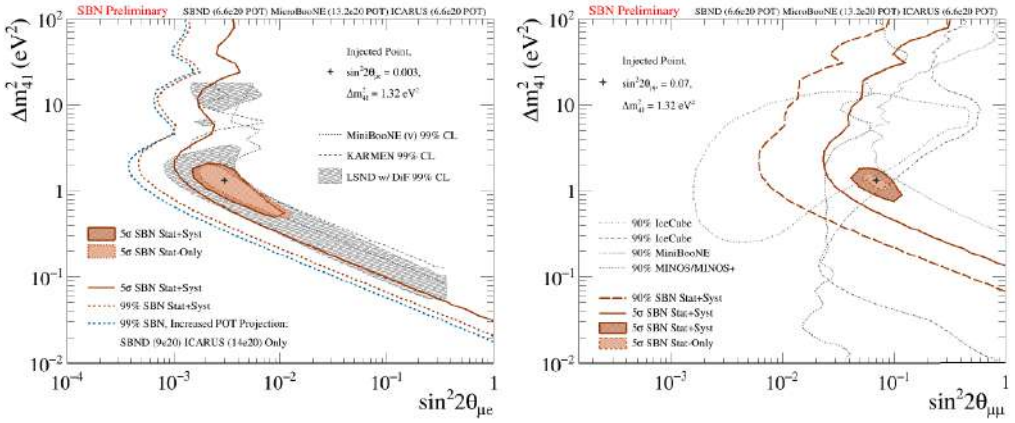

Figure 2.3: SBN 5σ sensitivity to a light sterile neutrino in the appearance (left) and disappearance (right) channels. The SBN sensitivities correspond to an integrated exposure of 6.6×10^{20} POT for BNB [].

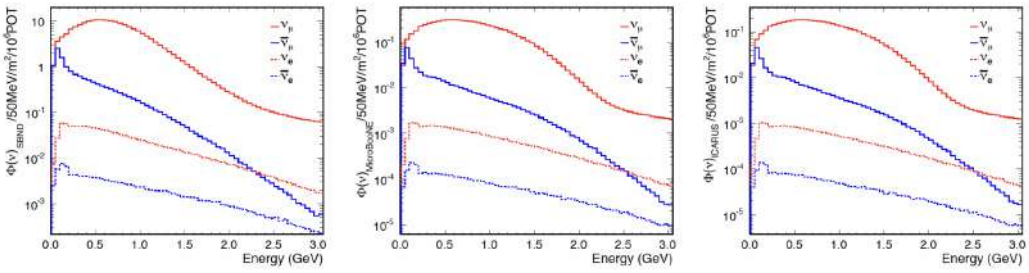

Figure 2.4: The Booster Neutrino Beam flux at the three SBN detectors: (left) SBND, (center) MicroBooNE, and (right) ICARUS-T600 [47].

tunnel, where the majority decay to produce muon and electron neutrinos, with the remainder absorbed into a concrete and steel absorber at the tunnel's end. The dominant decay channel, with a 99.9877% branching ratio, is $\pi^{+/-} \rightarrow \mu^{+/-} + \nu_\mu/\overline{\nu}_\mu$.

The Booster beam operates with a spill length of 1.6 μs, delivering nominally 5×10^{12} protons per spill to the beryllium target. The BNB's fluxes are well characterized through detailed simulations by the MiniBooNE collaboration and dedicated hadron production data from the HARP experiment at CERN. The neutrino fluxes at the three SBN detectors are shown in Figure 2.4. Is possible to notice that the rate in the near detector is 20-30 times higher than at the MicroBooNE and ICARUS locations. The composition of the flux in neutrino mode (focusing positive hadrons) varies with energy. However, it predominantly consists of ν_μ (93.6%), followed by $\overline{\nu}_\mu$ (5.9%),

with an intrinsic contamination of $\nu_e/\overline{\nu_e}$ at a level of 0.5% at energies below 1.5 GeV. A significant portion of the intrinsic ν_e flux, approximately 51%, stems from the decay chain of pions to muons and subsequently to electrons, characterized by the process $\pi \to \mu \to e + \nu_e + \nu_\mu$.

2.3 The NuMI beam

The NuMI (Neutrinos at the Main Injector) beam facility is the world's existing most powerful neutrino beam, producing neutrinos by directing a 120 GeV proton beam onto a narrow graphite target approximately 1 m long [49]. The resulting hadrons are focused forward and charge-selected by two magnetic horns before entering a long decay pipe where most decay into neutrinos.

The protons are initially H^- ions accelerated to 400 MeV in the Linac, then converted to protons in the Booster and accelerated to 8 GeV in 1.6 μs long batches with a 53 MHz bunch spacing. The Main Injector, seven times the circumference of the Booster, accommodates storage and acceleration of 6 Booster batches, with one slot reserved for pulse kicker rise time. After impacting the graphite target, the produced hadrons are focused by two magnetic horns and travel along a 675 m long decay pipe. Pions and kaons, major constituents of the hadrons, predominantly decay into muon neutrinos, forming the primary ν_μ beam. Additionally, a few percent of $\overline{\nu_\mu}$ component arises from negative hadrons, with a minor contamination of electron neutrinos (ν_e) due to subdominant decay modes. At the end of the decay pipe, an hadron monitor and an absorber are placed. These are followed by 240 m of rock stopping the remaining muons in the beam. In Figure 2.5 the individual components of the NuMI beam are shown (not to scale). NuMI can deliver up to 6.5×10^{20} protons per spill, with a beam pulse width of 9.6 μs.

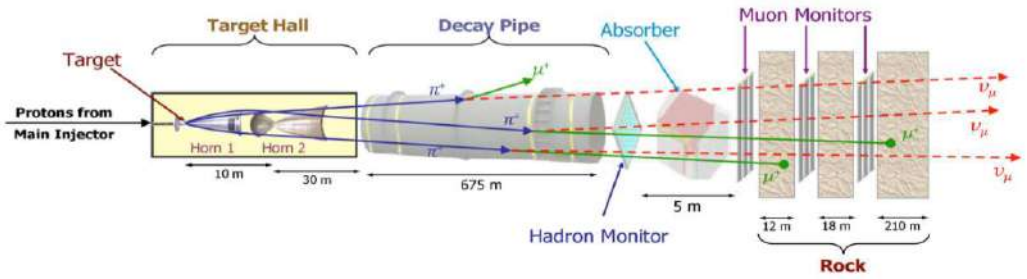

Figure 2.5: Schematic of the NuMI Beam [49].

The ICARUS detector is located 795 meters away from the NuMI neutrino beam, at an angle of 5.7 degrees off-axis. Event rates for muon neutrinos are similar to those in the Booster beam, while the electron neutrino component is enhanced in the off-axis beam. The expected neutrino (left) and antineutrino (right) fluxes at the SBN far detector are shown in Figure 2.6.

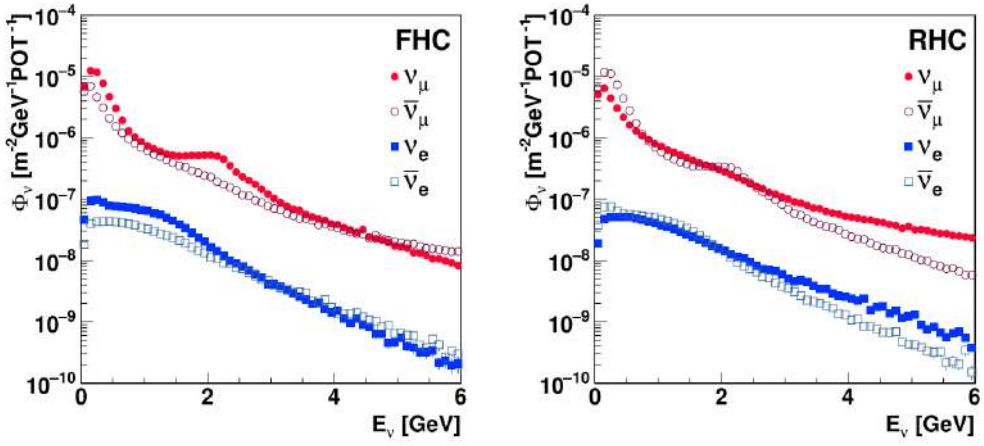

Figure 2.6: NUMI beam flux at the SBN far detector, for Forward Horn Current or FHC (left) and Reverse Horn Current or RHC (right).

2.4 The Liquid Argon Time Projection Chamber

In neutrino experiments, a commonly employed detection technique involves the use of scintillating materials that emit photons ("luminescence") when exposed to ionizing radiation [50]. Many experiments in the neutrino sector use liquid argon (LAr) as scintillator, in one or more Time Projection Chambers (TPCs) to achieve high resolution three-dimensional particle reconstruction. Carlo Rubbia's late 1970s proposal [51] of the LArTPC marked the beginning of its widespread use in particle physics for neutrino detection, due to several properties of liquid argon:

- it is dense (1.4 g/cm^3);
- it does not attach electrons and hence it permits long drift-times;
- it has an high electron mobility;

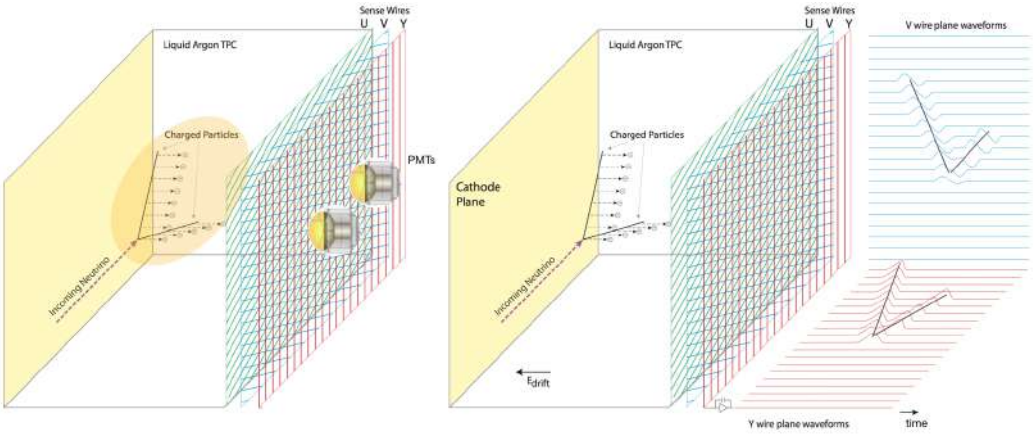

Figure 2.7: Operating principle of the liquid argon time projection chamber neutrino detector.

- it is cheap and easy to obtain, as Ar is the third most abundant gas in Earth's atmosphere ($\sim 1\%$);
- it is easy to purify, as many of the organic impurities are frozen out from its liquid form;
- it is inert and it can be liquified with liquid nitrogen.

The general TPC concept [52], originally envisioned using a noble gas as medium, was presented a few years earlier Rubbia's article to address the need for both high-precision spatial measurements and clear three-dimensional position reconstruction. To date, numerous experiments have employed this technology: ICARUS T600, MicroBooNE, LArIAT, and ProtoDUNE among others. The working principle of the device is illustrated in Figure 2.7 [45].

The detector consists of a large active volume of highly purified liquid argon (87 K), surrounded by an high voltage cathode plane on one side and an anode surface at the opposite side. Neutrino interactions with argon nuclei, via CC or NC weak interactions, produce charged particles that ionize and excite the argon atoms while propagating in the medium. An electric field between the cathode and the anode planes, made uniform by a field cage surrounding the argon volume, causes the drift of the generated free charges. These drifting electron clouds induce signals in closely spaced wires (3-5 mm pitch) arranged in planes on the anode side. Electron drift speeds are relatively slow, about 1.6 mm/μs, needing a continuous readout over 1-2 milliseconds for a typical 2-3 meter wide detector. At the anode side the detector is instrumented with three distinct layers of wires, oriented at different angles, to reconstruct a 3D view of the particle trajectory. The first

two layers, arranged to form a grid, allow for a 2D projection of the particle path in the two coordinates perpendicular to the drift direction. These layers, referred to as induction planes, are biased to remain transparent to the drifting electrons, that are then collected by the third layer. Calorimetry measurements are given by the total charge accumulated on the third layer, i.e. collection plane, which is proportional to the energy lost by the particle. The drift time of the electrons is finally used to reconstruct the third coordinate. For this purpose it is used the release of scintillation light by LAr in the ionization process. The scintillation photons produced are proportional to the energy deposited by the ionizing particle. In absence of a drift field, LAr has a light yield of approximately 40000 γ for every MeV of energy deposited. However, under a 500 V/cm drift field, this yield decreases to about 24000 γ per MeV, due to a significant reduction in the recombination process. This light, emitted in the vacuum ultraviolet spectrum (λ = 128 nm, E = 9.69 eV), provides the initial timing (t_0) for interactions. The third spatial coordinate of the ionization point is determined by the time difference between the start of the event (indicated by prompt scintillation light detection) and the signal production on the wires. The described detector is therefore a totally active, precise-sampling calorimeter capable of tracking particles with O(1 mm) spatial resolution.

This technology, pioneered by the ICARUS project, has evolved into a mature technology after decades of global research and development. It is currently employed in Fermilab's operational MicroBooNE detector and is also being implemented in the under-construction SBND detector.

2.5 MicroBooNE

The MicroBooNE detector started operating in 2015 and completed its original program. Subsequently, it has then been integrated into the SBN Program as an intermediate detector [50]. The experiment took data along the Booster Neutrino Beamline at Fermilab, maintaining the same configuration that delivered neutrino and anti-neutrino beam to MiniBooNE for over a decade, thereby reducing systematic uncertainties in comparative data analyses [47]. One of its physics goals is to investigate the MiniBooNE LEE: being a Cherenkov based detector, MiniBooNE was limited by photon misidentification background (see Section 1.5.3) while MicroBooNE, using the LArTPC technology has thus the capability to identify ν_e CC interactions.

The detector's core, a single 86-ton LAr TPC measuring $2.325 \times 2.560 \times 10.368$ m^3, is enclosed within a cylindrical cryostat with a 41 cm thick foam insulation layer to maintain cryogenic temperatures. Its design, shown in

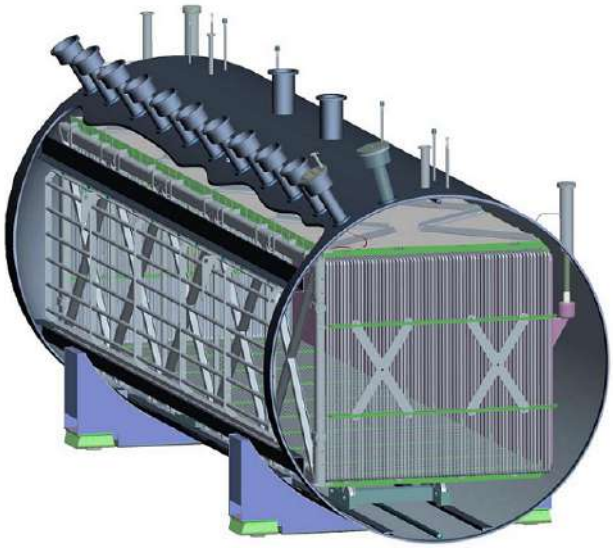

Figure 2.8: The MicroBooNE LArTPC, within the cylindrical cryostat.

Figure 2.8 [53], mirrors that of ICARUS T600's drift volumes, featuring a cathode composed of nine stainless steel panels and a high voltage (HV) feedthrough. The TPC itself is defined by 64 field cage loops spaced 4 cm apart center-to-center, connected by a resistor chain that helps to generate a uniform drift field across the detector. The Anode Plane Assemblies (APAs) contain three layers of parallel wire planes, two induction planes at angles of +60° and -60° relative to vertical, and a collection plane with vertical wires. These planes, spaced 3 mm apart, are biased at -200, 0 and 400 V, respectively, working together with a nominal cathode bias of -128 kV to create an electric field of 500 V/cm. This allows a maximum drift time of 1.6 ms. A stopping muon candidate decaying into a Michel electron, recorded by the MicroBooNE collection plane, is shown in Figure 2.9 [50]. A distinctive feature of MicroBooNE is its cold electronics system, which comprises application-specific integrated circuits (ASICs) for signal processing. These circuits, which combine pre-amplifiers, digitizers, signal shapers, and multiplexers, are mounted directly on the APA support frames within the LAr, differently with respect to the ICARUS T-600 setup [54]. This system significantly reduces the readout noise, thus improving the signal-to-noise ratio. The light collection system, essential for timing and triggering, includes an array of 32 8-inch Hamamatsu R5912-02MOD PMTs and a secondary system of lightguide paddles. This secondary system has been installed in MicroBooNE primarily for R&D studies for future large-scale detectors.

Located near the Earth's surface, the MicroBooNE detector is signifi-

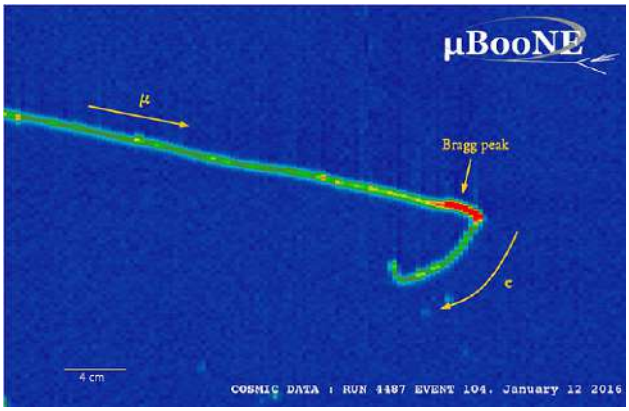

Figure 2.9: A stopping muon and associated Michel electron candidate as recorded by the MicroBooNE collection plane.

cantly affected by a high rate of cosmic ray muons at 5 kHz [55]. Due to a relatively long readout window of 2.2 ms for collecting drifting charges, nearly twice the SBND one, MicroBooNE typically detects signals from an average of 24 cosmic rays during each 4.8 ms data acquisition window. To mitigate this, a Cosmic Ray Tagger (CRT) system was implemented after the initial data run. This system comprises 73 scintillating modules, made from plastic scintillating strips, positioned on the top, bottom, and along the sides parallel to the neutrino beam, achieving an 85% coverage of the TPC.

The MicroBooNE detector operated from February 2016 to March 2020, collecting neutrino beam physics data across five separate Runs. MicroBooNE's half-decade of operation has supported a robust analysis program covering a wide array of topics, including single-particle and electromagnetic shower reconstruction, energy response calibration, background identification and rejection, vertex identification, and innovative uses of neural networks for event reconstruction. Recently, the collaboration released findings from a series of searches focused on the MiniBooNE LEE. These studies investigated various final-state topologies in CC ν_e interactions and NC Δ resonance decays that produce a single photon. The results suggest that the MiniBooNE low-energy excess is unlikely to be due only to additional ν_e interactions, and a more complex explanation is needed [56]. The analysis, using data from February 2016 to September 2018 (Runs 1 to 3), corresponding to $\sim 6.4\times10^{20}$ POT from the BNB, showed no evidence supporting sterile neutrino oscillations. The resulting exclusion contours are presented in Figure 2.10 [56]. Although these results exclude some of the sterile neutrino parameter regions allowed by past experimental anomalies, they do not conclusively exclude the 3+1 neutrino model.

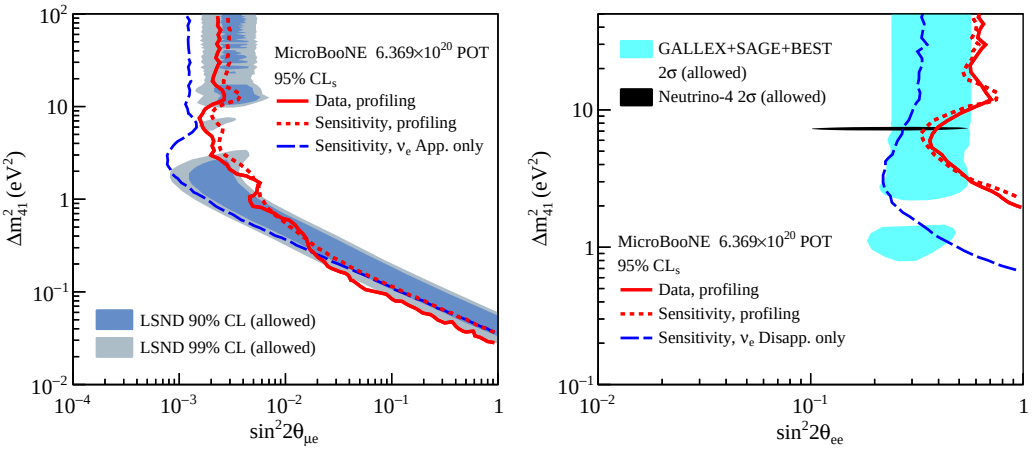

Figure 2.10: MicroBooNE exclusion countours s at the 95% CL in the $\nu_\mu \to \nu_e$ appearance (left) and $\nu_e \to \nu_e$ disappearance channels.

2.6 The SBN Near Detector: SBND

The Short-Baseline Near Detector will be the future near detector in the SBN Program on the Booster Neutrino Beamline, and will measure the unoscillated neutrino flux. The detector layout is shown in Figure 2.11 [57]. Its multi-component system is based on three different detectors: the Time Projection Chamber, the Photon Detection System (PDS) and an external Cosmic Ray Tagger [58].

The TPC, positioned inside a liquid-argon-filled cryostat, measures 4m (W)$\times$ 4m (H) $\times$ 5m (L) along the beam direction. At its core, it features an opaque cathode plane (CPA) surrounded by two sets of Anode Plane Assemblies (APAs) on each side. These create two drift volumes, each two meters in length, where ionized electrons drift under a strong electric field of 500 V/cm provided by a -100 kV bias on the cathode. This setup achieves a maximum drift time of 1.28 ms. Each APA side hosts three layers of wires: two induction planes with wires angled at $\pm 60°$ and one vertical collection plane (see Figure 2.12), with a total of 11,264 wires at 3 mm pitch. The readout electronics for the detector are made up of a system that includes custom-built pre-amplifiers, commercial Analog-to-Digital Converters (ADCs), and motherboards with onboard Field-Programmable Gate Arrays (FPGAs). These components, installed on the frames, are connected to the end of each wire plane and are designed to operate within the liquid argon environment. The entire TPC is encased in a stainless steel membrane cryostat, which will be filled with liquid argon. This design is similar and serves as a prototype for

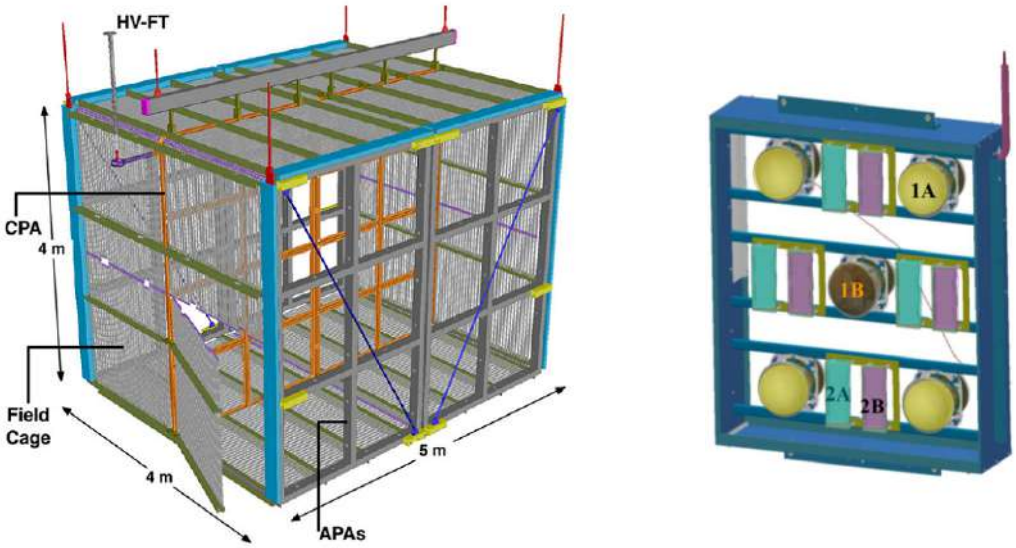

Figure 2.11: (Left) SBND LArTPC and main components: the cathode plane assembly (CPA), the wire-based anode plane assemblies (APAs), the field cage and the HV-FT (high voltage feedthrough) [50]. (Right) Photon Detection System module, equipped with two types of sensors: **1** PMTs and **2** X-ARAPUCAs, each with two variants, **A** sensitive to direct scintillation light; **B** sensitive to reflected light by the CPA.

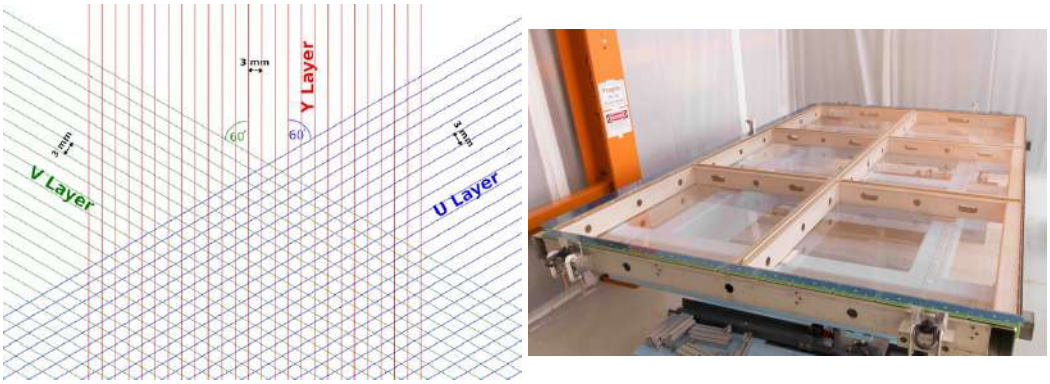

Figure 2.12: (Left) A schematic layout of the wire planes in SBND, showing the U (innermost) and V (middle) induction planes with wires at +60° and -60° to vertical respectively, and the Y (outermost) collection plane with wires orientated vertically [50]. (Right) One of four completed SBND anode planes [45].

the cryostat used in the DUNE experiment [59]. The assembly was completed in June 2022 within a clean room tent at a separate facility.

Located behind the APAs, the PDS consists of 24 modules (12 per side), incorporating tetraphenyl butadiene (TPB)-coated reflector foils on the cathode to shift the wavelength of detected scintillation light. Each module contains 5 8-inch Hamamatsu R5912-mod Cryogenic PMTs and 8 X-ARAPUCAs, for a total of 120 PMTs and 192 X-ARAPUCAs across the system. The PDS, which completed installation in September 2022, captures scintillation light within the TPC and employs TPB coatings on strategically placed PMTs and X-ARAPUCAs for enhanced light collection and reflection. This configuration not only ensures uniform light yield but also provides excellent timing resolution.

As SBND is located on the surface, it is exposed to an high flux of cosmic rays. The CRT system is designed to mitigate the cosmic ray background surrounding the detector on all six sides, identifying cosmic rays that enter, exit, or pass through the LArTPC, using 135 single modules of extruded scintillator strips read by Silicon Photomultipliers (SiPMs). A "muon-beam telescope" setup of CRT modules has already been temporarily implemented at the cryostat's upstream and downstream walls to facilitate the commissioning, before the liquid argon phase begins. The complete CRT installation is planned as the final step, although the bottom CRT panels below the cryostat are already installed. With an unprecedented ν-Ar interactions sample size, the SBND will provide critical insights for future LArTPC neutrino experiments, observing 5000 ν-events per day, and totaling approximately 1.5

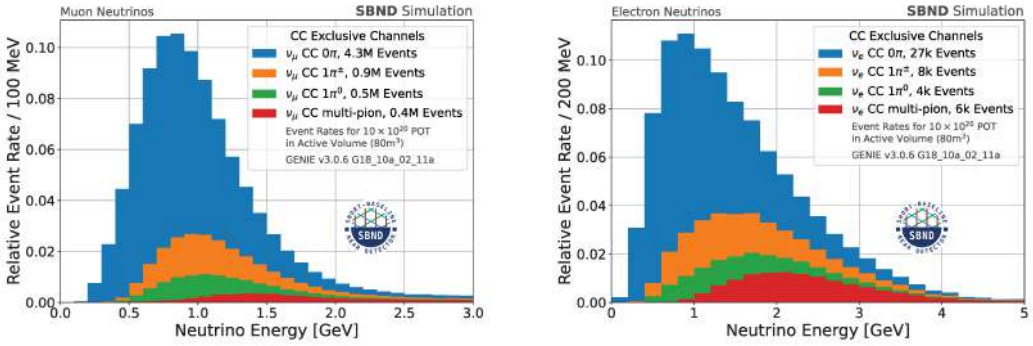

Figure 2.13: Expected event rate of muon (left) and electron (right) neutrinos in SBND during 4 years of data collection, separated by interaction channel.

million ν_μ CC events and 12000 ν_e events annually (see Figure 2.13) [58].

2.7 The SBN Far Detector: ICARUS T-600

The ICARUS T600 detector, which comprises two cryostats holding liquid argon time projection chamber modules and photodetectors, will serve as the Short-Baseline Program Far Detector. ICARUS is the farthest from the BNB target, at a distance of 600 meters and it is the largest of the SBN detectors.

Initially deployed from 2010 to 2013 at the Gran Sasso National Laboratory (LNGS) in Italy, ICARUS was the first large-scale LAr-TPC to operate continuously as a general-purpose observatory [47]. During its operation, it successfully demonstrated high-purity, underground operation, conducted measurements of neutrino velocity, and explored neutrino oscillations using the CERN Neutrino to Gran Sasso (CNGS) beam [45]. Following its long run at the LNGS, ICARUS underwent significant overhauling at CERN in the years 2015-2017, before being transported to Fermilab in July 2017. The final installation in Fermilab's SBN far detector building was completed in August 2018.

To mitigate cosmic-generated backgrounds similar to the near detector, ICARUS is equipped with a segmented cosmic ray tagging system composed of plastic scintillation slabs read by SiPMs, and a 3 m concrete overburden on top. The ICARUS commissioning was concluded by June 2022, and the first physics run officialy began on the 9^{th} of June 2022.

A more detailed description of the ICARUS detector is provided in Chapter 3.

Chapter 3

The ICARUS detector

3.1 The ICARUS Time Projection Chamber

The ICARUS detector, a 470-ton active mass LArTPC, is a crucial part of the SBN program and represents a milestone in the demonstration of LArTPC technology for neutrino physics. Positioned 600 m from the BNB proton target, a detector schematic is shown in Figure 3.1.

ICARUS is divided into two identical T-300 cryostat modules. Within each module, there are two TPCs with three parallel wire planes, spaced 3 mm apart. The wire orientation, horizontal for the first plane and $\pm 60^{\circ}$ for the other two, was designed for an optimal detection of cosmic rays, which predominantly enter from above and exit downward, maximizing interaction with the horizontal wires. This orientation is different from the vertical setup typically found in other SBN detectors and was chosen based on ICARUS's original design as a cosmic ray detector.

As in other SBN detectors like SBND and MicroBooNE, ICARUS uses an appropriate bias voltage to create a non-destructive readout from the ionization charges in the first two planes (Induction 1 and 2 planes), while the ionization charges are fully collected in the last plane. The active volume of each T300 half-module is 18.0 m long, 3.2 m high, and 3.0 m wide.

The TPCs within each module are separated by a common central cathode consisting of a stainless steel frame and punched stainless-steel sheets, providing 58% optical transparency. The ICARUS TPC is instrumented with 360 PMTs with wavelength shifters to detect the VUV scintillation light and to provide the event time and the trigger. The maximal drift length in the TPCs is 1.5 m, corresponding to a drift time of ~ 0.96 ms at the nominal drift field of 500 V/cm. The readout electronics are located outside the detector.

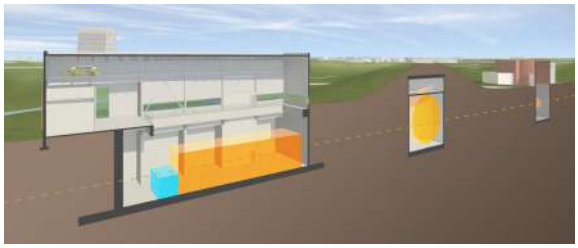

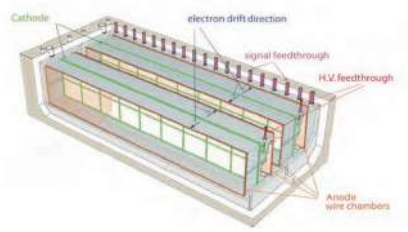

Figure 3.1: (Left) The ICARUS-T600 detector building concept. The neutrino beam center is indicated by the orange dashed line and enters from the right. The existing MiniBooNE and MicroBooNE buildings are also shown. (Right) ICARUS-T600 detector schematic.

3.2 ICARUS at LNGS

The first large-scale experiment conducted by the ICARUS Collaboration at the LNGS underground laboratory demonstrated the potential of LArTPCs for 3D imaging and calorimetric reconstruction of ionizing events [54].

The detector, pre-assembled and tested in Pavia, was transported in 2004 to Hall B of the LNGS (see Figure 3.2) [47]. It became operational in early 2010, collecting data from both the CNGS neutrino beam and cosmic rays. By 2013, ICARUS had successfully completed a three-year run collecting 3000 neutrino events on the CNGS beam (8.6×10^{19} POT), proving the feasibility of LArTPC technology at the kiloton scale in a deep underground setting. This success paved the way for the development of next-generation neutrino oscillation experiments like DUNE.

The primary objectives of this physics run included studying neutrino oscillations via the CNGS beam and searching for atmospheric neutrino interactions and proton decay. ICARUS searched for an excess of electron neutrinos related to the LSND anomaly, analyzing 2650 neutrino interactions from a 7.9×10^{19} POT exposure. This analysis restricted the LSND signal to a narrow parameter region at $\sin^2 2\theta \sim 0.005$ and $\Delta m^2 < 1$ eV^2, necessitating further investigation [60].

Maintaining the purity of liquid argon (LAr) is crucial for ensuring the accurate measurement of energy deposition from ionization charge signals in collected events, necessitating continuous monitoring of the free electron lifetime in LAr as a critical indicator of this purity [61]. By 2013, the purity had improved allowing a 16 ms electron lifetime, corresponding to a 20 parts per trillion (ppt) O_2 equivalent contamination in LAr, demonstrating the potential for constructing larger LAr-TPC detectors with up to 5 m drift distances [62].

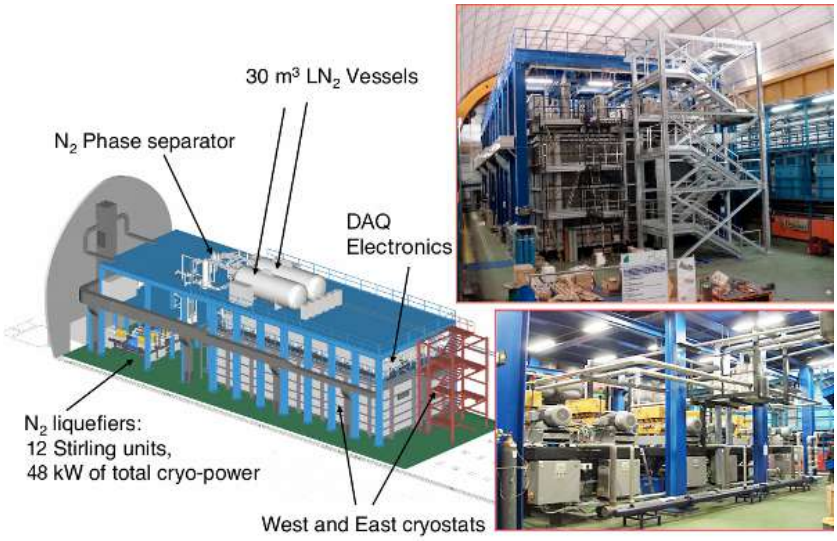

Figure 3.2: Left: schematic view of the whole ICARUS plant in Hall B at LNGS. Right-top: photo of the detector installation. Right-bottom: details of the cryo-cooler plant.

The high-resolution and granularity of the detector, providing a resolution of ~ 1 mm^3 over an active volume of 340 m^3, allowed the particle identification through the analysis of event topology and energy deposition per track length (dE/dx) based on particle range [63]. The momentum of escaping muons was measured by means of multiple Coulomb scattering (MCS), crucial for reconstructing muon neutrino charged-current (ν_μCC) events in the absence of a magnetic field. An average resolution of 15% was achieved in the 0.4-4 GeV energy range relevant for the SBN experiment [64]. Additionally, the high sampling density ($\sim$ 2% of a radiation length) and the excellent signal-to-noise ratio of about 10/1 on individual wires allowed an excellent e/γ separation, crucial for identifying ν_eCC interactions. Finally, the study of events related to cosmic rays led to the identification and reconstruction of 6 ν_μCC and 8 ν_eCC events from a 0.43 kton·y exposure, confirming the feasibility of automatic searches for ν_eCC in the sub-GeV range, crucial for the study of the BNB neutrinos at FNAL and future long baseline neutrino experiments [65].

3.3 ICARUS overhauling at CERN

To prepare the detector for data collection for the SBN program and its non-underground operations at FNAL, ICARUS was disassembled at the end of

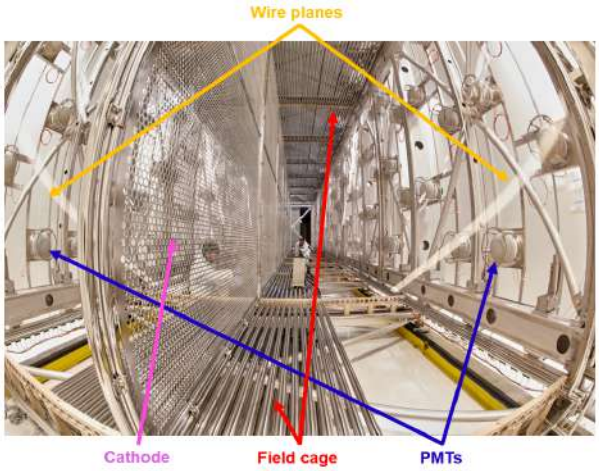

Figure 3.3: Inner view of one of the ICARUS modules, during its overhauling at CERN. The TPCs are visible, separated by the cathode at the center. The wire planes and the PMT system behind, can be seen on the right.

its operations at LNGS and transported to CERN for an intensive overhaul before being shipped to the current location at Fermilab. This overhaul, part of the CERN WA104 project, aimed to preserve most of the existing operational equipment while integrating updated technology. The refurbishment included the construction of new cold vessels for liquid argon (LAr) containment with purely passive insulation, similar to the technology used in the SBND. It also involved a comprehensive review and maintenance of the cryogenics and LAr purification equipment. The TPC cathode was flattened and a new light collection system was implemented to enhance event localization and differentiate beam events from cosmogenic backgrounds. Finally, the detector was equipped with higher-performance TPC read-out electronics, along with updated slow control systems and cabling [54]. A picture of the ICARUS TPC during the refurbishing operations is shown in Figure 3.3.

3.4 ICARUS at FNAL

After its overhaul at CERN, ICARUS was transported to Fermilab and installed in the SBN far detector experimental hall by August 2018. In Figure 3.4 different installation stages of the ICARUS detector are shown [54]. Following installation, efforts focused on setting up and testing all primary subsystems before the cryogenic commissioning. Thanks to a joint effort between CERN, INFN, and Fermilab the ICARUS cryogenic plant was designed, con-

Figure 3.4: (Left) Deployment of the ICARUS cryostats in the pit of the SBN Far Detector experimental hall at Fermilab occurred in August 2018. (Center) The installation of TPC, PMT, and laser feed-through flanges followed in December 2018. (Right) The ICARUS detector was ready at the start of data taking for commissioning.

structed, and installed at Fermilab, based on the proven reliability of the previous system at LNGS. While the overall design followed that of LNGS, significant updates were made, particularly to the cryogenic and purification systems. Notably, the re-liquefaction system at Fermilab operates on an open loop, venting nitrogen gas to the atmosphere, in contrast to the closed-loop system used at LNGS. The cryogenic plant became fully operational by July 2019, with the installation of the TPC electronics and PMT systems completed. Cryogenic commissioning began in February 2020, culminating in the full stabilization of the system by May 2020 after the completion of liquid argon filling. During this phase, the detector was closely monitored, and preparations were made for data collection.

Detector activation took place by August 2020, with the TPC wire planes and cathode high voltage being brought to nominal settings (-75 kV for the cathode). Data collection started with a random 5 Hz trigger, focusing on cosmic-ray interaction events for calibration. The electron lifetime, namely the LAr purity, was continuously monitored since the commissioning and during the physics runs as shown in Figure 3.5: except for variation above the error bars due to maintenance of argon pumps, the purity has a steady behaviour with a value > 3 ms which ensure a precise reconstruction of ionizing events [61]. ICARUS TPC and light collection system became fully operational in June 2021, marking the start of neutrino data collection.

A visual study campaign of the collected events was initiated to identify and analyze neutrino interactions. An example of a ν_μCC candidate is shown in Figure 3.6. The visual scanning also allowed the identification of the first ν_eCC candidates in the NuMI beam, as shown in Figure 3.7. The commissioning phase of the ICARUS detector was concluded on June 1st, 2022, setting the start for the physics run data taking. More details on the detector initial operations can be found in [54].

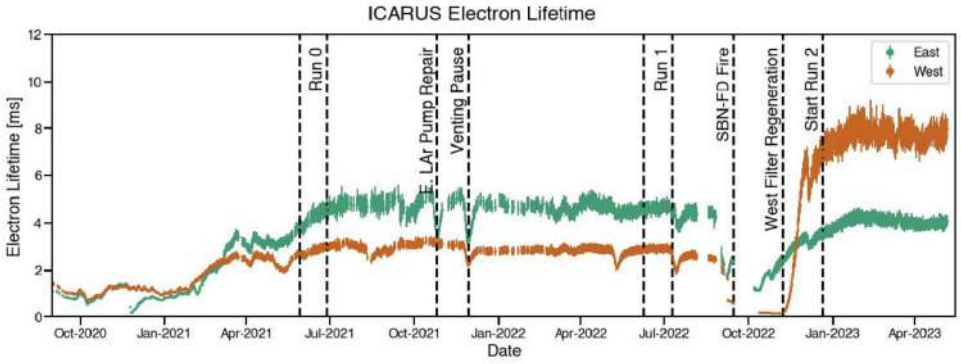

Figure 3.5: Electron lifetime evolution, monitored during ICARUS operations for both cryostats.

3.4.1 TPC electronics

To address the higher data rates at FNAL, with respect to the operations at LNGS, the overhaul at CERN included designing new electronics for the 53,348 wire-channels [54]. Maintaining the core architecture of the original system, the upgrade introduced a more sophisticated design with each channel now featuring a dedicated serial 12-bit ADC, and integrating both analog and digital components into a single electronic module for 64 channels. The system also moved from VME (Versa Module Eurocard) to a serial bus architecture with optical links for gigabit-speed data transmission. Modifications were also made to the cryostat's flanges to accommodate new electronic modules and Decoupling Biasing Boards (DBBs), crucial for wire biasing and signal transfer. The redesign significantly reduced space, with nine A2795 boards now compactly housed in a "mini-crate", as shown in Figure 3.8, mounted onto each chimney's feed-through flange, connected through two fibers [54]. The entire system of 96 mini-crates is synchronized by a serial link cable that transmits clock, trigger, and command signals.

3.4.2 The Photon Detection System

In the ICARUS detector, scintillation light is primarily generated by the excitation and ionization of argon atoms when charged particles deposit energy in liquid argon. The amount of scintillation light increases with the recombination of electron-ion pairs, a process inversely proportional to the applied electric field strength. Scintillation light in LAr is emitted following the radiative decay of excited argon molecules (Ar_2^*), which produce monochromatic VUV photons with a wavelength $\lambda \simeq 128$ nm from transitions from

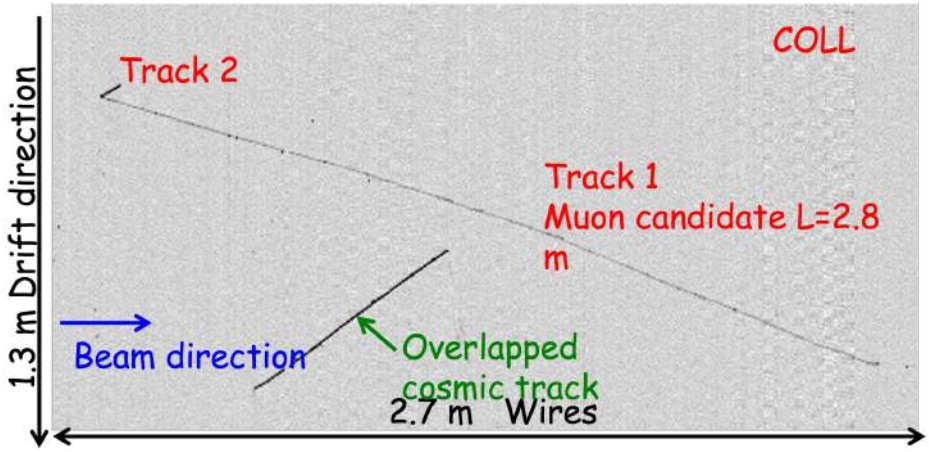

Figure 3.6: A visually selected ν_μCC candidate from the BNB, with an estimated total deposited energy of $\sim$ 1.1 GeV. The muon candidate is 3.8 m long, while the highly ionizing track was identified as a 20 cm proton track.

the lowest excited molecular state to the dissociative ground state [47]. This light emission includes both fast ($\tau_{fast} \sim 6$ ns decay time) and slow ($\tau_{slow} \sim 1.6$ μs) components.

The overhaul at CERN upgraded the ICARUS light detection system for shallow depth operations, enhancing its ability to detect photons from LAr scintillation and accurately localize tracks along the detector's 20-meter length with a resolution better than 1 meter (time resolution of around 1 ns). This allows the system to provide precise absolute timing for each track and to accurately identify specific events in coincidence with the BNB and NuMI beam spill gates. The system now includes 360 8-inch Hamamatsu R5912-MOD photomultiplier tubes deployed behind the wire chambers, with 90 PMTs per TPC [66]. To enhance their sensitivity to VUV light, each PMT is coated with ≈ 200 μg/cm^2 of TPB. The PMTs are mounted onto the wire chamber frames, positioned about 5 mm behind the collection planes' wires, and are surrounded by a stainless steel grid cage to provide electrostatic shielding and prevent spurious signals on the wire planes. Additionally, the setup includes a laser calibration system to maintain PMT gain equalization and timing accuracy, allowing for monitoring and maintenance of system performance [67]. An example of a PMT signal showing the characteristic fast and slow light components is illustrated in Figure 3.9.

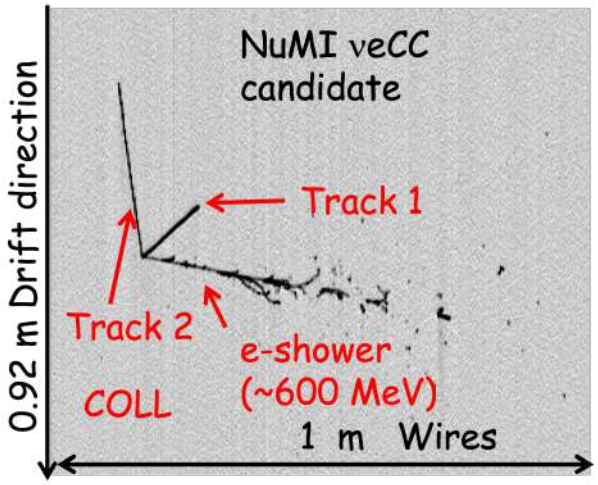

Figure 3.7: A visually selected ν_eCC candidate from the NuMI beam, with a total deposited energy of $\sim$ 600 MeV.

3.4.3 Trigger

With an expected rate of 40,000 events per day (considering also non-physical ones), the ICARUS detector processes a significant volume of data [68]. This rate is influenced by the intensities, spill windows, and repetition rates of the BNB and NuMI beams. Specifically, BNB has a nominal intensity of 5 $\times$ 10^{12} POT per spill in a 1.6 μs spill window at a 4 Hz rate. On the other hand NuMI has 6.5 $\times$ 10^{13} POT per spill over 9.5 μs at 0.83 Hz. Monte Carlo simulations indicate that one neutrino event is expected in the active volume every 180 BNB spills and every 53 NuMI spills. An higher rate of background cosmic events is expected, once every 55 (BNB) and 7 (NuMI) beam spills for "in-time" cosmics, i.e. cosmic particles entering in the detector during the neutrino beam spill.

To manage this data efficiently, ICARUS employs an online trigger system, using the prompt scintillation light signal detected by the PMTs in coincidence with the beam spill windows. The system's 90 PMTs per TPC are connected through six CAEN V1730B boards, which digitize 15 PMT signals (channels) per board covering 3 m longitudinal sections of a TPC. These signals are written in a 10 μs wide circular buffer, to readout both fast and slow scintillation light components of each PMT. The generation of beam spill gates is based on receiving "*Early Warning*" signals 35 ms and 730 ms before BNB and NuMI beam protons hitting the target, respectively. The precise synchronization of the detector subsystems is possible

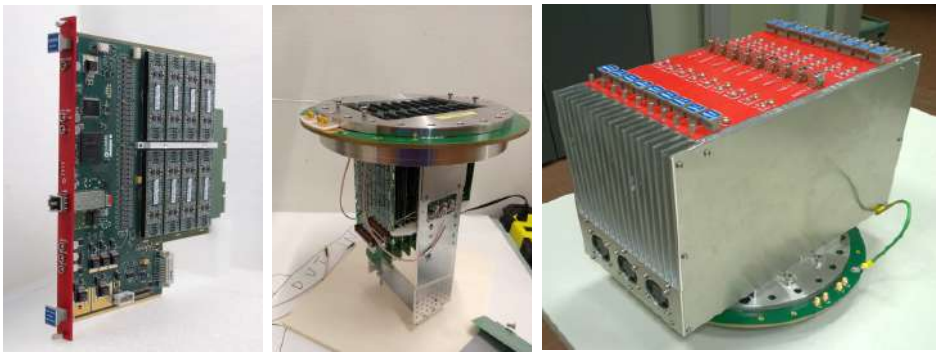

Figure 3.8: (Left) A2795 custom board housing 64 amplifiers, AD converter, digital control, and optical link. (Center) An assembled feed-through with nine DBBs and the biasing cables. (Right) A mini-crate populated by the nine A2795 boards installed on a feed-through flange.

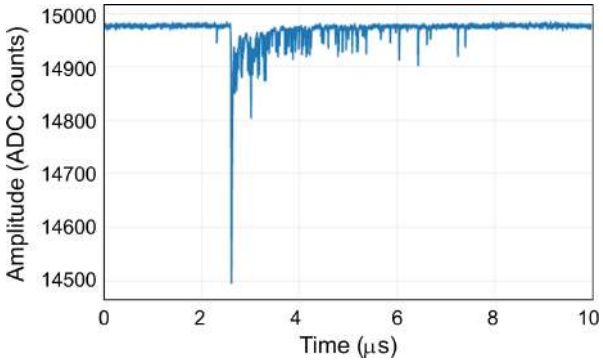

Figure 3.9: PMT signal recorded by the light detection system electronics.

via a network known as White Rabbit [69], that ensures ns-accurate signal distribution. For each PMT channel an internal trigger-request logic signal starts when the PMT pulse exceeds a set threshold. For each pair of adjacent PMT channels, trigger request are combined with an OR logic, producing a low-voltage differential signaling (LVDS) output. This LVDS signal is processed by a FPGA board, that controls the activation of the read-outs across ICARUS's various subsystems. The Icarus *Global Trigger* is generated when a specified number of LVDS signals from the same TPC, i.e. majority, are in coincidence with a beam gate window. The beam gate windows are set to 2.2 μs for BNB and 10.1 μs for NuMI, with a small enlargement with respect to the beam spill to ensure that all interactions within the spill are captured.

In presence of a global trigger signal, 1.5 ms and 30 μs acquisition windows are activated for the TPC and PMT signal recording, respectively.

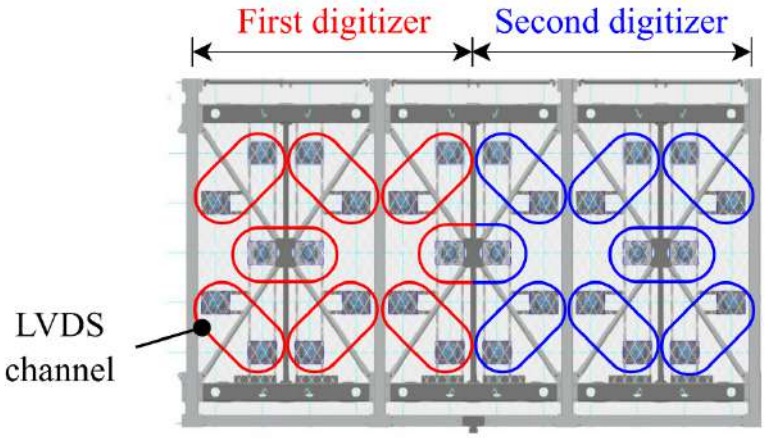

Figure 3.10: Single 6 m section of the TPC. The PMT positions are shown, together with the pairs providing the LVDS output signal.

Additionally, 2 ms and 50 ms windows are acquired for PMT waveforms and CRT signals, respectively, to recognize and tag cosmic rays during the drift time of the TPC. The 18 meters long TPC walls are subdivided into three consecutive 6-meter sections, each with 30 PMTs, as can be seen in Figure 3.10 [70]. In each of opposite facing slices (see Figure 3.11) a majority of 5 LVDS signals, with 8 photo-electrons (p.e.) discrimination threshold and an OR of two adjacent PMTs, has been required to produce a PMT trigger signal ("Majority-5"). The system efficiency was evaluated with Monte Carlo simulations, showing an average efficiency $> 99.5\%$ for BNB ν_μ events. Improvements were made after the first physics run, that included an overlapping window logic adding two new 6-meter windows. This resulted in an improved efficiency to above 99.9% for these events, considering a Majority-5 trigger.

Another trigger implemented for calibration purposes, is the so called BNB and NuMI Minimum Bias trigger. The Minimum Bias generates triggers at the beam gate time regardless of light activity.

3.4.4 Cosmic ray mitigation and tagging

The ICARUS-T600 detector was initially designed to operate in the low muon cosmic background of the Gran Sasso laboratory. The conditions at FNAL are completely different: placed just below the surface the detector is subject to a significant cosmic ray background and this may induce several additional and uncorrelated triggers during the ~ 1 ms drift time. Simulations showed

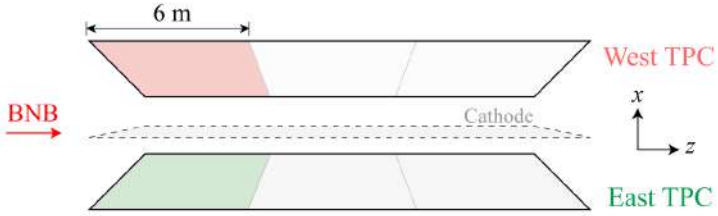

Figure 3.11: View from the top of the West ICARUS T300 module. The front-facing sections of the TPCs are shown.

that the expected rate of cosmics depositing more than 100 MeV within the T600 active volume is of $\sim$ 11 kHz [71].

Cosmic particles entering the detector during the 1.6 μs BNB neutrino beam-spill interact in the liquid argon generating scintillation light and an event trigger, the so-called *in-time activity*. The *out-of-time* cosmic activity corresponds to cosmic muons crossing the detector during the $\sim$ 1 ms TPC drift time. On average $\sim$ 11 cosmic tracks are expected over the full T600 volume during the drift time window, generating a background that has to be disentangled from the neutrino event tracks. One of the most important sources of background to the ν_e appearance analysis is due to electromagnetic showers induced by γ produced by cosmic particles propagating through the detector and in the surrounding materials. By showering withing the active liquid argon volume, the cosmogenic photon can mimic a genuine ν_eCC interaction [72]. Without systems in place to mitigate cosmic rays, the detector would be unable to effectively conduct any meaningful search.

In order to mitigate the cosmogenic induced background, the ICARUS T600 detector is indeed surrounded with an external Cosmic Ray Tagger system below a 3 m concrete overburden (6 m water equivalent).

A more detailed description of the ICARUS Cosmic Ray Tagger system (CRT) is provided in Chapter 4.

3.5 ICARUS physics operations

ICARUS is the only detector in the SBN program currently taking data (*Run 3*). In previous years ICARUS collected a large statistic sample of physics quality data during *Run 1* (June - July 2022) and *Run 2* (December 2022 - July 2023) collecting a total statistics of 2.51×10^{20} POT for BNB and 3.48×10^{20} POT for NuMI beams. The experiment, in a standalone physics program, is exploring the potential presence of a sterile neutrino signal, initially indicated with a 2.7σ C.L. by the Neutrino-4 reactor experiment. A

Neutrino-4 oscillation signal with best fit parameters $\delta m^2 = 7.25eV^2$ and $\sin^2(2\theta) = 0.26$ should be visible by the ICARUS detector in both ν_μ and ν_e disappearance channels, as a function of L/E averaged over the pion decay tunnel length. The top plot in Figure 3.12 shows the survival oscillation probability of ν_μ in the presence of the Neutrino-4 anomaly, using data expected from ICARUS after three months of data collection with the BNB ($\sim$ 11500 ν_μCC events). By using the enhanced ν_e signal contribution of the NuMI beam, the bottom plot in Figure 3.12 is obtained, showing the result of the analysis with the expected $\sim$ 5200 ν_eCC interactions with a fully contained electromagnetic shower, after one year of data taking [73]. The ongoing Neutrino-4 analysis is a major focus for the ICARUS collaboration, using data from Run 1 and 2 to understand detector performance and provide robust physics results. Visually selected $\sim$ 1500 ν_μCC events candidates from Run 1 and 2, are now being exploited to develop an automated event selection scheme, evaluate its performance and address some of the major event reconstruction issues [68].

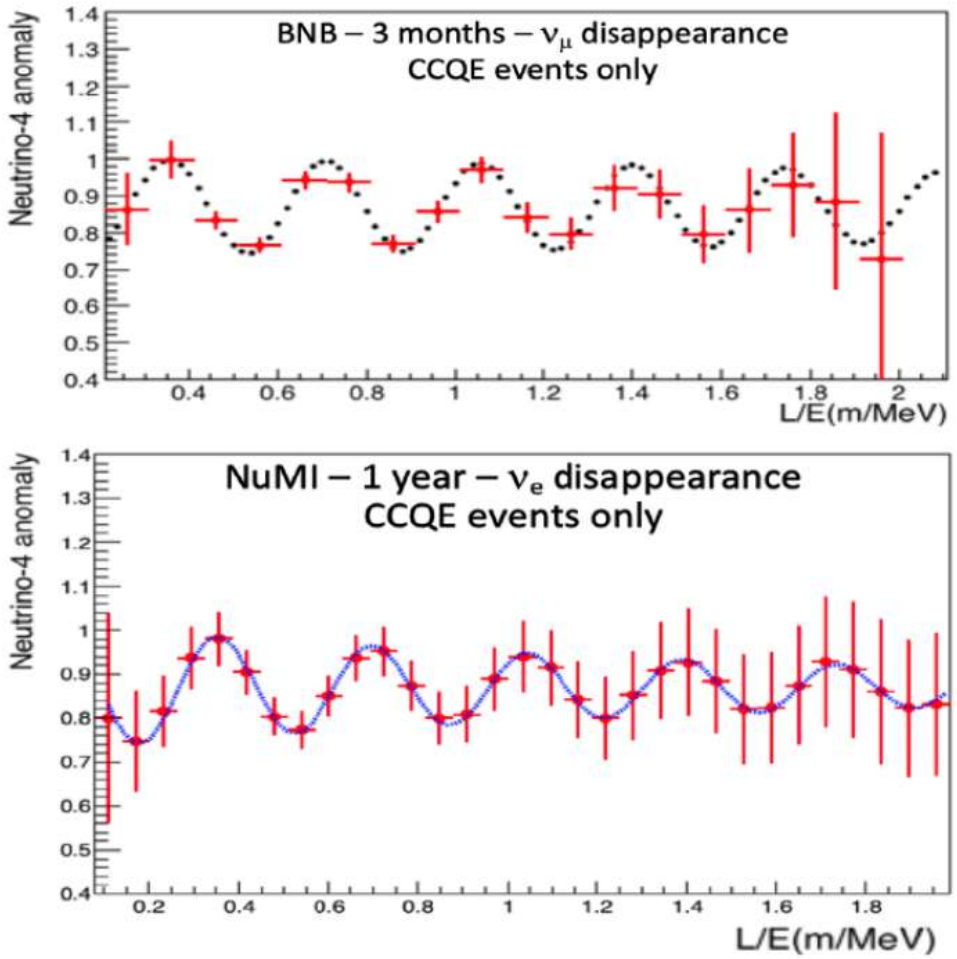

Figure 3.12: Expected survival oscillation probabilities at ICARUS, as a function of L/E, for ν_μ on the BNB (left, red dots) and for ν_e on the NuMI beam (right, red dots). This is superposed to the calculated survival ν_μ (left, black dots) and ν_e (right, blue dots) oscillation probability for Neutrino-4 anomaly, for the best fit parameters.

Chapter 4

Calibration of the ICARUS Cosmic Ray Tagger

4.1 The ICARUS Cosmic Ray Tagger

The CRT system serves as an external subdetector located outside the cryostats, with the primary goal of identifing charged particles that pass through or close to the active volume of the TPC. The time resolution of few nanoseconds of PMT and CRT together, with a precise synchronization of both the detector subsystems, allows to determine the direction of detected particles. Therefore the discrimination between particles coming from outside the detector from those produced by a neutrino interaction inside the LAr volume, allows to reject cosmic ray induced triggers. The CRT system covers an area of ≈ 1100 m^2 and is divided into three distinct subsystems: the *Top CRT*, *Side CRT*, and *Bottom CRT*. These subsystems complement each other, ensuring complete coverage (4π) of the active LAr volume and enabling the identification of nearly 95% of passing through cosmics with a spatial resolution of few cm [72]. In Figure 4.1 is shown a representation of the Top and Side CRT sub-systems in the plane perpendicular to the beam direction.

4.1.1 The Side and Bottom CRT

The ICARUS Side CRT is made of scintillator modules previously used by the MINOS experiment. Each module contains twenty 800 cm (L) $\times$ 4 cm (W) $\times$ 1 cm (H) polystyrene scintillator strips contained in a metal box, with a WLS fiber embedded along the center of each strip. The fibers from each module are gathered and connected to an optical readout system consisting of ten Hamamatsu SiPMs, with each SiPM reading out two fibers and linked

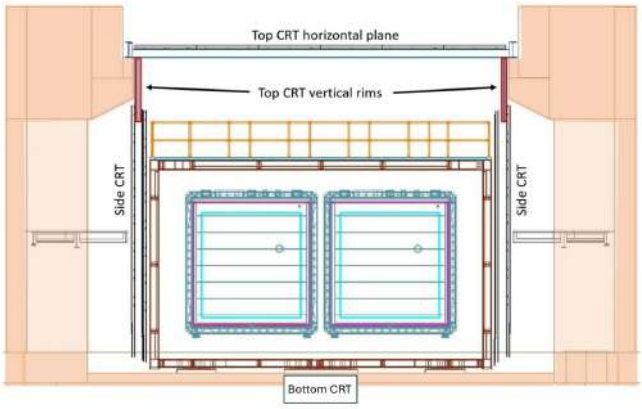

Figure 4.1: Representation of the Top, Side and Bottom CRT sub-systems.

Figure 4.2: Pictures of the (Left) Top CRT before the overburden deployment on top, (Center) Side CRT, and (Right) Bottom CRT on the ground pit of the ICARUS cryostat.

to a single CAEN FEB electronic readout channel. The system configuration uses two layers of modules, an inner and an outer layer, with coincidence logic applied to them. The south Side CRT wall (BNB beam's upstream direction) employs an X-Y orthogonal arrangement of the scintillator bars between the layers. On the east, west and north sides the CRT panels are installed in two parallel layers.

The Bottom CRT consists of 14 modules, previously used in the Double Chooz experiment, and positioned beneath the TPC warm vessel. Each module features 64 polystyrene scintillator strips organized in two layers. Scintillation light from these strips is collected by WLS optical fibers, read out at one end by a Hamamatsu multi-anode PMT, and mirrored at the other end [68, 74]. A picture of the three installed subsystem is shown in Figure 4.2 [54, 74].

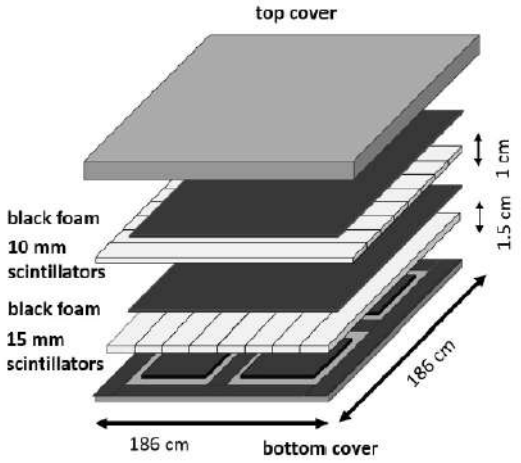

Figure 4.3: Sketch of a Top CRT module.

4.1.2 The Top CRT

The Top CRT is designed to detect around 80% of the cosmic muons that enter the ICARUS LArTPC. It consists of 123 modules, with 84 modules placed on the top horizontal plane and 39 modules covering the upper perimeter of the TPC (vertical rims). These modules function as hodoscopes and are composed of two perpendicular layers, each containing 8 scintillator bars, which are 23 cm wide. These scintillator bars are enclosed in aluminum boxes measuring 1.86 meters $\times$ 1.86 meters, as shown in Figure 4.3. In the top layer the scintillator bars are 10 mm thick, while in the bottom layer they are 15 mm thick. Each scintillator strip in the Top CRT has two WLS fibers embedded along the length of the bar, positioned 6 cm from each side, as shown in Figure 4.4. The CRT scintillators use Kuraray Y-11(200) WLS fibers [75]. These fibers are read-out from only one end, with the opposite end mirrored to enhance the light yield, and have an absorption peak at 430 nm, emitting green light at 476 nm with an attenuation length greater than 3.5 m [76]. Hamamatsu S13360-1350CS SiPMs are coupled to the WLS fiber as illustrated in Figure 4.5 to detect scintillation light. They have a crosstalk probability of approximately 3% and a photon detection efficiency of around 40% at 450 nm [77].

The SiPMs in each module are read out and biased by a CAEN DT5702 Front End Board (FEB) [78], shown in Figure 4.6, of the same type of those used for the Side CRT. The analog input signal is processed by the Cherenkov Imaging Telescope Integrated Read Out Chip (CITIROC), a 32 channel fully

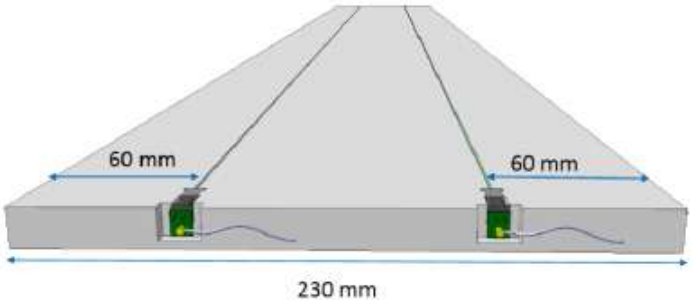

Figure 4.4: Representation of the scintillator bar with the two fibers embedded along the longitudinal direction of the bar.

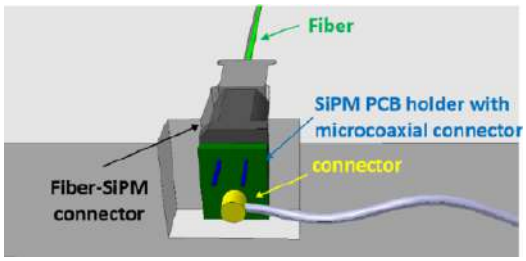

Figure 4.5: Picture of the SiPM connection scheme to the fiber.

analog front-end ASIC dedicated to read-out of SiPMs [79]. These 32 signals are directed to an XILINX Spartan-6 FPGA chip, which handles basic input coincidence and triggering logic. A coincidence between adjacent fibers of the same bar with a signal greater than 2.5 p.e. is required on each layer. The hardware trigger is performed requesting a coincidence between the two module layers. When a trigger is issued all the 32 channels of the board are digitized and read out. The FEB enables precise timing ($\sim$ ns) of cosmic-tagged particles (CRT hits) using an two independent internal counters T0 and T1. The first counter is reset every second by a Pulse-Per-Second (PPS) signal which provide an absolute time reference, while T1 counter receives a reset from the ICARUS Global trigger which is used for the synchronization of the PMT and CRT signal [74]. Reset signals are distributed to the Top CRT FEBs using LEMO connectors. Communication between the board and the host computer is done through the Ethernet protocol.

Together with timing information, the primary function of the CRT modules is to accurately determine the precise position of crossing muons. In the case of the Top CRT modules, they employ an XY scintillator layer configuration, enabling the creation of 64 coincidences of crossing strips (referred

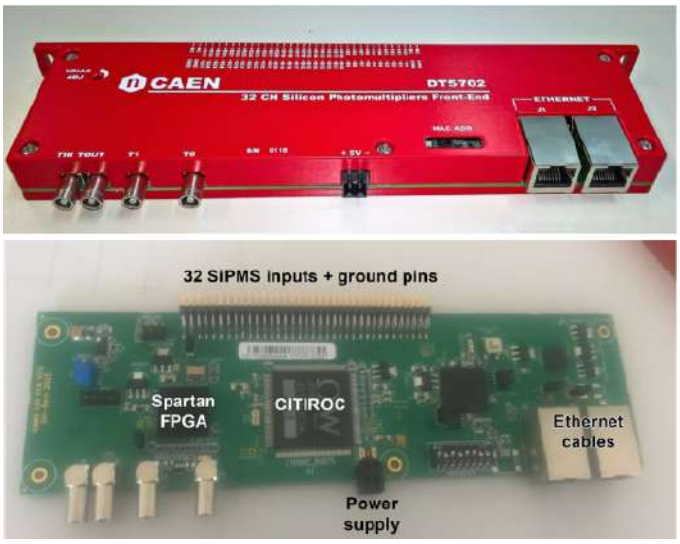

Figure 4.6: The Front End Board and its internal components.

to as "sectors") within each module. An example of a possible coincidence sector when a cosmic muon passes through, is illustrated in Figure 4.7 [80].

4.1.3 The ICARUS overburden

The Overburden (OB) placed on top of the ICARUS CRT consists of three layers of concrete, each 1 meter thick, or 6 m water equivalent. The concrete blocks are positioned 10 centimeters above the Top CRT horizontal modules.

By simulating with CORSIKA [81] the cosmic ray fluxes on ICARUS and evaluating the flux reduction through the ICARUS TPC, the OB reduces the dominant muon flux by $\sim 20\%$, stopping the muons with a $E_K \leq 1.5$ GeV. The suppression is more effective for hadrons, with a reduction by a factor ~ 200 for neutrons and ~ 500 for the protons. Primary γ's are almost fully suppressed. The results of the simulation show that the overburden reduces the most serious background due to γ initiated showers with kinetic energy ≥ 200 MeV [72].

The event rates before and after the installation of the concrete overburden are shown in Figure 4.8 for horizontal modules [54]. Before the OB installation, the nominal mean rate for horizontal Top CRT modules was approximately 620 Hz, while for vertically installed modules was around 250 Hz. The cosmic ray spectrum at sea level has two components: a soft component (about 30%) and a hard component (about 70%), the latter mostly consisting of muons with an average energy of 4 GeV and a typical rate of $\sim$ 100 Hz/m^2 ($\sim$ 70 Hz/m^2 for straight-going muons) [82]. Given the surface

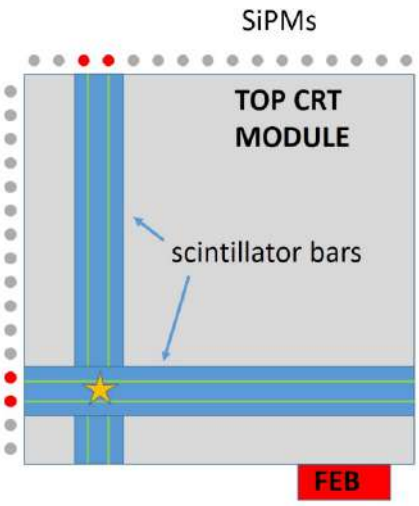

Figure 4.7: A possible coincidence sector at the passage of a cosmic muon.

area of the Top CRT modules (approximately 3.4 m^2), the expected rate for cosmic muons was around 340 Hz. The difference between the expected and the measured value is due to additional contributions from the soft component, including electrons, positrons, and gammas. After the overburden was installed, the mean rate per module decreased to approximately 330 Hz for the horizontal modules and 180 Hz for the vertical ones, mainly reflecting the expected rates from muons after the soft electromagnetic component was absorbed by the concrete. These values align with the expected muon-only component of the cosmic spectrum [82]. The overall cosmic rate across the entire Top CRT surface, following the complete overburden installation, is 35 kHz.

4.1.4 Calibration of Top CRT

4.1.5 Scintillators and Wavelength Shifting fibres

Scintillators are luminescent materials that emit visible light when excited by ionizing radiation. These materials have generally a linear response to the energy deposited, i.e. the intensity of the emitted light is proportional to the amount of energy absorbed. When coupled with an electronic light sensor such as a PMT, photodiode, or SiPM, these materials form what is known as a scintillation detector or scintillation counter. A light guide is generally needed to capture and channel the light emitted by the scintillator to the photodetector. This setup allows the photodetector to convert the

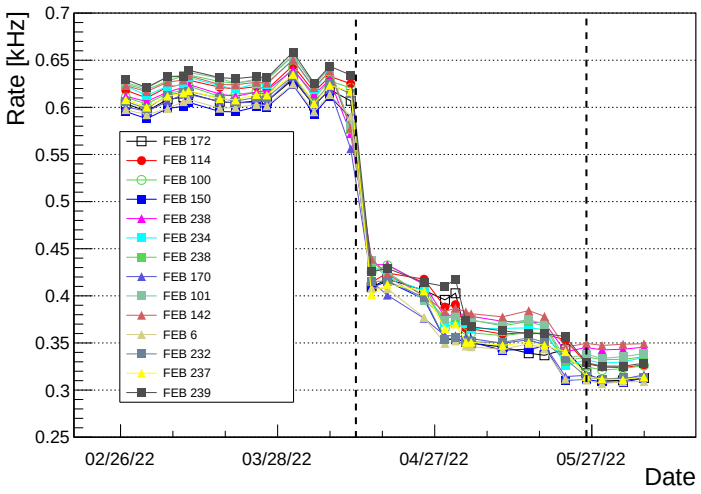

Figure 4.8: Cosmic ray rates as a function of time for a set of Top CRT horizontal modules. Numbers in the legend indicate the module's Front End Board and the black dotted lines indicate the beginning and the end of 3 m overburden installation over the displayed modules.

light into an electrical signal. In the ICARUS CRT, Wavelength Shifting (WLS) optical fibers are used in each scintillator strip to collect and guide the light to the surface of a photosensor. These fibers contain a fluorescent organic molecule (dopant) that absorbs short-wavelength photons and emits them isotropically at a longer wavelength. The WLS fiber is composed of a core and a cladding with different refractive index, and only about 4% of the light is trapped inside the fiber. An illustration of this absorption and reemission process is depicted in Figure 4.9.

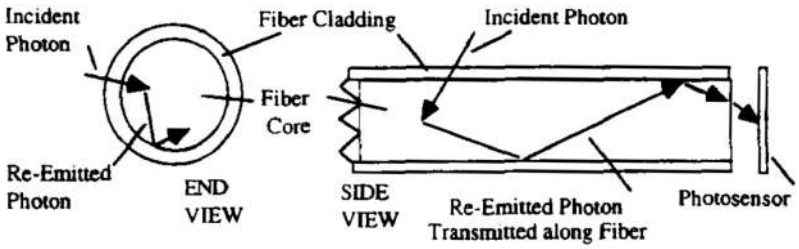

Figure 4.9: Illustration of photon absorption and reemission within a WLS fibre.

4.1.6 Silicon Photo-Multipliers

SiPMs are devices built from an array of single-photon avalanche photodiodes (SPADs, or micro-cells, also called *pixels*), on a common silicon substrate. SPADs are biased above the breakdown voltage V_{br}, working in Geiger-Muller avalanche mode. Each SPAD is in series with a quenching resistance and readout in parallel via a common substrate. An illustration of a SPAD, and the electric circuit of an array of microcells is shown in Figure 4.10 [76]. When a photon hits the photodetector, it generates an electron-hole pair through the photoelectric effect. The resulting carriers are then separated and drifted by an electric field, initiating a discharge if the field in the depletion region is high enough to cause secondary ionization along their path, achieving a typical gain G $\sim 10^6$. Photons are detected independently by each pixel, and their collective discharge currents form a quasi-analog signal that is proportional to the number of photons detected, providing information on the magnitude of an incoming photon flux. The output from each detected photon is a quantized pulse. This can be integrated by an ADC to visualize distinct peaks, representing different numbers of detected photons in a spectrum. In Figure 4.11 is shown a charge spectrum of a SiPM coupled to a scintillator for a Top CRT channel where different peaks, corresponding to a different number of detected photoelectrons, are clearly visible [76].

The SiPM Photon Detection Efficiency (PDE) is limited by the following contributions:

- the quantum efficiency, which is the probability of a photon to generate an electron-hole pair in the active region of the detector;
- the fill factor F or geometric efficiency, i.e. the ratio of sensitive to total area of a pixel, which depends on the gaps between the microcells;
- the probability for a photo-electron to initiate a Geiger discharge;
- the recovery time of the pixel, defined as the microcell reset period, in which the pixel capacitance C recharges back to V_{bias} through the quenching resistance and the microcell is ready for the detection of a new photon.

The gain G of a microcell is the ratio of the output charge to the charge q of an electron. The output charge can be calculated from the over-voltage $\Delta V_{ov} = V_{bias} - V_{br}$ and the microcell capacitance C as:

$$G = \frac{C\Delta V_{ov}}{q}. \tag{4.1}$$

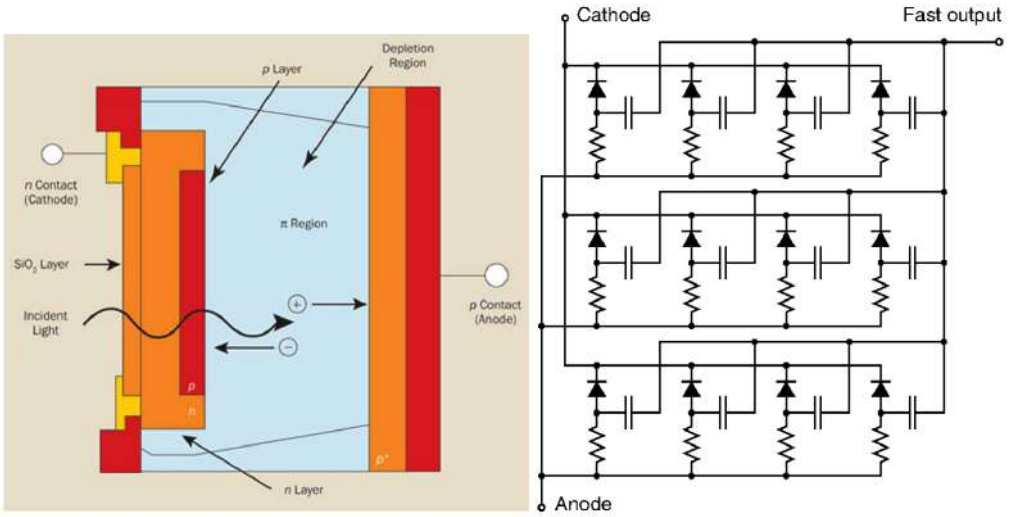

Figure 4.10: (Left) Cross section of an avalanche photodiode. (Right) Simplified schematic of a SiPM array of microcells.

The signal of a fired pixel is linearly proportional to the capacitance of the microcell and to ΔV_{ov}. SiPMs typically operate at an over-voltage from 1 to 5 V over V_{br}.

SiPMs present different sources of noise, that together influence the signal interpretation:

- *Dark current*, resulting from thermally generated electrons that can initiate avalanches. This effect increases with the temperature.
- *Optical cross-talk*, where photons from a breakdown avalanche in one cell can induce avalanches in neighboring cells. This can lead to signals equivalent to multi photon events, for a single detected photon.
- *After-pulses*, caused by delayed release of carriers trapped during a discharge, resulting in a subsequent avalanche and producing a delayed secondary pulse.

4.2 Calibration of the Top CRT

As part of this thesis work and during a two months internship at Fermilab, I took care of the calibration of Top CRT. The primary objective of the calibration analysis is to estimate the pedestal and gain values of each Top

CRT channel, in order to monitor and equalize the detector response over time. The analysis code, based on the ROOT [83] analysis tool was integrated in the experiment software framework `icaruscode` (version: v09_77_00).

The pedestal and gain values can be obtained by fitting the integrated ADC charge spectrum of each channel, exploiting the feature that at each trigger the FEB stores the ADC value of each of the 32 channels. The first step of the analysis (decoding stage) is to convert the raw data into a readable format where the most relevant information are stored in a ROOT Tree:

- the Front End Board MAC5 address (whose variable name is `fMac5`), as mapped in Figure 4.12;
- the ADC values of all 32 FEB channels (`fAdc[32]`);
- the flag (`fFlags`), that represents the CRT `Hit`status.

The flag variable is an integer and can take the values: 3 if the event is related to a CRT signal hit from a crossing particle that triggered the acquisition, 7 or 9 if due to the reset of T0 and T1 counters. After the decoding stage, the data entries are used to construct integrated ADC spectra for all the channels. For each module trigger, the ADC values of each channel are recorded by the data acquisition system, and this information is extracted to generate histograms of charge spectrum distribution for each of the 32 channels within the 123 modules/FEBs of the Top CRT. An example of spectrum is showed in Figure 4.13. Additionally, the calibration analysis creates histograms for channel electronic noise with ADC values corresponding to 0 p.e. (pedestal distributions), signal photoelectron peaks (signal distributions), and the cumulative ADC counts across all channels per module/FEB, as shown in Figure 4.14.

To generate the channels signal distributions I selected the data entries, from the calibration Run 9989, with `fFlags = 3` fFlags (the module recorded signal generated by a cosmic particle) excluding all entries with ADC < 250 and took the highest 2 ADC counts in each layer of scintillator bars. These values were used to fill the histograms of the corresponding channels. As already mentioned, a CRT triggering coincidence between two scintillator bars in the same module is obtained when at least 4 channels signals are above a certain threshold.

Accordingly, the pedestal distributions were initially derived by selecting the hits ADC values recorded in the channels of each layer with `fFlags = 3`, with the exclusion of the top 6 highest values per layer. In this way I obtained the ADC spectrum of a channel when it was not participating in the CRT triggering coincidence (also referred to as non-triggering channel

logic), estimating its noise distribution. The large pedestal fluctuations may be related to some unexpected behaviour of the electronics which affects channels below threshold when the front-end is (auto)triggered by 4 or more channels. Therefore it was not suitable to correctly estimate the waveform baseline for the pedestal. A different selection was then explored to obtain the pedestal distribution. Using the same dataset, I exploited the T1 and T0 special reset events which behave as external random triggers and force the readout of all the 32 channels. Those signals are generated by an external uncorrelated source (PPS signal or ICARUS global trigger), so that the ADC value of all 32 channels are most likely electronic noise and a new sub-sample with a reduced statistic was obtained (see Figure 4.15).

A further problem was observed when digitizing the special reset events of the T0/T1 counters: not all reset events were correctly identified and flagged as special events, but they were flagged as regular signal hits (65% of the times the flag is correct [72]). In order to identify T10 reset hits and disentangle with the normal triggers, a possible solution can be obtained by considering the sum if all 32-ADC values of the Board. As seen in Figure 4.16, we can see that the sum of the signal given by reset hits (red peak on the left) is superposed on a similar peak related to the sum of the ADC values of signal hits (in blue). In the future a cut for signal sum values below 7000 ADC will be exploited for a better selection of reset hits. However, the distribution of pedestal obtained using the hits triggered by the T1/T0 reset signals is still quite large (NUMBER), even if better than the one obtained with normal triggers which require at least other 4 channels above threshold. In an attempt to obtain a "clean" pedestal further investigation is required.

The obtained charge distributions were then analysed. With the developed algorithm, multiple gaussian fits are performed on the pedestals distribution, as obtained by triggering with reset signals, optimizing the fit range until the reduced χ^2 is smaller than 10 or until there are no more bins in the selected range (see Figure 4.17). The mean value extracted from the fit is then stored for the channel's gain evaluation. For the signal a similar procedure is followed: the ROOT function `TSpectrum` is used to search for the first 5 peaks in the signal distribution, quantized photoelectron peaks are fitted recursively using a gaussian distribution, adjusting the fitted range of the histogram in order to minimize the reduced χ^2. For each fit, the minimum distance between the previous and following peaks is used as the range and is recursively reduced until $\chi^2 < 2$ or until there are no more bins in the selected range. In Figure 4.18 a distribution of the charge spectrum for a bottom layer channel is shown, with overlayed the recursive gaussian fit of the first 5 photoelectron peaks. The mean and standard deviation values of the fit for each peak are then stored.

In order to extract the gain the mean ADC values of the pedestal and the fitted photoelectron peaks are plotted as a function of the corresponding photoelectron number. The gain for a specific channel is determined as the slope of a linear fit. Following the calibration of pedestal and gains for all the Top CRT channels, the conversion of ADC counts to photo-electrons can be obtained by:

$$n_{p.e.} = \frac{ADC_i - Ped_i}{G_i} \tag{4.2}$$

where $n_{p.e.}$ is the resulting number of photo-electrons, ADC_i is the ADC value of the i-th channel and Ped_i and G_i are, respectively, its pedestal and its gain as evaluated from the calibration. The result of this work is presented in Figure 4.19, where an example of gain fit for a top layer's channel is shown. The colored band represents the growing sigma value of the fitted photo-electron peaks and the y-intercept is the ADC count mean value of the pedestal peak.

After determining the gain and pedestal values for each channel, the average amount of light ("light yield") produced by the particles when they pass through scintillator bars can be calculated. By converting the ADC values of the charge spectra of each channel into p.e., the most probable value of the distribution can be evaluated by fitting it with a Landau function convoluted with a Gaussian, thus obtaining the average light yield for each scintillator bar. The Landau distribution describes the typical energy loss of charged particle in scintillator materials while the Gaussian function describes statistical fluctuations introduced by the photosensor and other contributions like the non-uniformity in the light collection process and the non-linear scintillator response.

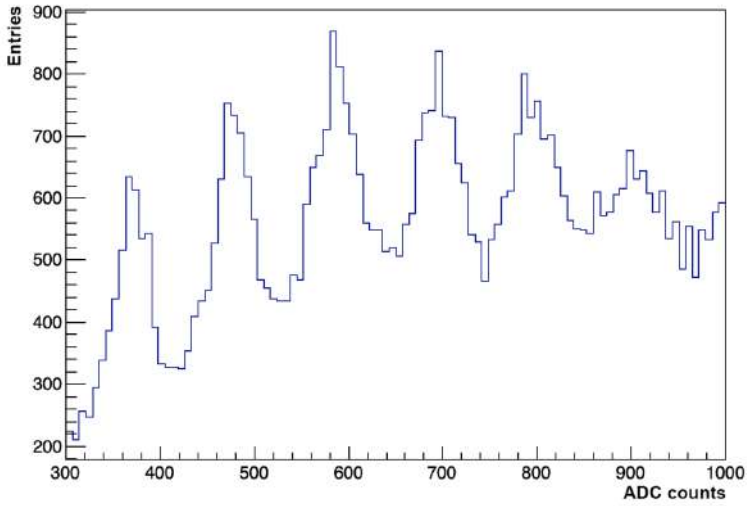

Figure 4.11: The photo-electrons spectrum of a SiPM used in one bar of the CRT scintillators.

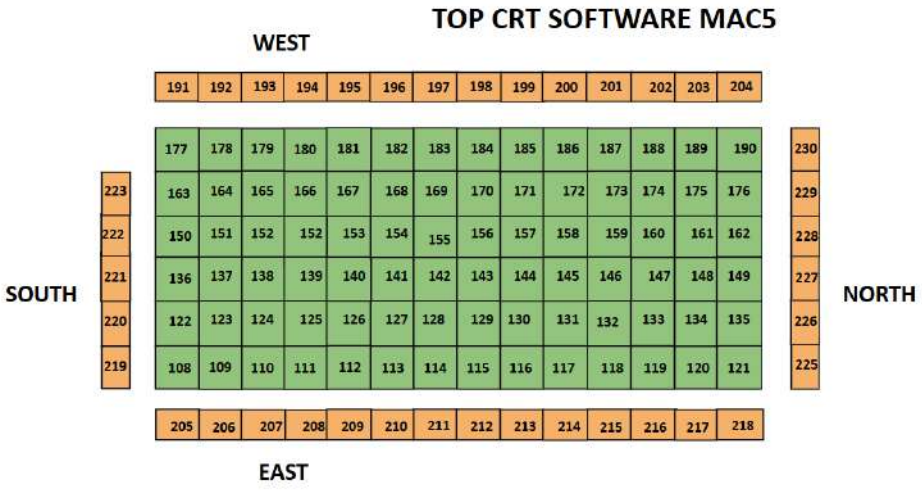

Figure 4.12: Map of the MAC5 addresses of the FEBs/modules of the Top CRT. Modules colored in green are installed horizontally, while the orange modules are positioned vertically.

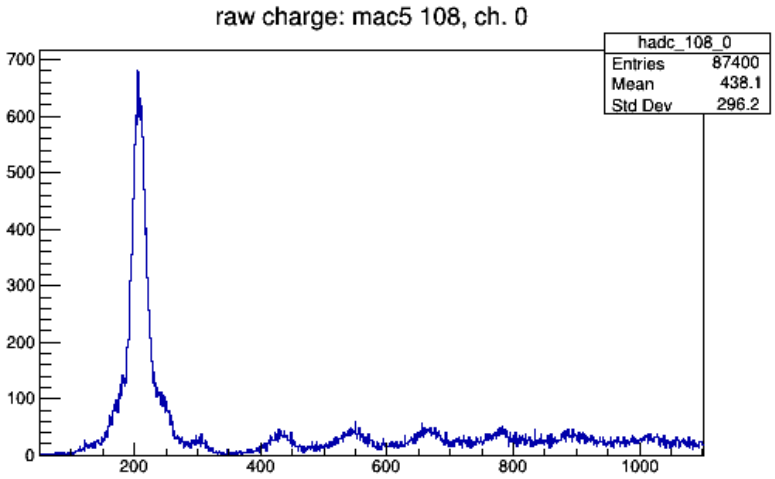

Figure 4.13: Example of spectrum for a 15 mm scintillator channel (Top Layer) zoomed in the range 0 - 1100 ADC Counts. The pedestal and signal peaks are visible.

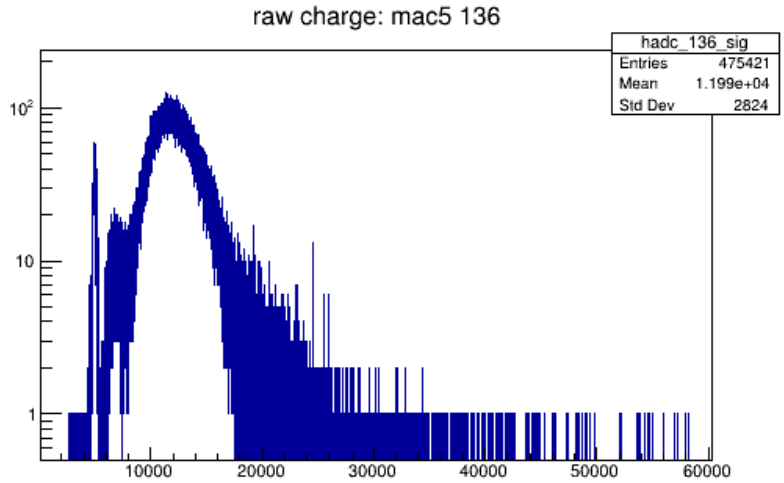

Figure 4.14: Histogram obtained by the sum of the ADC count values of all the 32 channels of the FEB with MAC5 address 136.

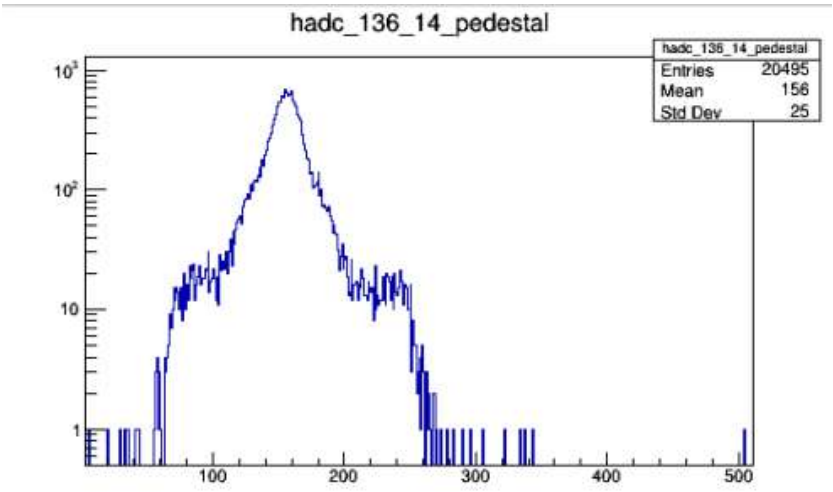

Figure 4.15: Pedestal distribution for a Top Layer channel obtained from the reset hits, with a lower statistic and with the y-axis in log scale.

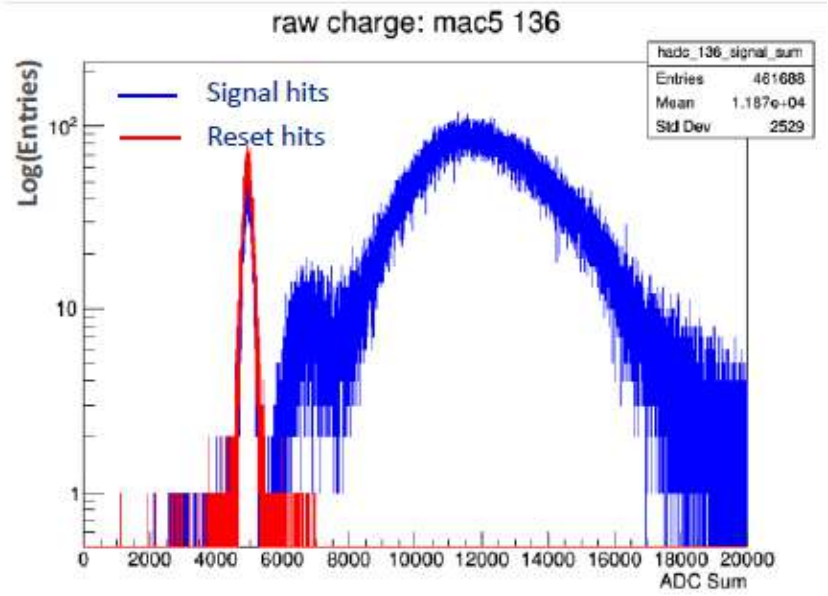

Figure 4.16: Superposition of the distributions of adc values sum on all 32 channels of a FEB for pedestal obtained with reset hits correctly flagged (red) and signal hits (blue).

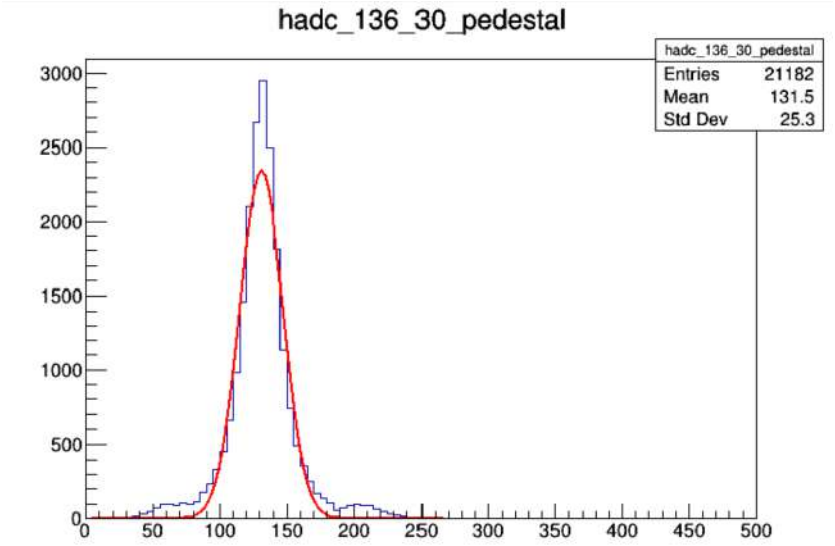

Figure 4.17: Pedestal distribution for a Bottom Layer channel obtained from the reset hits (blue) and fitted with a Gaussian distribution (red) with $\chi^2 < 10$.

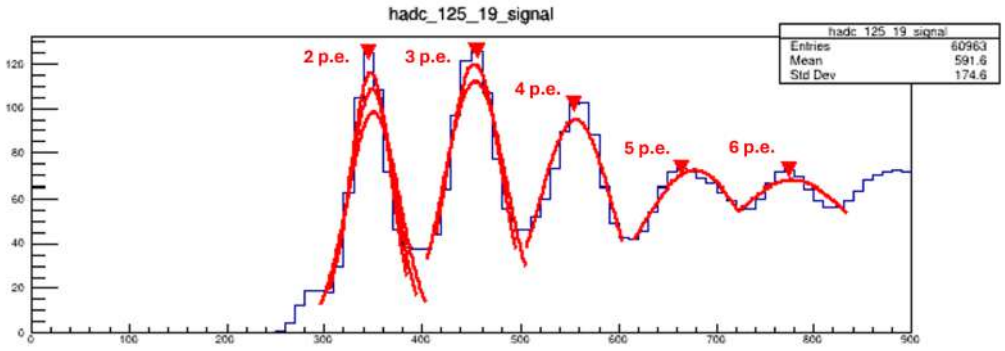

Figure 4.18: Recursive single photoelectron peaks fitting with a gaussian distribution for a bottom layer's channel when participating in the CRT triggering coincidence. The signal has a cut for ADC counts >250 and the left peak corresponds to 2 p.e.

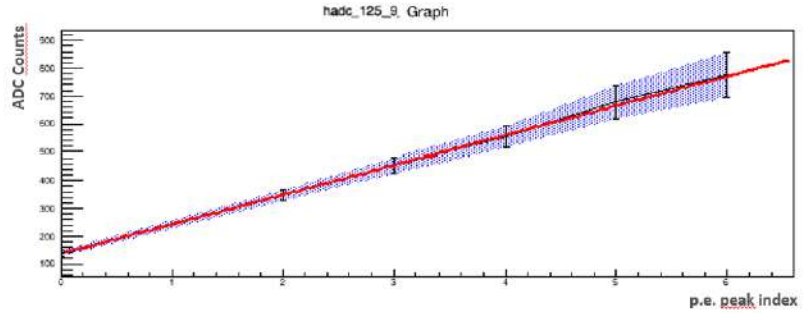

Figure 4.19: Distribution of the p.e. peaks mean value versus the corresponding p.e. number with the superposed linear fit (in red) used to evaluate the gain from the slope. The peak with index 1 is skipped. The blue band shows how the standard deviation of the fitted gaussians grows with the peak number.

Chapter 5

Event reconstruction in the ICARUS TPC

The ICARUS detector is designed to identify and analyze both neutrinos and cosmic rays interactions, using the data collected from the TPC, the PMT and the CRT subsystems. The TPC is crucial for reconstructing events, exploiting the topological and calorimetric information to create tridimensional track and shower objects, identifying and characterizing the particles involved. In this process the PMT system uses scintillation light to trigger data acquisition, assigning a time for the event with a nanosecond precision and localizing the interaction inside the detector. Meanwhile the CRT data is used to identify and reject cosmic rays in coincidence with the neutrino beam spill.

This chapter will primary focus on the event reconstruction process within the TPC. Hardware related issues and inefficiencies at reconstruction level can compromise the accuracy of the event reconstruction, leading to single particle trajectories being erroneously segmented into multiple tracks. This problem is here analyzed for Monte Carlo simulated data, and a solution is proposed with the aim of improving track reconstruction and momentum estimation.

5.1 The data processing chain

The design and acquisition parameters of ICARUS result in a high data rate and volume. The majority of this data (about 90% of the total event size) is coming from the four TPCs: the signals from the TPC wires are digitized with a 12-bit ADC, with 2 bytes per sample at a sampling frequency of 2.5 MHz. The TPC data acquisition time window of $\sim$1.6 ms corresponds to 4096

samples and allow to record activity before and after the beam spill. With ∼53000 wires this means for the TPC raw data only, about 400 MB/event. Each ICARUS event size is then reduced to about 200 MB by software lossless data compression. The output data from the detector includes digitized waveforms from each TPC readout channel and from the PMTs. These respectively represent the signal induced by the ionization charges collected by the wires and the signals from detected scintillation photons. All collected raw data must go through many levels of software processing before it can be analyzed. The signal processing and events reconstruction is done in two stages. In the "`Stage0`" the raw data is translated to LArSoft [84] format for offline processing. LArSoft is a toolkit for the simulation, reconstruction, and analysis of events in LArTPCs. Its data format is a typical output format common across different LArTPC experiments, which might have slightly differing detector geometries and readout schemes but share the same underlying physics in liquid argon. The first stage includes [68]:

- Decoding: the raw data is decompressed and converted to the format used in the next steps. In this step the electronic noise is filtered, to remove TPC coherent noise.
- Deconvolution: this process removes the effect of the electrostatic field around the wires and on their electronic response.
- ROI (Regions Of Interest) finding: the volume of data is reduced by identifying ROIs around candidate signals, isolating the charged particle signal used in the next processing steps.
- Hit finding: builds the `Hit` objects from the ROIs identified in the previous step. The `Hit`s are the primary input to the remaining pattern recognition phase.

This processed data, about 10 times smaller than the initial raw input data volume, becomes the input for the next stage. `Stage1`, focuses on the reconstruction of the signals coming from the different subsystems, and includes:

- Hit filter: combine 2D Hits across different wire planes to build three dimensional space points.
- Pattern Recognition: multiple algorithms attempt to organize nearby hits into clusters. These are used to identify track or shower candidates, cosmic rays and obtain event topology information. Interactions, also called "slices", are classified in neutrino candidate interactions or cosmic ray muon interactions and a hierarchy of all the reconstructed objects is defined to determine parent-daughter relationships.

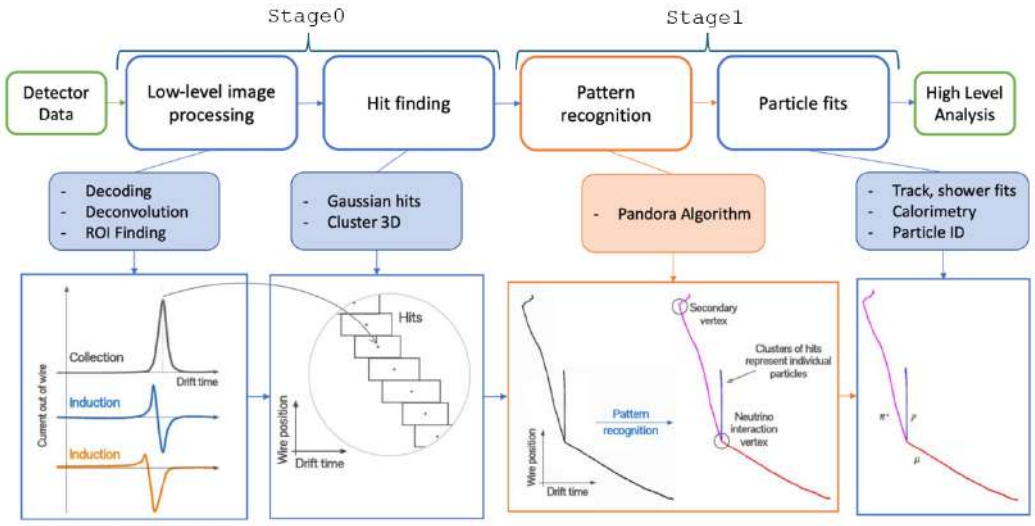

Figure 5.1: Illustration of the ICARUS TPC signals processing and reconstruction process.

- Particle fits: algorithms are applied to reconstruct tracks and showers, and to provide calorimetric measurements for each identified particle. This also includes information for kinematic reconstruction and event analysis.

A schematic representation of the TPC signals processing and reconstruction chain is shown in Figure 5.1. At the end of `Stage1` processing, events are fully reconstructed and stored in TTrees (a columnar dataset) [85] in ROOT files, which are then used as input for further analysis. These files can be of two types, `Calibration Ntuples` or `CAF` (Common Analysis Framework) files, and depending on the type of analysis we want to perform we can use one or the other. The `Calibration Ntuples` are generated automatically after `Stage1`, and are regular ROOT files primarly intended for calibration studies. `CAF` files are ROOT files created after `Stage1` and containing all the essential information for high-level analysis, while omitting heavy data products such as raw digits, wire responses, and full hit information. These lighter files are fast to process and, differently from the `Calibration Ntuples`, preserve the hierarchical structure inherited from the reconstruction process. The contained TTree consists of a series of branches, a list of independent columns containing C++ type data, where each entry in a branch corresponds to a single detector readout. `CAF` files enable analyzers to share event selection and reconstruction techniques, with the goal of a rapid analysis developement.

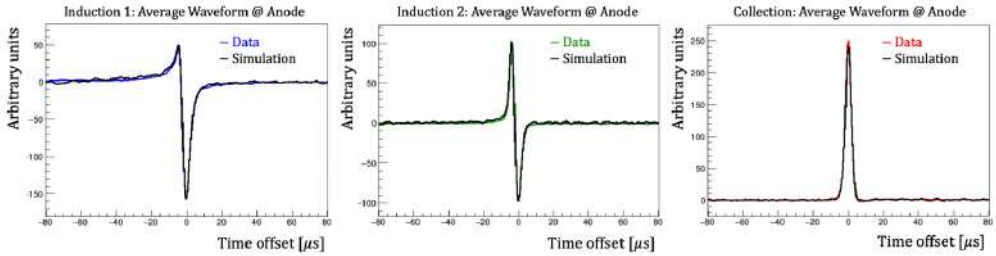

Figure 5.2: Averaged signal waveforms from measured data and simulated response for one TPC, showing the characteristic unipolar and bipolar shapes for the three planes.

5.2 TPC Reconstruction

The reconstruction process starts with the detection of ionization electrons on the anode planes. Each of the three anode wire planes records waveform signals with a sampling time of 0.4 μs (tick). The three wire planes are biased at -250V, 30V and 250V for Induction 1, Induction 2 and Collection planes respectively. This biasing ensures full transparency of electrons to the first two planes, allowing all the charges to be collected by the last plane. As charges approach the wires of the first two planes, they produce a positive signal that becomes negative once a plane is crossed, resulting in a bipolar signal. On the other hand, electrons generate a unipolar positive signal on the collection plane, as shown in Figure 5.2 [68].

5.2.1 Wires signal processing

The signal recorded on the wires is not due exclusively to the ionization charge, but several effects interfere between the ionization and the measurement in the wire signal. The measured waveform is a convolution of the signal formation itself, electron propagation through the liquid argon, electrostatic field around the wires, signal response of the readout chain and electronic noise. The sum of these effects has to be subtracted from the waveform to correctly extract information on the charge deposited on each wire as a function of time. Noise filters are applied to remove random electronic noise and coherent noise caused by other detector components. Then the deconvolution of wire signal waveform is performed, after which the signal pulse of the charge would be gaussian-like, with mean and integral values determined by the drift coordinate and ionization charge deposited respectively. The area under the deconvoluted waveform would then be proportional to the number

of deposited electrons. By assuming that the induced current on each wire is independent from the nearby charge distribution, the "one-dimensional deconvolution can be applied. The measured signal $M(t')$ is modeled as a convolution integral of the original ionization charge signal $S(t)$ and the detector response funtion $R(t, t')$. This function describes the portion of the measured signal at time t' resulting from an element of the original signal at time t [86, 87]:

$$M(t') = \int_{-\infty}^{\infty} R(t' - t) \cdot S(t) dt. \tag{5.1}$$

By applying a Fourier transform, we convert the previous expression in the frequency domain equation $M(w) = R(w)(w)$. However, this straightforward approach can cause an amplification of high-frequency noise during the deconvolution process. To address this, a low-pass filter function $F(w)$ is introduced:

$$S(w) = \frac{M(w)}{R(w) \cdot F(w)}. \tag{5.2}$$

replacing a response function with an effective one, and mitigating high-frequency noise. The original signal can then be obtained by applying the inverse Fourier transform to $S(w)$. Currently ICARUS uses the described 1D deconvolution, but is transitioning to a 2D deconvolution, in which both time and wire direction are considered to account for contributions from ionization charge in nearby wire regions, potentially causing interference, especially in induction planes and for isochronous tracks (tracks travelling almost parallel to the wire planes). An example of TPC signal processing in MicroBooNE, employing the same deconvolution technique at different stages is shown in Figure 5.3 [68].

5.2.2 ROI finding

After the deconvolution, the bipolar signal on the induction planes is converted into a unipolar signal similar to that of the collection plane. This difference causes a worse perfomance of the deconvolution for the induction planes with respect to the collection plane due to the wire response suppression at low-frequency signals.

The measured signal contains eletronics noise which in the decovolution process is not necessarily as suppressed at low frequencies. This lead to an amplification of the low frequency noise that without mitigation, would lead to an uncertainty in the charge estimation.

To address this problem, only certain regions in the time domain, namely ROIs, are considered for the deconvolution. This involves limiting the deconvolution to small time windows around the signal waveform, and replacing

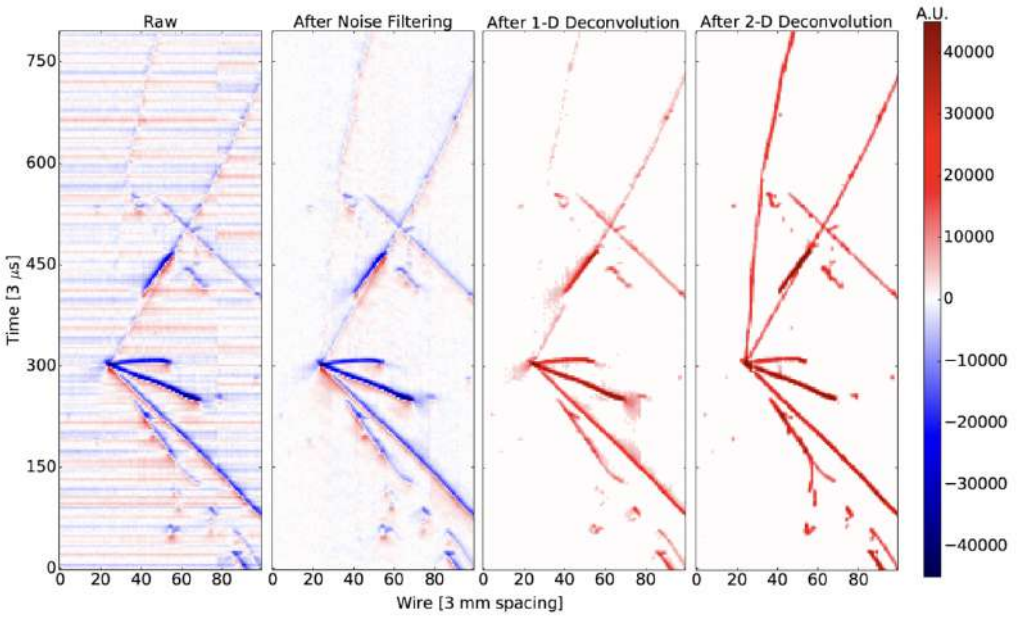

Figure 5.3: Event displays of the Induction 1 plane from a neutrino interaction candidate in MicroBooNE. From left to right: raw waveform (baseline-subtracted ADC), noise-filtered waveform, and charge spectrum (electrons) after 1D and 2D deconvolution. Bipolar signals (red/blue) are converted to unipolar after deconvolution.

the entire event readout window with a set of ROIs, as shown in Figure 5.4 [68]. The ROI finding is performed on all the planes and helps also in reducing data size and speeding up wire signal processing. Deconvolution filters are chosen to ensure the signal from an individual charge element is Gaussian-shaped, facilitating the following reconstruction steps.

5.2.3 Hit finding

A `Hit` is a two-dimensional object representing a cluster of electric charge detected at a specific wire and time. The Hit Finder module, called `gaushit`, assumes gaussian-shaped charge deposits. It processes input ROIs from the deconvoluted waveform, by first finding candidate pulses over a certain threshold and then fitting them to a Gaussian shape. If multiple charges are detected by the same wire in a short time period, the pulse is divided into multiple hits, described by overlapping Gaussian peaks. The properties of `HitsHit` are derived from the Gaussian fit parameters, where the area indicates the total charge (converted from ADC×t-sample to Coulombs) and the

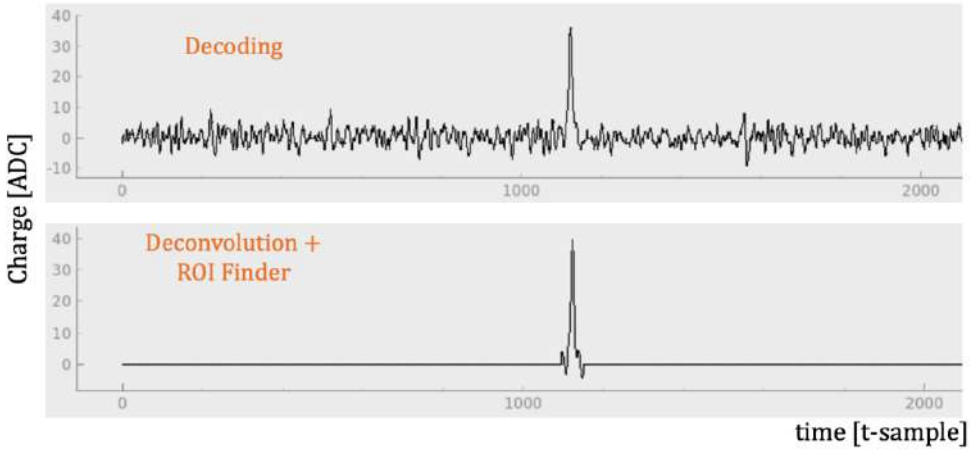

Figure 5.4: (Top) Measured waveform in the collection plane, after the decoding stage. (Bottom) Remaining signal waveform after the deconvolution and ROI finding stages. A t-sample corresponds to 0.4 μs (1 tick).

mean represents the hit peak time. A visual representation of the Hit Finder algorithm applied on a Collection plane waveform is shown in Figure 5.5 [68]. The output of this stage is a collection of 2D `Hits`for each wire plane, used as input to the pattern recognition algorithms.

5.3 Pandora Pattern Recognition

The Pandora software development kit [88] was developed to simplify the creation, implementation, and execution of pattern recognition algorithms

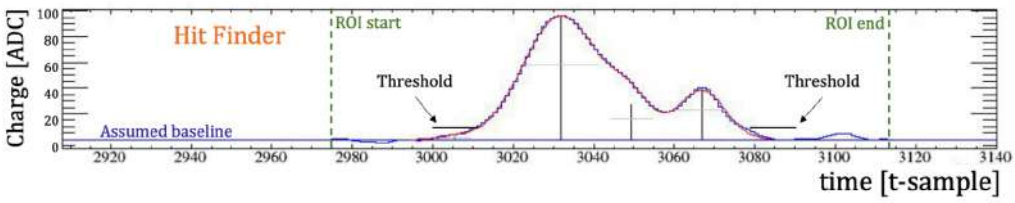

Figure 5.5: Illustration of the Hit Finder algorithm applied on a collection plane waveform. The red line represents the three Gaussian-shaped fits. The crosses indicate the centers of the fit peaks, the pulse heights above the baseline, and their fit widths. The ROI regions, assumed baseline, and threshold are also visible.

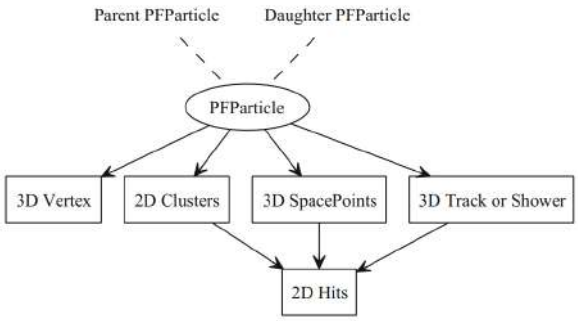

Figure 5.6: Illustration of the Pandora output data products.

for identifying energy deposits from particles in fine-granularity detectors. It uses a multi-algorithm approach, where each algorithm addresses specific tasks in a particular topology.

Pandora reconstruction (designed to be generic to allow its use by multiple experiments) is integrated into the LArSoft framework, and the current chain of algorithms is primarily tuned for neutrino interactions from BNB. The goal of Pandora is to reconstruct each particle as a single, pure (containing only hits from that particle), and complete (including all hits from that particle) object.

The pattern-recognition chain is applied to a list of reconstructed 2D hits, generated by the Hit finding process, and takes into account detector information (e.g detector geometry and dead wire regions). The main output, illustrated in Figure 5.6 [88], is a list of reconstructed *Particle Flow Particles (PFPs)*, each corresponding to a distinct track or shower in the event. The PFPs are associated with a set of 2D clusters, reconstructed 3D positions (SpacePoints), and a reconstructed vertex position (the interaction point or first energy deposit). A hierarchy identifies parent-daughter relationships between PFPs and describes the particle flow in the observed interactions. A neutrino PFP can be created as part of this hierarchy, serving as the primary parent particle for a neutrino interaction. Tracks typically represent muons, protons, or parts of charged pion trajectories, while showers represent electromagnetic cascades.

Pandora has two main chain algorithms for event reconstruction in neutrino detectors:

- PandoraCosmic, optimized for reconstructing cosmic ray muons andthe associated delta rays or showers. This reconstruction is more track-oriented, producing primary particles that represent cosmic-ray muons. The reconstructed vertex/start point for the cosmic-ray muon is the

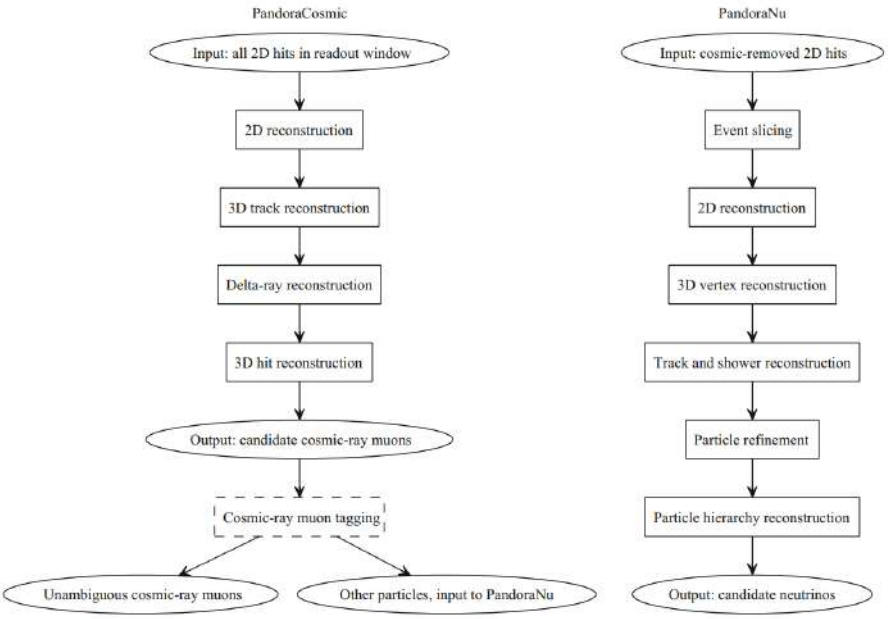

Figure 5.7: Flowchart of the Pandora reconstruction chain, with the two multi-algorithm reconstruction paths PandoraCosmic and PandoraNu. Particles formed by the PandoraCosmic reconstruction are examined by a cosmic-ray tagging module, external to Pandora.

high-y coordinate of the muon track.

- PandoraNu, optimized to reconstruct neutrino interactions. This reconstruction identifies a neutrino interaction vertex and then uses this to help in the reconstruction of all particles emerging from the vertex position. It carefully reconstructs tracks and showers, creating a parent neutrino particle and adding the visible particles as daughters of the neutrino.

ICARUS data is passed through the PandoraCosmic and PandoraNu reconstructions using a two-stage approach. The first stage is the processing of all hits in a pre-determined readout window to produce an initial list of candidate cosmic-ray particles. This list is then examined by a dedicated cosmic-ray tagging module, which looks for unambiguous cosmic-ray muons in terms of start and end positions and the location of their hits in time. Cosmic ray muon-associated hits are removed from the input hit collection, and the new collection is used as input for PandoraNu reconstruction, resulting in a list of candidate neutrino interactions. The overall chain of Pandora algorithms is illustrated in Figure 5.7 [88].

5.3.1 PandoraCosmic

The PandoraCosmic stage begins by performing a two-dimensional clustering of hits within each read-out plane of the detector. Hits are clustered based on their proximity and alignement to form continuous lines, indicating possible particle trajectories. If a bifurcation or ambiguity is detected separate clusters are created to mantain cluster purity. Then nearby or collinear clusters are merged to enhance cluster completeness.

In the three-dimensional track reconstruction phase, 2D clusters from different planes are combined to form 3D particle trajectories. The algorithm check all possible combinations of 2D clusters to find 3D tracks, using a χ^2 test to measure fit quality and resolve ambiguities. These emerge if a 3D cluster contains more than one 2D cluster from any single readout plane view.

Clusters not included in the main tracks are considered potential fragments from secondary processes, such as delta-rays and secondary particles. After creating 3D SpacePoints, a cosmic ray tagging filter is applied. PandoraCosmic places the start position of tracks tagged as "unambiguous cosmic ray muons" at their heighest reconstructed vertical coordinate, assuming that they move downward in the TPC. A parent-daughter relationship is assigned to the secondary track and shower reconstructed particles linked to the primary cosmic muon track. Finally all cosmic-ray muons hits are removed from the 2D hits collection used in the PandoraNu stage of the reconstruction.

Cosmic ray muon tagging and tracks stitching

As described in Section 2.4 the x coordinates, i.e. drift coordinate, of reconstructed objects inside the LArTPC are computed from the drift time of ionization charges. This drift time is the difference between the time at which ionization signals are recorded on the wires (t_m) and the time at which the particle interaction that generated the signal occurred (t_0):

$$x = v_d \cdot (t_m - t_0). \tag{5.3}$$

In this equation v_d is the electron drift velocity, and the value of t_0 can be obtained from beam timing or from a trigger provided by the light collection system [68]. As shown in this equation, knowing t_0 is crucial for accurately reconstructing the hits positions in space. Without a precise t_0 assignment the interaction point along the x-axis is ambiguous, since $t_m = t_0 + x/v_d s$ could correspond to multiple t_0 (the particle time is the reference time for computing the x coordinate) and x combinations. Solving the ambiguity becomes more challenging in environements with a high cosmic ray flux, to which the assignement of a unique t_0 is not straightforward. This is not

a problem for in-time interactions, where $t_0 = 0$ by definition, and whose x-position is correctly reconstructed. For out-of-time interactions t_0 is unknown, and Pandora's reconstruction algorithms assume $t_0 = 0$ by default. For these events, it is not possible to distinguish between a particle arrived before the trigger far from the anode plane, and one that arrived after the trigger but closer to the anode, as they both would have the same t_m.

The measurement of t_0 can be done with different techniques. One is the "PMT-TPC matching", that involves matching an optical flash (a cluster of optical hit signals on the PMTs) to a reconstructed object in the TPC, accurately assigning a track time. A light-independent technique, called "stitching", can be instead applied to cathode crossing tracks. Each drift volume is initially processed independently by Pandora reconstruction. For tracks with $t_0 = 0$ crossing the cathode this yields two separate reconstructed segments displaced symmetrically from the cathode, but shifted in opposite directions due to the differing drift field directions. This displacement is directly proportional to the actual track time t_0 and inversely to the drift velocity v_d. The direction of the displacement indicates whether the track arrived before (*early track*) or after (*late track*) the trigger time, a scan be seen in Figure 5.8 [68].

The Pandora algorithm uses the geometric features of these tracks to search for two 3D clusters reconstructed in adjacent drift volumes and consistent both in position and direction with a single continuous trajectory across the cathode boundary. If a match is found, the separate clusters are shifted to the x-coordinate of the cathode plane. The track t_0 can be estimated by:

$$t_0 = t_{max} - (L - \Delta x)/v_d, \tag{5.4}$$

where t_{max} is the time of the hit closest to the cathode, L is the maximum drift length (1.5 meters), Δx is the distance between the cathode and the x-position of the hit with t_{max} (see Figure 5.8) and $v_d \sim 1.6$ mm/μs at the nominal drift field of 500 V/cm.

For each triggering event a total of 4096 time samples are recorded by the wires, with about 850 collected before the trigger. Thus, to collect all the hits of an interaction, the first hit must be recorded no earlier than 340 μs before the trigger time, and the last one hit no later than 1300 μs after the trigger. After the stitching algorithm, cosmic ray candidates are identified if they meet any of these conditions:

- the particle crosses both the top and bottom of the detector (through-going particle);
- assuming $t_0 = 0$, any hit is outside the drift volume, as shown in the bottom right illustration in Figure 5.8;

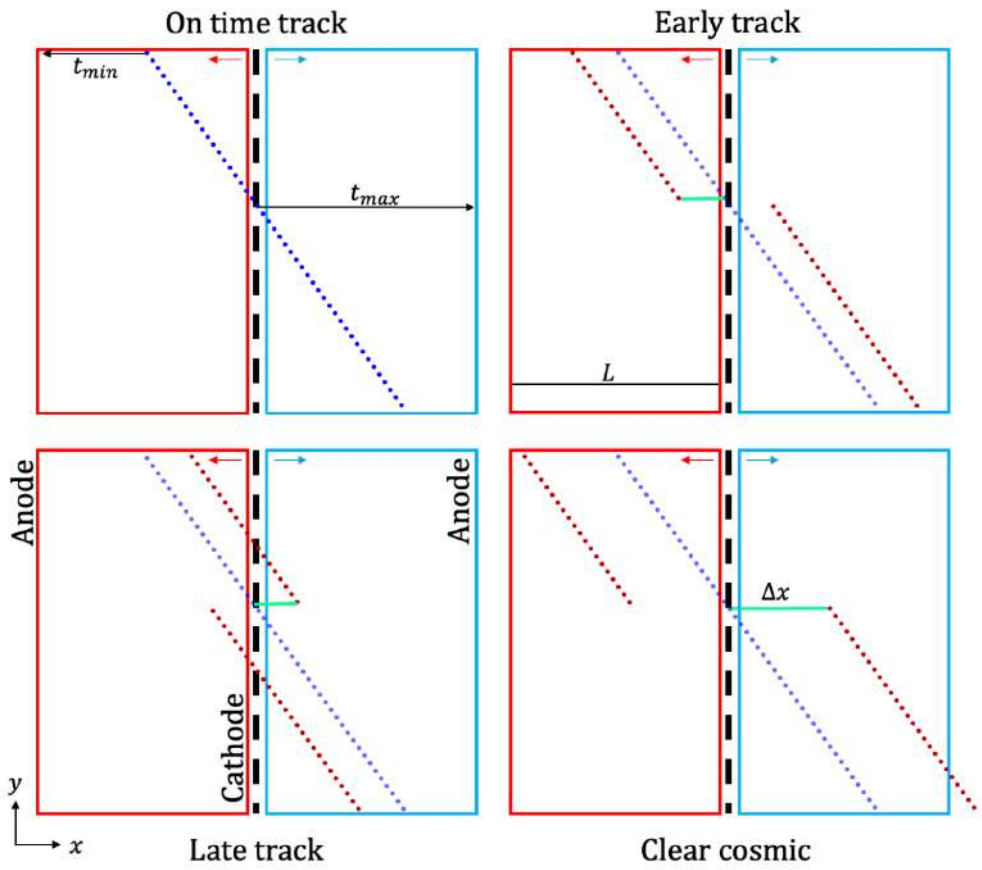

Figure 5.8: A representation of the different kinds of tracks and corresponding signal in the TPC.

- the t_0 correction applied by the stitching algorithm is too large, indicating that the particle is not from the beam.

Hits from this tagged cosmic ray muons, called "clear cosmics", are removed from the data to simplify the reconstruction of neutrino interactions by the PandoraNu.

5.3.2 PandoraNu

The PandoraNu stage of the Pandora chain is designed to handle neutrino interactions in the presence of cosmic rays remnants not removed in the PandoraCosmic step. [88]. The same algorithms applied in the PandoraNu stage are used to form a three-dimensional representation of the interaction events from the filtered 2D cluster data. The 3D hits are then grouped into "*slices*"

based on their spatial proximity and direction, to separate neutrino interactions from residual cosmic ray remnants. Each slice is processed individually with specialized neutrino reconstruction algorithms to identify neutrino interaction candidates. The algorithm re-evaluates the 2D clusters using the same track-oriented clustering and topological association techniques used in the PandoraCosmic step, to create a list of possible 3D vertex candidates. The most likely neutrino interaction vertex is determined through a score-based selection process, which evaluates and ranks each candidate based on specific geometric and energy-related criteria. The 3D track reconstruction process is similar to the algorithm used for PandoraCosmic. While the main goal is to trace the path that particles took through the detector, primary electromagnetic showers, generally due to electrons and photons, are also identified and reconstructed in PandoraNu. 2D shower-like clusters are matched across readout planes to form a complete 3D representation of the shower. Using a Boosted Decision Tree (BDT) algorithm, each particle is classified as either track-like or shower-like. The classification process is finally refined by picking up any small, unassociated clusters left out in earlier steps and parent-daughter relations between particles are defined. In this last step the reconstruction process organizes particles around the 3D neutrino vertex, building a particle hierarchy. Particle that directly result from the neutrino interaction are classified as primary particles, while those resulting from interactions or decays of primary particles are classified as secondary particles. The final output of each slice's reconstruction is a single reconstructed neutrino particle, with an internal hierarchy that represents the flow of the neutrino interaction. The different stages of Pandora pattern recognition chain are schematically represented in Figure 5.9 [89].

5.4 ICARUS Monte Carlo Simulation

The analysis performed in this thesis was performed on Monte Carlo (MC) simulated data, which use random sampling to model the expected kinematics of particles, and their final state based on theoretical models of particle cross sections. The simulation process in ICARUS uses LArSoft to generate the events under study, and can be summarized with the following steps:

- particle flux simulation;
- particle propagation and interaction;
- detector response simulation.

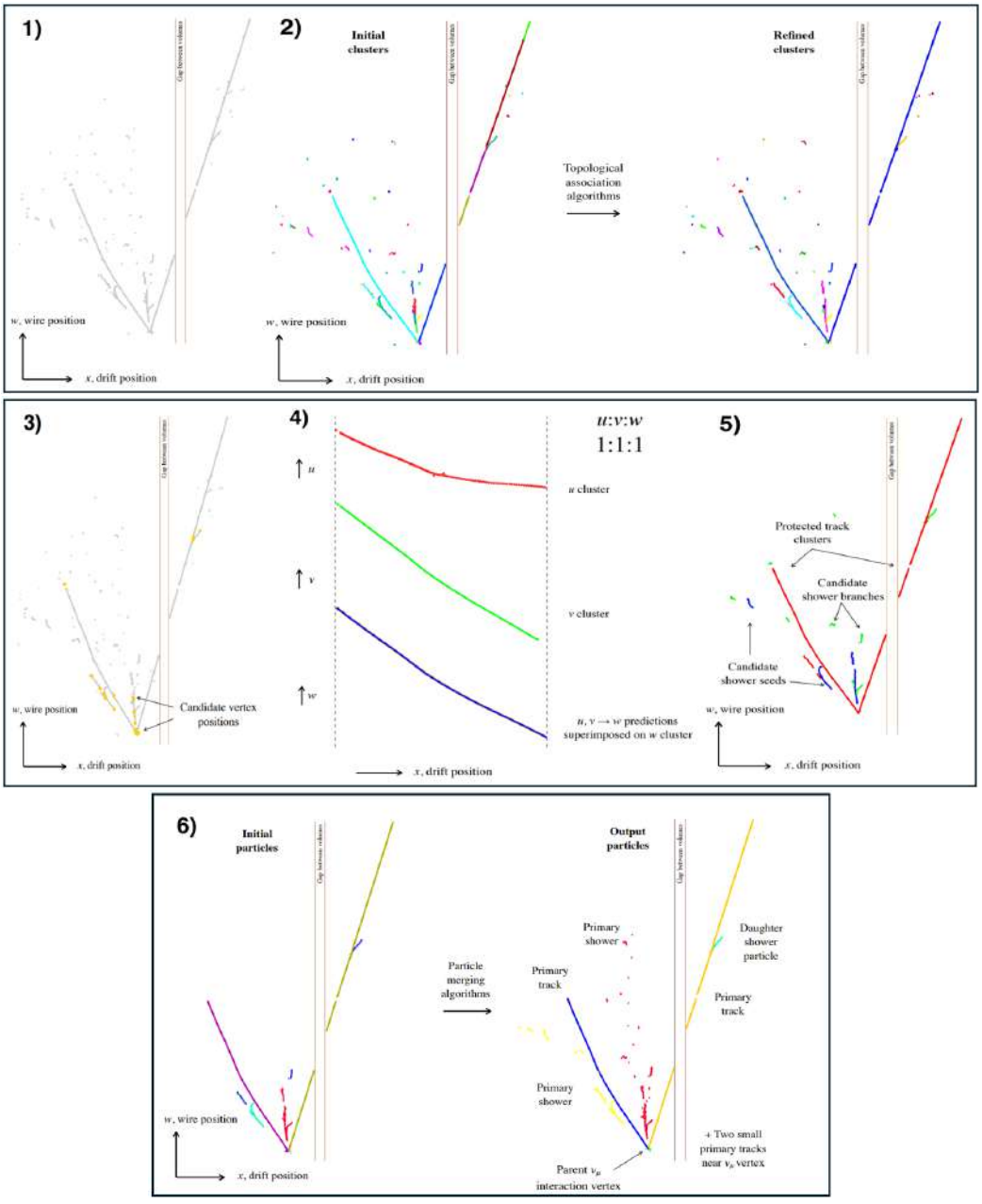

Figure 5.9: Illustration of the main stages of the Pandora pattern recognition chain: (1) Input Hits; (2) 2D track-like cluster creation and association; (3) 3D vertex reconstruction; (4) 3D track reconstruction; (5) Track/Shower separation; (6) 2D and 3D particle refinement and event building.

Initially the expected distribution of particles, such as cosmic ray and neutrinos, is simulated. As mentioned in Section 4.1.3 ICARUS uses CORSIKA to generate cosmic events, like air showers created by high-energy cosmic particles, based on the magnetic field components specific to a given geographic location [68]. Particles are tracked through the atmosphere until they interact with air nuclei or decay. For ICARUS, the focus is on simulating cosmic protons. Neutrino fluxes are modeled using data-driven MC approaches based on the specific beam characteristics (see Sections 2.2 and 2.3) and external hadron-production measurements. In this case the simulation of the passage of particles through matter uses GEANT4 [90] toolkit. Each generated particle (MCParticle or "true particle") type is identified by the PDGID, a unique code assigned using the Particle Data Group Numbering Scheme. Moreover, each MCParticle generated in each neutrino or cosmic event is assigned with a unique identification number, called G4ID (Geant4 ID). Once the particles are generated, the next step is to simulate their propagation toward the detector and their interactions. This involves tracking the particles as they travel through and eventually interact with the detector materials and the argon nuclei. ν-Ar interactions are simulated using GENIE (Generates Events for Neutrino Interaction Experiments) [91]. This open-source ROOT-based MC Generator can model neutrino interactions with different nuclear structures over a wide energy range, from 1 MeV to 1 PeV. A `MCNeutrino` object is generated in LArSoft, providing information about the neutrino interaction and the kinematics of any secondary particles produced. The propagation of these particles, generated from interactions of neutrinos or cosmic rays with liquid argon, is simulated using GEANT4 . Each daughter particle is tracked in its path through LAr, and their energy deposits are recorded at every step. A `SimChannel` object is created to store the information about the electrons deposited on a single TPC readout channel, where also all the detector effects on the drifted ionization electrons and inefficiencies are simulated. A `SimPhoton` object is generated to contain the information of all photons reaching a single optical detector readout channel. GEANT4 calculates also the positions and energy deposits of charged particles in each plastic scintillator bar of the CRT, storing this data in an `AuxDetSimChannel` object. This information is then processed to simulate the signals recorded by the detector's subsystems. Finally the same Pandora reconstruction algorithms applied for the data are used to process simulated events.

5.5 Neutrino energy reconstruction

As mentioned in Section 3.5 ICARUS has been taking data with both BNB and NuMI beams with the goal of assessing the Neutrino-4 oscillation hypothesis in the same baseline over energy range (L/E $\sim$ 1-3 m/MeV), but collecting $\sim$ hundred times more energetic events. The ν_μ disappearance channel is being studied with neutrino events collected with the BNB, focusing on quasi-elastic ν_μCC interactions fully contained. These are required to have a single muon and at least a proton existing from the same interaction vertex and with all tracks stopping inside the active LAr. As neutrinos interact weakly and are not electrically charged they leave no ionization trace in liquid argon, but often their product do, and it is by these that the original neutrino flavour, interaction point and energy can be inferred. These are necessary to precisely infer oscillation parameters, for which it is mandatory to measure the neutrino energy. In this context it is crucial to measure the energy loss of charged particles traveling through a material. This can be described generally as the sum lost due to interaction with the material's electrons and the energy dissipated through radiative processes. Muon energy loss in the kinematic regime relevant to ICARUS is primarly by ionization. The mean energy loss for unit length, also called linear stopping power, is given by the Bethe-Bloch formula an its corrections δ [92]:

$$-\left\langle \frac{dE}{dx} \right\rangle = \rho \cdot K z^2 \frac{Z}{A} \frac{1}{\beta^2} \left[\frac{1}{2} \ln \frac{2 m_e c^2 \beta^2 \gamma^2 T_{max}}{I^2} - \beta^2 - \frac{\delta(\beta\gamma)}{2} \right] \tag{5.5}$$

where K is a constant, z is the charge number ($Q = ze$), Z is the atomic number and A the atomic mass of the material (argon), T_{max} is the maximum kinetic energy which can be imparted to a free electron in a single collision, I is the mean exitation energy, ρ is the mass density and the δ factor is the density correction. This equation is only valid in the region $0.1 \leq \beta\gamma \leq 1000$, with an accuracy of a few percent. As Equation 5.5 describes the relation between particle momentum and its mean energy loss per particle path,it can be integrated to find the Continuous Slowing Down Approximation (CSDA) [93] range R for a particle that loses energy only through ionization and excitation:

$$R(E) = \int_{E_0}^{E} \left[\frac{dE}{dx} \right]^{-1} dE \tag{5.6}$$

where E_0 is sufficiently small that the result is insensitive to its exact value. This expression relates the path traveled by a particle in a medium with its momentum. This is particularly useful because when a particle stops inside

the ICARUS detector, the range traveled inside can be measured and converted to kinetic energy. This can be done by using the reference tables of stopping power contributions and CSDA ranges found in [93]. Finally the momentum can be obtained as $p = \sqrt{K^2 + 2KM}$, where K is the kinetic energy and M is the particle mass. In practice, this comes in hand when trying to estimate the neutrino energy, that assuming a quasi-elastic interaction and a struck nucleon at rest, can be estimated as the sum of the energy of the outgoing particles from the interaction

$$E_{\nu}^{vis} = E_{\mu} + \sum E_p - M_N, \tag{5.7}$$

where muon and proton energies are computed from range-based energy reconstruction, where the range is the ionization trace left in liquid argon by these particles. This estimate only accounts for the "visible" energy, nucleon binding energy and any energy carried by outgoing neutrons is not accounted for.

However this estimate is possible and accurate when the range, and so the particle path inside the detector is correctly reconstructed.

5.6 Tracks split

Both in real data and MC simulated data detector inefficiencies (tracks can be split across gaps in the detector instrumentation) and reconstruction issues can cause particle ionization traces to result split after the reconstruction, leading to an erroneous interpretation of the events occurred in the TPC. The goal of this thesis is to propose a solution to this problem, with an algorithm that is able to joint together the segments belonging to the same particle track, a practice here called "stitching". At detector level the most common known reasons of track splitting, caused by missing hits that weren't accounted for at reconstruction level or that Pandora wasn't able to account for stitching (joint together the segments belonging to the same particle track) the divided tracks segments, are:

- malfunctioning channels, as it is known that a set of 32 wires is disconnected in one of the TPCs;
- the presence of the cathode plane;
- hanging cables in the West Cryostat;
- electric field distorsions, produced by the fact that the Induction 1 plane is made by two sets of wires joint in the middle of the plane, with a few cm wide region not equipped with them.

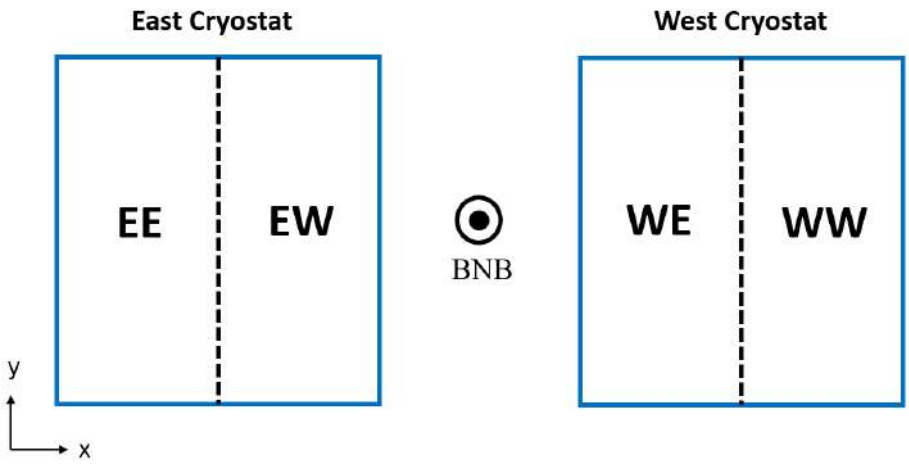

Figure 5.10: Scheme illustrating the TPCs labelling. The first letter identifies the specific cryostat unit, while the second letter denotes its position on the cryostat, either western or eastern.

For simplicity in the following figures TPCs are labeled with two letters, the first indicating the cryostat and the second the TPC inside the cryostat, for instance WE TPC is the East TPC of the West cryostat (see Figure 5.10). For each T300 module, the width (3.6 m) is labeled as x-axis, the height (3.9 m) as y-axis, while the lenght (19.6 over the BNB direction) as z-axis with the middle point fixed as the origin of the z-axis (z=0). Figure 5.11 shows the start and end hit points of reconstructed tracks in the WW cryostat, using around $\sim$ 250,000 tracks collected during Run2, where the presence of an accumulation of points due to the hanging cables is clearly visible in the top right part of the TPC. The typical distortion that a track sufers when crossing the z = 0 surroundings is shown Figure 5.12, where a muon track produced by a neutrino interaction is visible in the Collection plane [68].

These problems however are not simulated and therefore are not present in the MC simulated data reconstruction, where tracks splitting is mainly due to the presence of the cathode plane, which is included in the simulation. An example is shown in Figure 5.13 [88], where the proton track presents some missing hits. In Figure 5.14 the start points and end points of $\sim$ 30,000 MC muons fully contained tracks, generated from ν_μCC interactions, are represented in the XZ view of ICARUS cryostats (view from the top). Accumulations are visible around the cathode plane.

Before going to the following section is important to remember the terminology of slice, with which we refer to a group of reconstructed particle objects identifying an interaction (neutrino or cosmic) inside the TPC, and

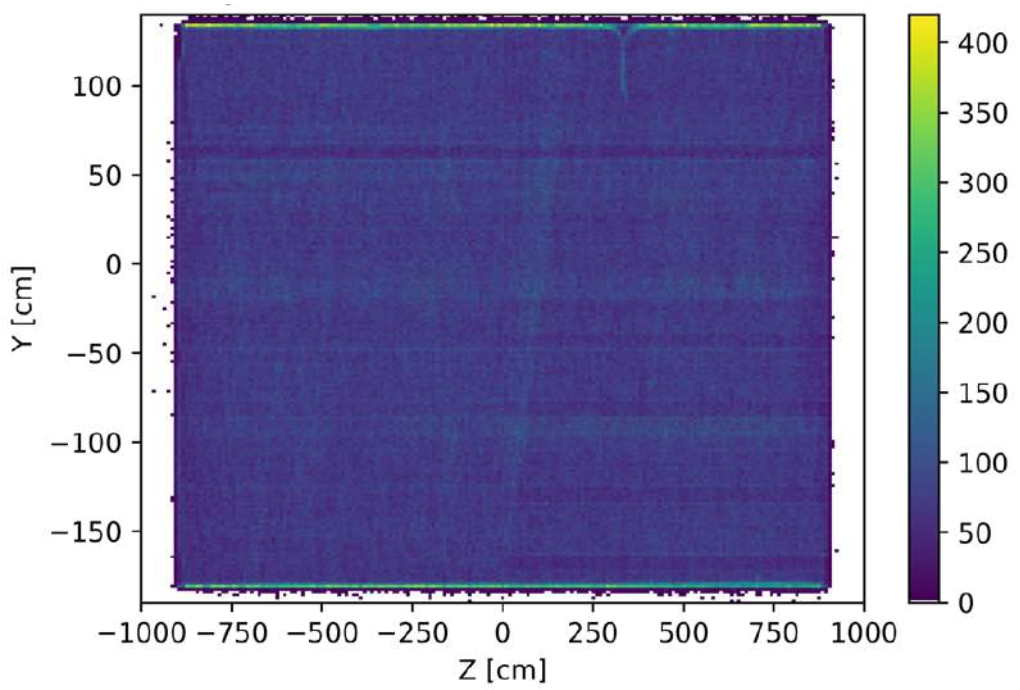

Figure 5.11: Start and end hit points of reconstructed tracks in the WW cryostat, where the presence of an accumulation of points due to the hanging cables is visible.

PFP, referring to single reconstructed particles.

5.7 Data analysis

The data analysis I developed is divided in the following steps:

- select fully contained cathode crossing muons tracks from ν_μCC interactions and identify split tracks;
- develop a stitching algorithm;
- evaluate improvement in the muon momentum estimate.

In this thesis I focused only on the analysis of MC simulated data of BNB neutrinos and cosmic rays from CAF files. The size of reconstructed data was reduced selecting only the variables needed for the analysis, namely those relative to the simulated particle MC truth and the reconstructed quantities of each particle trajectory inside the detector. These variables were stored

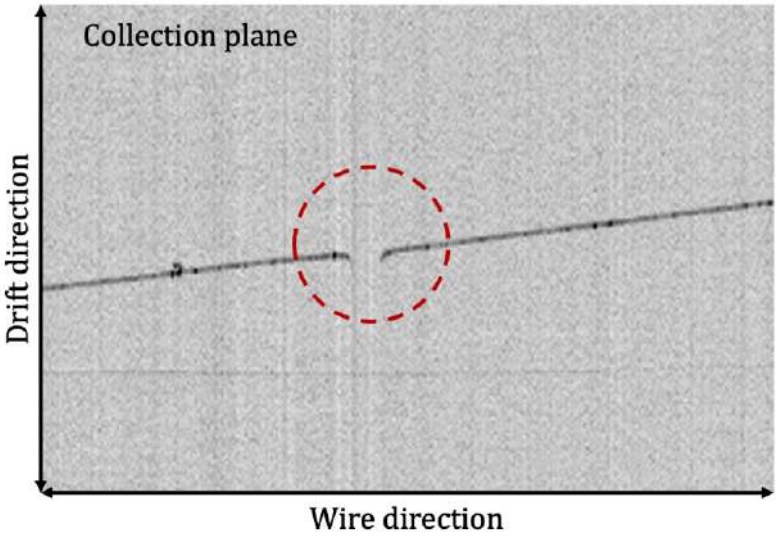

Figure 5.12: Muon track from a neutrino interaction affected by the distortion produced due to the split at z = 0 of Induction 1 wires.

in a *TTree object* where each entry is a true particle trajectory with the associated MC truth variables such as momentum, directions of start and end point of the trajectory, etc. For each true particle one or more reconstructed tracks were associated as described in the following section.

5.7.1 Event selection and classification

In order to identify a sample of split tracks for which apply the stitching algorithm, the association between the truth information on the generated particles and the corresponding reconstructed objects was exploited. After the pattern recognition algorithms are applied to simulated charge depositions, associations based on the amount of hits shared between the generated and reconstructed particles are made. Each reconstructed 2D hit is matched to a simulated particle responsible for the largest deposit of energy in the region of space and time covered by the hit [88]. From the hit level it is therefore possible to connect reconstructed objects with a known purity and completeness back to simulated neutrino interaction products. Single reconstructed tracks might contain hits from multiple true particles, either because a few hits are incorrectly assigned in regions where several true particles meet, or due to poor reconstruction performance merging together pieces of two independent interactions. Each reconstructed track has a list of associations to

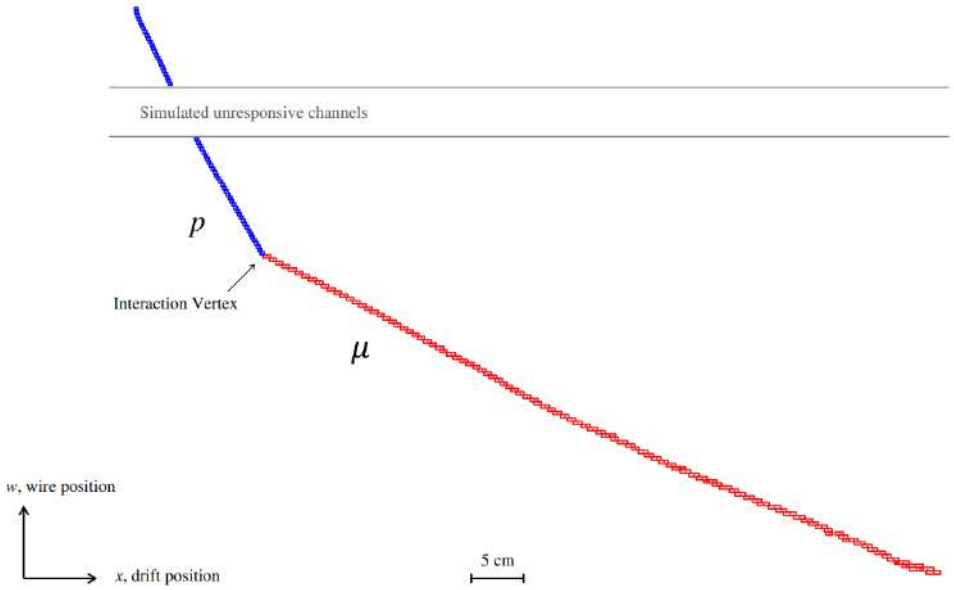

Figure 5.13: The reconstruction of a simulated 500-MeV CC ν_μ QE interaction. The target particles for the reconstruction are the muon and proton. A gap in the reconstructed proton track is observed due to the presence of malfunctioning channels, which are included in the simulation.

true particles, identified by their G4ID, ordered from highest to lowest energy contribution. Events with a correct reconstruction should match exactly one reconstructed particle to one true particle. However due to the mentioned problems, it can happen that a MCParticle trajectory is reconstructed with a multiplicity of segments that Pandora recognizes as multiple different particles, that will be partially matched to the MCParticle. We call here the number of tracks matched to a single MCParticle as "multiplicity".

For each true particle the reconstruced track with the same G4ID and with the highest energy from the matched hits was selected to identify the slice of neutrino interaction. Thus, all the reconstructed tracks in that slice with the same G4ID were associated to the true particle. An initial sample of $\sim$ 240000 true muons from ν_μCC interactions was matched with a total of $\sim$ 600000 reconstructed tracks.

The sample was reduced further, selecting cathode crossing true muons, since the presence of the cathode is one of the causes of track split. Moreover, only true muons whose trajectory and matched reconstructed tracks are fully contained within one of the cryostats were selected, in order to be able to compute the momentum from the range. A trajectory is contained if its first and last points are within 5 cm from each wall of the cryostat. The

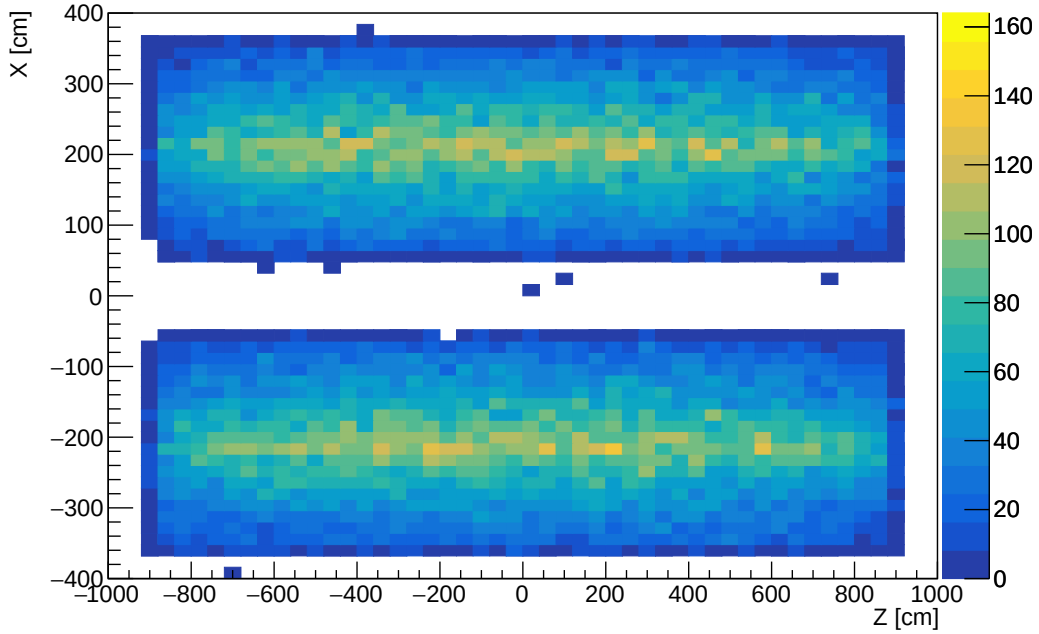

Figure 5.14: XZ view of ICARUS cryostats representing start and end points of simulated muon tracks.

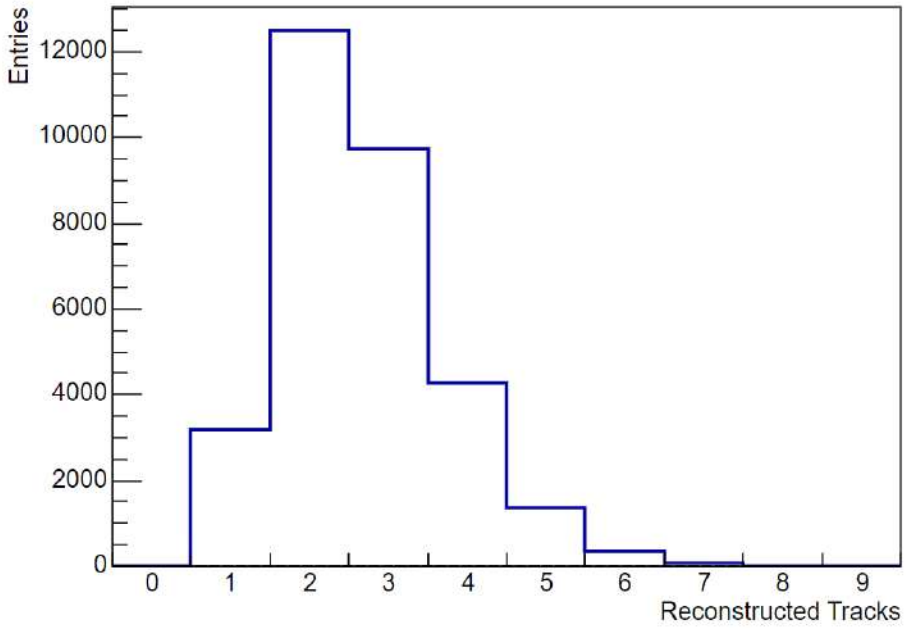

Figure 5.15: Multiplicity of reconstructed tracks for the 31,000 true muons samples.

new subsample is composed by $\sim$ 31,000 true muons, with $\sim$ 84,000 matched tracks. In Figure 5.15 the multiplicity of reconstructed tracks for this subsample is shown, where it is visible that most of the MCParticles, $\sim$ 6000, have 2 matched tracks in the slice. On the other hand $\sim$ 3000 MCParticles are correctly reconstructed in a single track.

A visual display was developed to study and have a better understanding of the selected events. In Figure 5.16 and 5.17 two events are shown, where the true muon trajectory is represented with a black dashed line, while the correspondent reconstructed tracks are shown in red. In Figure 5.16 a true muon trajectory split in two tracks at the cathode in the West cryostat, i.e. with an x-coordinate at $\sim$ 210 cm, is visible. In Figure 5.17 a trajectory split in four segments where only three belong to the true particle is shown: inefficiencies in TPC reconstrucion resulted in a gap in correspondence of a fourth segment not collinear with the others.

Furthermore, as track's directions are relevant to identify tracks belonging to the same trajectory, these were characterized. The direction of the track at any given point is computed by Pandora by fitting a line through the hit and its neighboring points (projected onto 2D wire planes), using the slope of this fit to define the direction at that point. This information is stored in CAF

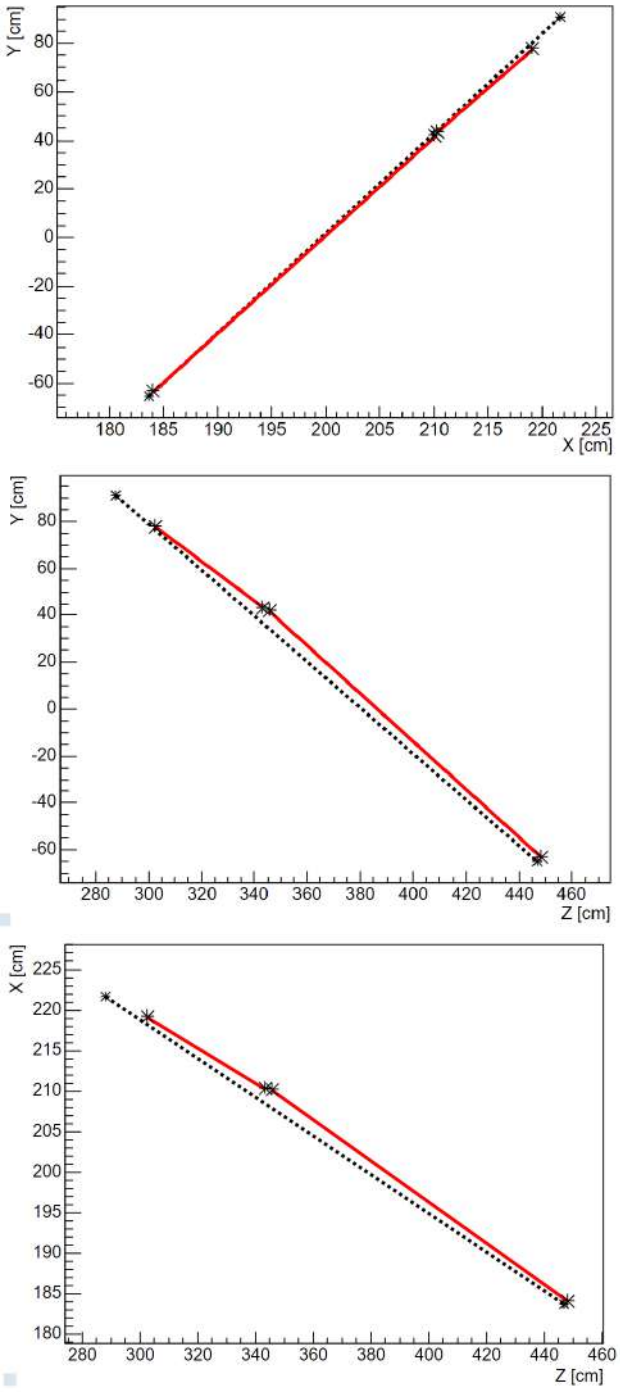

Figure 5.16: Visual display of the muon trajectory in the three different planes. The reconstructed track is represented in red, while the true track is in black. We can notice that the track split in two track at around $x \sim 210$ cm, i.e. the West cryostat.

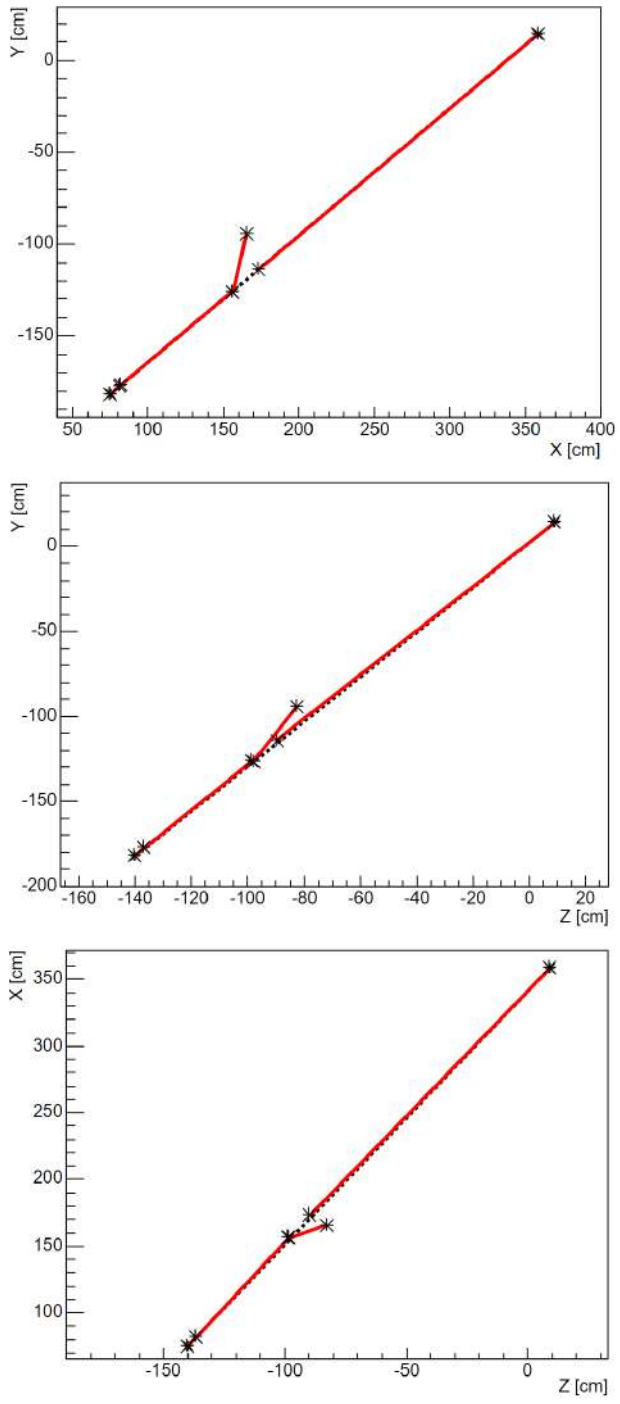

Figure 5.17: Visual display of the muon trajectory in the three different planes. The reconstructed track is represented in red, while the true track is in black. In this case, a trajectory split in 4 segments is evident.

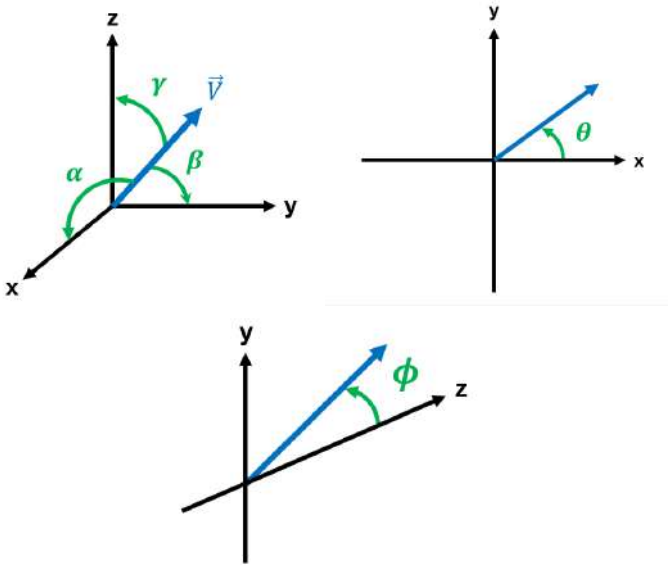

Figure 5.18: Representation of the utilised spherical coordinate system with respect to the cartesian system.

files as direction cosines, defined as the cosines of the angles between the track direction vector and the three positive coordinate axes (see left picture of Figure 5.18). Given that this information is not present for the MCParticles, the direction of a true particle's trajectory is computed by determining the vector from its starting to its ending position, and then normalizing this vector to unit length. Both for true particles and reconstructed track a different parametrization was used, with the spherical coordinates θ (polar angle) and ϕ (azimuthal angle), obtained from the direction cosines. These angles are shown in the center and right pictures in Figure 5.18.

From the selected subsample events can be classified in the following way, matching a true particle trajectory:

1. with a single reconstructed track;
2. with a long track, and a set of smaller tracks whose projection on the longest is overlaid to it;
3. with a long track, and a set of smaller tracks with a subset of them not overlaid on the longest.

In Table 5.1 the number of events per class is reported. In the following section, a stitching algorithm is proposed for tracks belonging to the third class of events.

	Class 1	Class 2	Class 3
Number of events	$\sim$ 3,000	$\sim$ 13,000	$\sim$ 15,000

Table 5.1: Number of events for each classification from the subsample of $\sim$ 31000 fully contained cathode crossing muons from ν_μCC interactions.

5.7.2 Stitching algorithm

The events belonging to *Class 1* and *Class 2* of Table 5.1 don't need to be stitched and in this case the range can be computed from the path of the longest track. A first geometrical cut was applied to separate events of *Class 2* from those of *Class 3*. For events of *Class 3* a stitching algorithm can be exploited in order to improve the reconstruction of the total path length of the muon in liquid argon and the momentum estimation from the range. To this aim an angular cut was applied to the *Class 3* events. To be stitched two tracks:

- must not overlap with each other;
- have to be collinear within a specified angle $\psi_{threshold}$ (collinearity threshold).

The algorithm stitches only the two longest tracks satisfying these conditions, meaning that a new value is created for the length of the reconstructed track, which is computed as:

$$L_{stitched} = L_1 + L_2 + L_{gap} \tag{5.8}$$

where L_1 is the longest track length, L_2 is the track length of the second longest track passing both cuts, and L_{gap} is the distance between the two closest points of the tracks. The distribution of the distance between the two closest points of the tracks that are stitched is shown in Figure 5.19, while the distribution of the length of the second longest track is reported in Figure 5.20.

Each true muon in the sample is analysed in the following way: if it has more that one matched reconstructed track, these are sorted by their length. For all the tracks starting from the second longest, is checked if they overlap with the longest track. The start and end points are projected onto the longest track's path checking if these points lie within its boundaries. If an overlap is detected, the corresponding track is flagged and the next is checked. If all the tracks are overlapped, the event belong to *Class 2* and the muon track cannot be stitched.

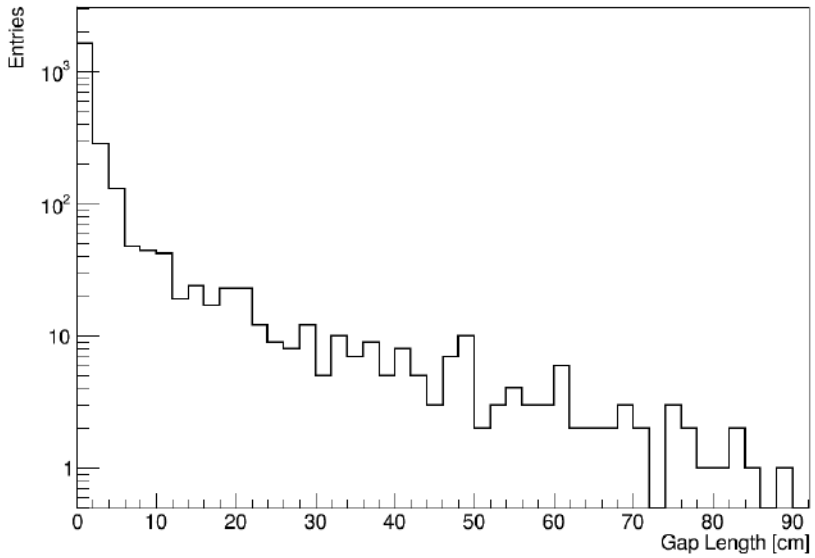

Figure 5.19: Distribution of the Gap Lenght, i.e. distance between the two closest points of the tracks that are stitched.

When at least a track is not overlapped, the event is classified as *Class 3* and an additional angular cut is applied. In particular, if the angle ψ between the two vectors representing the directions of the longest track and of the first track that passed the previous cut is within a specified threshold $\psi_{threshold}$ the two tracks are collinear and the path length is computed according to the Equation 5.8.

5.8 Results

In this section the optimal cut on the angle ψ which minimize the resolution on the muon momentum is studied. As mentioned in Section 5.5, the momentum can be estimated from the track range. In particular, the distribution of residuals $(p_{reco} - p_{true})/p_{true}$ bewteen the reconstructed and the momentum of the true muon is calculated for the events of Class 3. If no cut is applied on the angle ψ the reconstructed momentum is calculated from the length of the longest track, while for the events that surived the angular cut the reconstructed momentum is computed both from the range obtained with Equation 5.8 and from the longest track length. In Figure 5.21 the fraction of stitched muon track over the total number of true muons as a function of the ψ angle is shown if no cut on the ψ angle is applied (green points) and if a cut is applied (blue points).

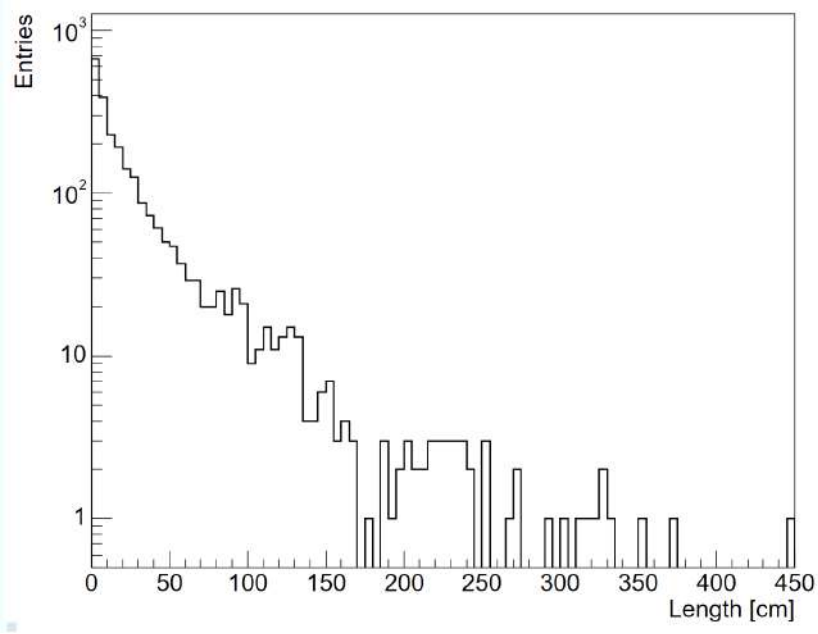

Figure 5.20: Distribution of the length of the second longest track.

The residual $(p_{reco} - p_{true})/p_{true}$ between the reconstructed momentum and the momentum of the true muon was computed for different cuts on the ψ angle. In Figure 5.22 comparisons of the residual distributions obtained estimating p_{reco} from the length of the stitched track (red) and from the longest track (blue), are shown for $\psi_{threshold}$ of 10°, 30° and 60° respectively. Is possible to see that for $\psi_{threshold}$=60° no improvement in the momentum reconstruction is observed when applying the stitching algorithm, and both the distributions show a narrow peak around zero, with the momentum that is underestimated if only the longest track length is used, while is overestimated when the stitch is applied. This is overestimation follows from the fact that the algorithm is stitching tracks with unrelated directions at large angles.

The momentum residual distributions were then computed for all the possible $\psi_{threshold}$ cuts, and the Root Mean Square (RMS) values were extracted. In Figure 5.23 the RMS values of the momentum residuals distribution is shown as a function of the cut on the ψ angle when the momentum is reconstructed from the longest track length (blue curve) and from the stitched track length (red curve). The algorithm therefore demonstrates promising results when applied to the events that survived the cut on the angle, showing an improvement in momentum.

However, in order to choose the optimal cut on the ψ angle the momentum residual distributions for the entire sample of Class 3 events were calculated.

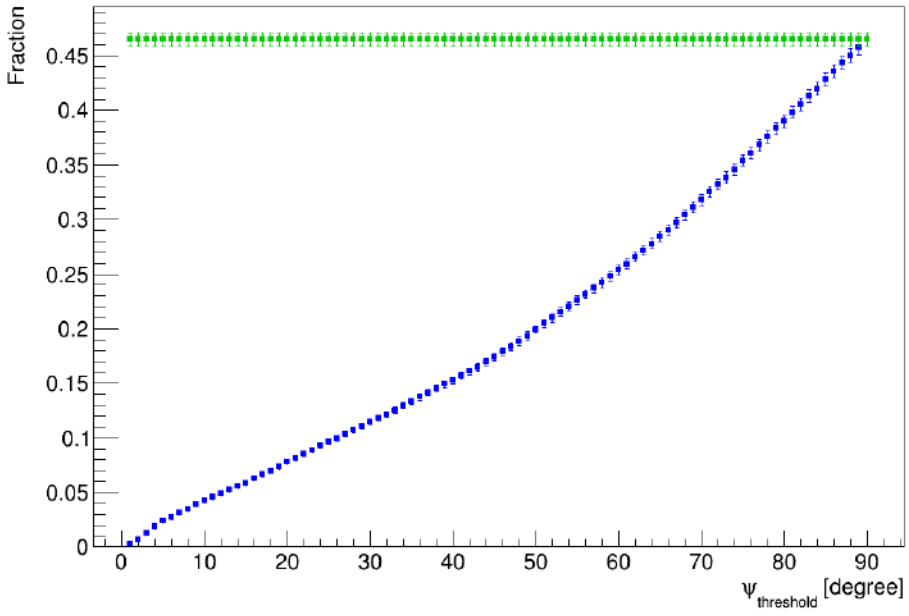

Figure 5.21: Fraction of thestitched muon track over the total number of true muons as a function of the ψ angle. In green, the distribution if no cut is applied. In blue, a cut on the ψ angle is applied.

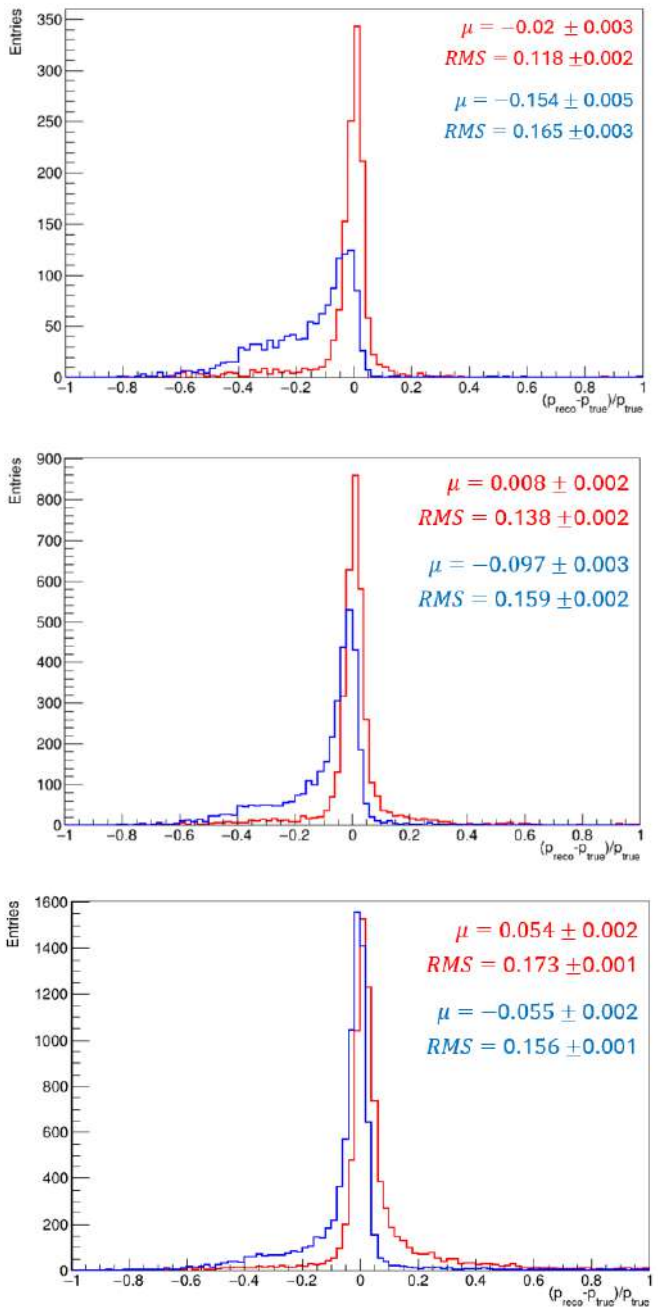

Figure 5.22: Comparisons of the residual distributions obtained estimating p_{reco} from the length of the stitched track (red) and from the longest track (blue), for $\psi_{threshold}$ of 10° (top), 30° (center) and 60° (bottom).

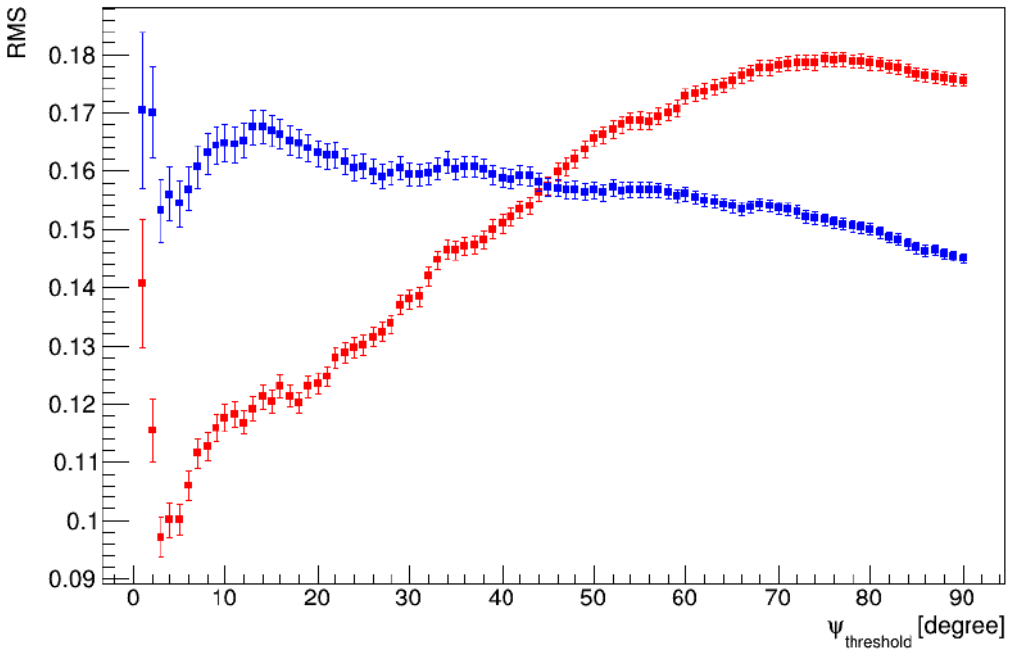

Figure 5.23: RMS values of the momentum residuals distribution shown as a function of the cut on the $\psi_{threshold}$ angle when the momentum is reconstructed from the longest track length (blue curve) and from the stitched track length (red curve).

At each cut on the ψ angle the momentum is reconstructed from the stitching algorithm equation if the two track are collinear within the threshold angle while is computed from the longest track length if the two track direction differ more than the threshold angle.

The objective is to determine if there is a global improvement in momentum resolution with respect to the baseline approach of using the longest track length to estimate the momentum for the entire sample of Class 3 events. To this end, an optimization criterion based on the RMS of momentum distributions obtained for different cut on the ψ angle has been employed. In Figure 5.24 the RMS of the momentum residual distribution are shown as a function of the cut on the threshold angle for the Class 3 events when reconstructing the range using the longest track length only (green points) and using the stitching algorithm if the two longest tracks are collinear within the threshold angle or the longest track length if the two track are not.

A minimum around 20 degrees for the RMS is found, showing an improve-

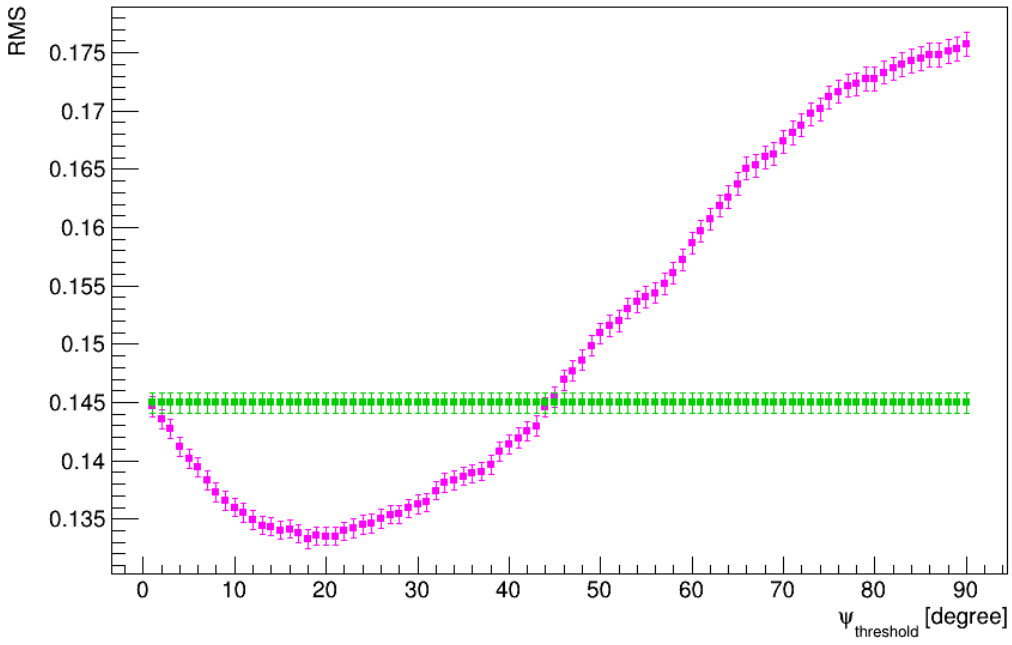

Figure 5.24: Comparison between the outcomes for the population always using the longest track (green points) and the case where stitched track lengths are used for estimation when applicable (magenta points). A minimum around 20 degrees is visibile.

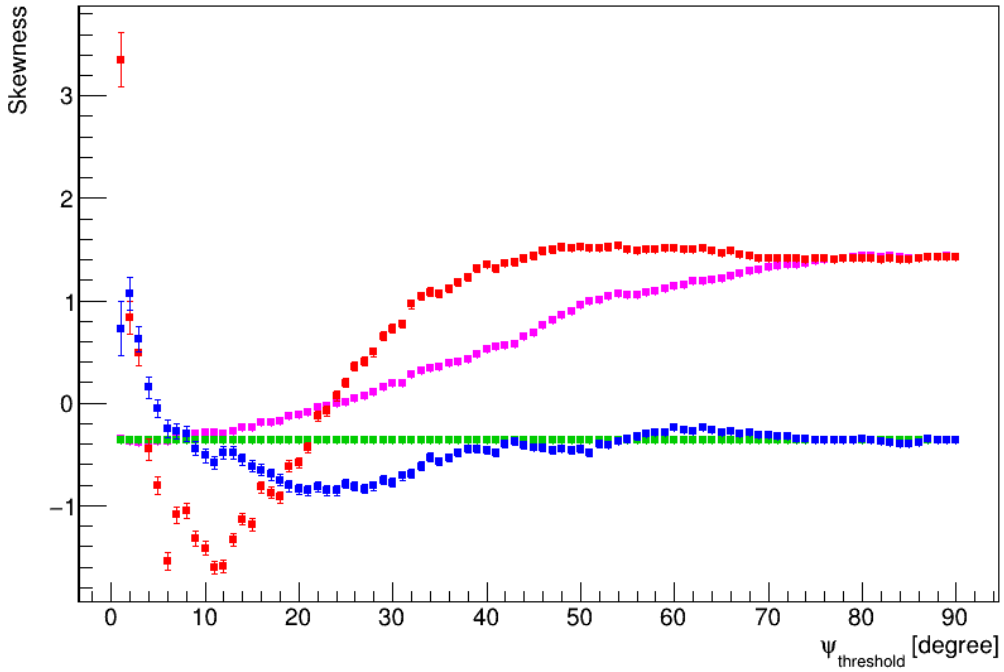

Figure 5.25: The skewness for the two global distributions (green and magenta) and overlaid distributions of values when only the Class 3 events are considered.

ment of ∼1% with respect to the momentum residual distribution. Other figure of merit were evaluated in order to choose the optimal cut on the threshold angle. For example, in Figure 5.25 the skeweness, i.e. a measure of the asymmetry of a distribution, is shown as a function of the cut on the threshold angle. The red and blue curves correspond to events that survived the angular cut and for which the range was computed from the stitching algorithm or from the longest track length, respectively. The green curve corresponds to the entire sample of Class 3 events for which the range was computed from the longest track length only. The magenta curve refers to Class 3 events where the range is obtained from the stitching algorithm or from the longest track length depending whether the event survived to the cut on the threshold angle or not. At $\sim$ 20 degrees the magenta distributions tend to zero, meaning that the momentum residual bias distribution is symmetric. In Figure 5.26 the bias, namely the mean value of the momentum residual distribution is shown. At $\sim$ 20 degrees, the $(p_{reco} - p_{true})/p_{true}$ distribution when the momentum is reconstructed from the stitching algorithm has a bias value that is almost zero.

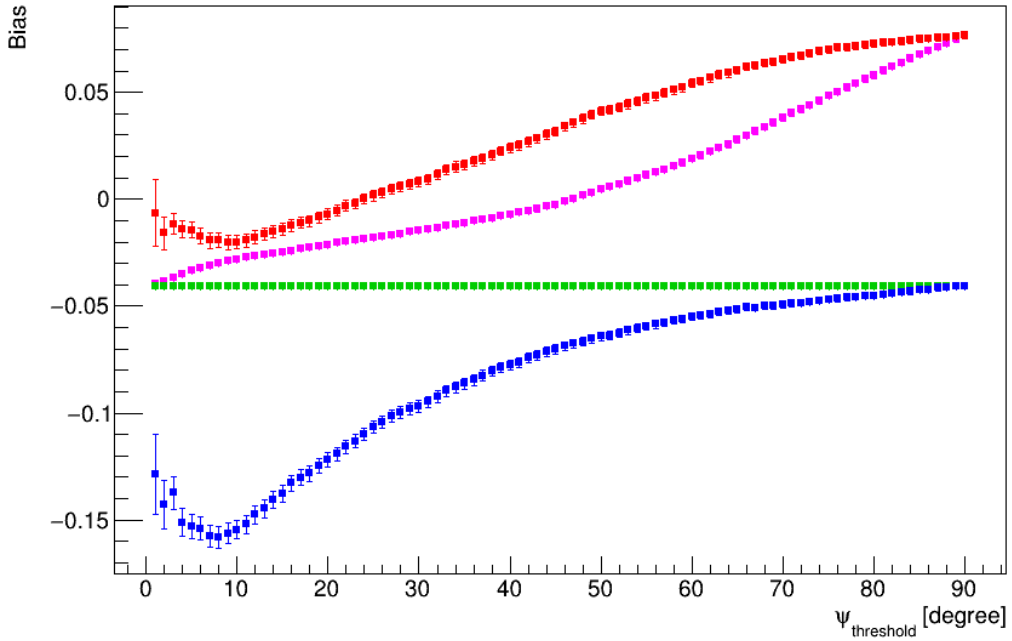

Figure 5.26: Bias values for the two global distributions (green and magenta) and overlaid distributions of values when only the Class 3 events are considered.

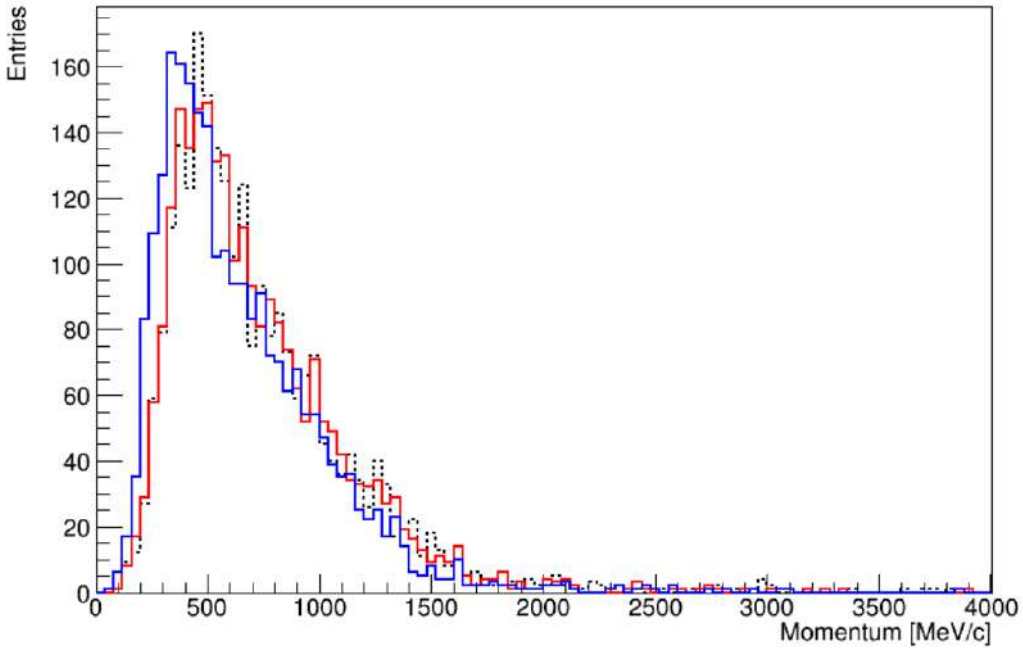

Figure 5.27: Momentum distribution computed from the range evaluated with the stitching algorithm (red) for $\psi_{threshold}$=20°, compared with the true momentum distribution (black dashed line) and with the momentum distribution where the range is obtained from the longest track length (blue).

Applying the stitching algorithm with a collinearity cut at 20 degrees, the momentum distribution is computed (see Figure 5.27) from the range evaluated with the stitching algorithm (red) and is compared with the true momentum distribution (black dashed line) and with the momentum distribution where the range is obtained from the longest track length (blue). A qualitative agreement between the red and the black momentum distributions can be observed. The momentum residual distribution obtained with a cut at 20 degrees is shown in Figure 5.28 for the case of applying the stitching algorithm (red) and the longest track length method (blue).

The same distributions are shown for the entire sample of Class 3 events in Figure 5.29 and Figure 5.30.

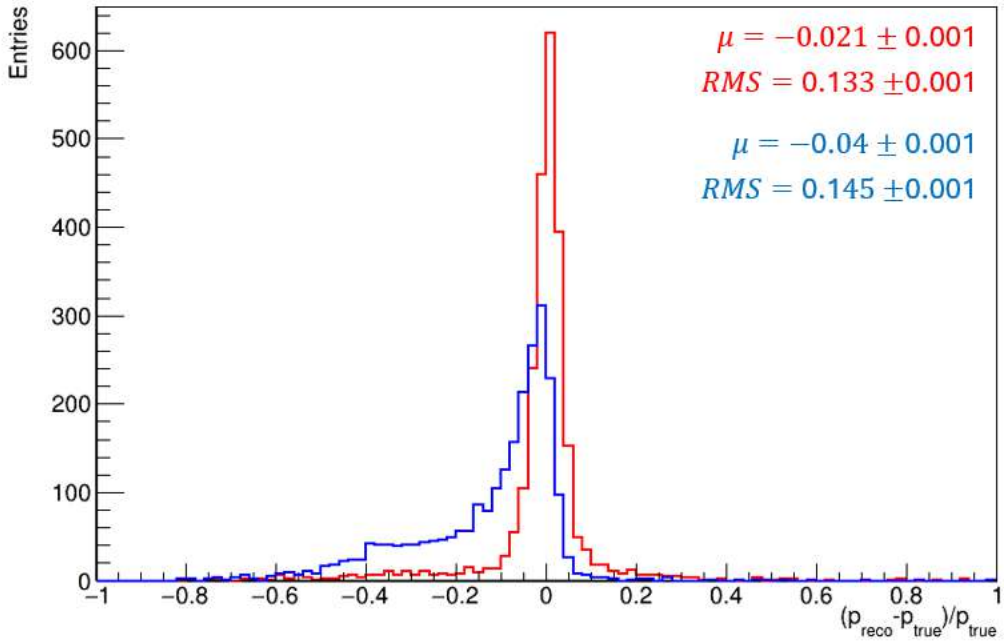

Figure 5.28: Momentum residual distribution with a cut at $\psi_{threshold}$=20°, when the stitching algorithm is applied (red) and computed from the longest track length (blue).

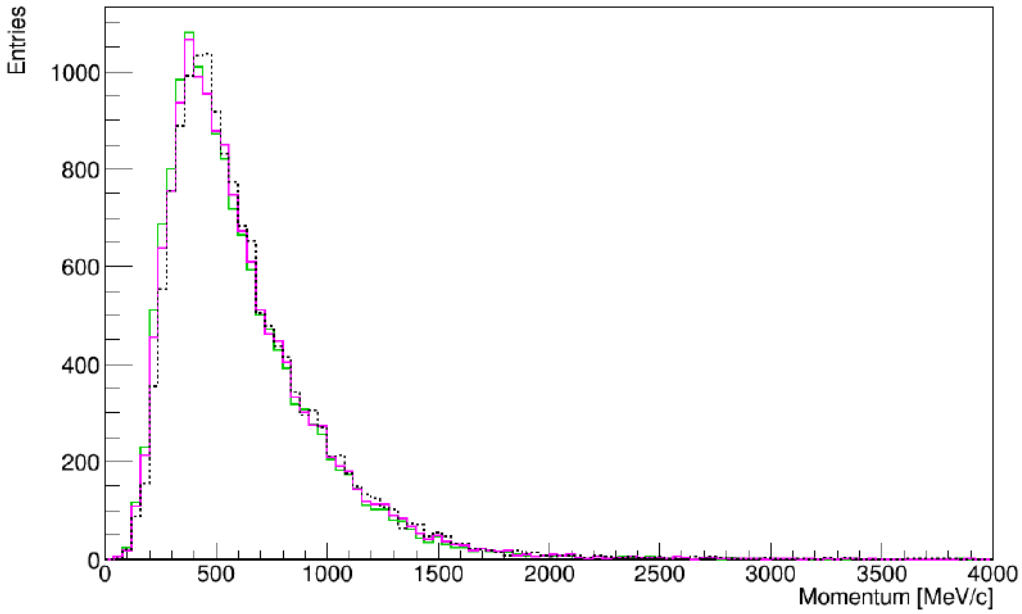

Figure 5.29: Momentum distribution computed from the range, evaluated for Class 3 events. The range is computed from the stitching algorithm or from the longest track length depending whether the event survived to the cut at $\psi_{threshold}$=20° (magenta), from the longest track length only (green) and momentum distribution of the true muons (black dashed line).

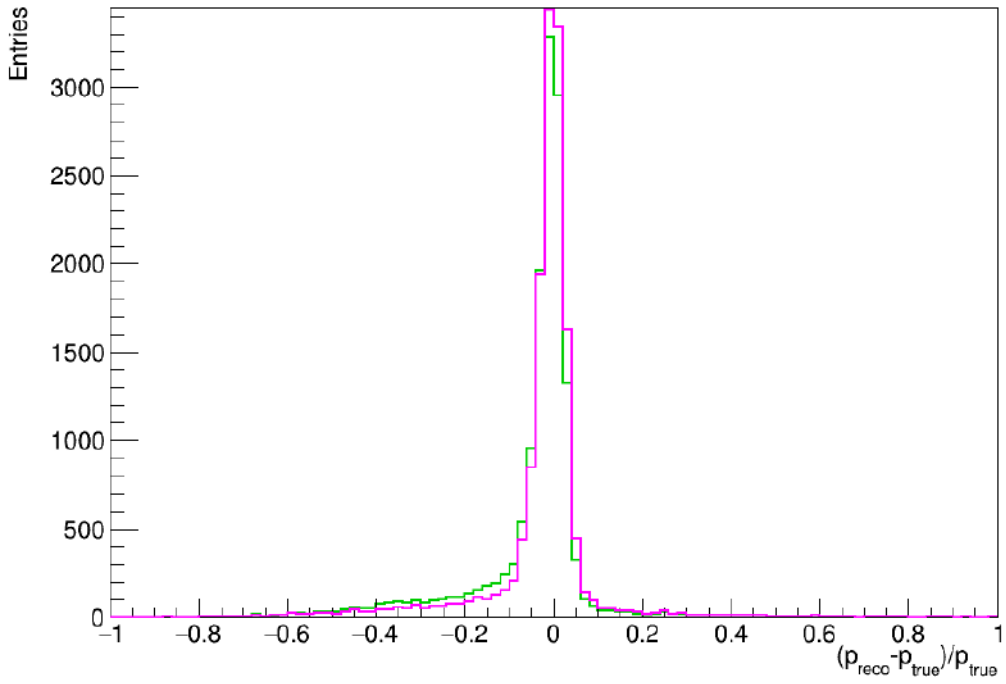

Figure 5.30: Momentum residual distribution evaluated for Class 3 events, with a cut at 20 degrees (magenta) and computed from the longest track length only (green).

Conclusions

The Short-Baseline Neutrino (SBN) program at Fermilab aims to investigate several anomalies that deviate from the predictions made by the standard three-neutrino oscillation model, suggesting the possible existence of a sterile neutrino.

ICARUS is a detector located at the SBN far site, 600 m from the Booster Neutrino Beam proton target and is composed by three subsystems: i) a 470 t Liquid Argon Time Projection Chamber; ii) a photon detection system in LAr, and iii) a Cosmic Ray Tagger (CRT) based on scintillators.

This thesis work primarily focused on calibrating the Top Cosmic Ray Tagger and enhancing track reconstruction in the Time Projection Chamber.

The calibration of the Top CRT is essential to ensure the uniformity of the detector's response. By estimating and equalizing pedestal and gain values for each CRT channel, the calibration aims to maintain consistent detector performance over time.

The second major focus was on enhancing track reconstruction accuracy within the TPC. Hardware-related issues and inefficiencies at the reconstruction level often lead to single particle trajectories being mistakenly segmented into multiple tracks. To address this, a track stitching algorithm was developed and implemented. The proposed track stitching algorithm, validated through Monte Carlo simulations, aims to improve track reconstruction accuracy and momentum estimation. The analysis showed that applying a 20-degree collinearity cut in the algorithm optimizes momentum estimation, significantly reducing bias (up to 15%) and slightly improving resolution ($\tilde{1}$%) for about 10% of the track sample.

Overall, the advancements in CRT calibration and TPC track reconstruction can contribute to the robustness and precision of the ICARUS detector's performance, enabling more accurate exploration of neutrino oscillations and the potential existence of sterile neutrinos.

Bibliography

[1] W. Pauli. Wissenschaftlicher briefwechsel mit bohr, einstein, heisenberg. 259, 1930.

[2] E. Fermi. *Nuovo Cim.*, 11:1, 1934.

[3] C. L. Cowan et al. *Science*, 124:103, 1956.

[4] F. Reines and C. L. Cowan. *Nature*, 178:446, 1956.

[5] B. Pontecorvo. volume 1 of *Cambridge Monographs on Particle Physics, Nuclear Physics and Cosmology*. 1991.

[6] M. Goldhaber, L. Grodzins, and A. W. Sunyar. *Phys. Rev.*, 109:1015, 1958.

[7] L. D. Landau. On the conservation laws for weak interactions. *Nucl. Phys.*, 3:127, 1957.

[8] T. D. Lee and C. N. Yang. Parity nonconservation and a two component theory of the neutrino. *Phys. Rev.*, 105:1671, 1957.

[9] A. Salam. On parity conservation and neutrino mass. *Nuovo Cim.*, 5:299, 1957.

[10] S. Weinberg. A model of leptons. *Physical Review Letters*, 19:1264, 1967.

[11] S. L. Glashow. *Nucl. Phys.*, 22:579, 1961.

[12] A. Salam. In N. Svartholm, editor, *Proc. of the 8th Nobel Symposium on "Elementary Particle Theory, Relativistic Groups and Analyticity"*, page 367, 1968.

[13] G. Danby et al. *Phys. Rev. Lett.*, 9:36–44, 1962.

[14] D. Decamp et al. *Phys. Lett.*, B231:519, 1989.

[15] K. Kodama and others (DONUT Collaboration). *Phys. Lett. B*, 504:218, 2001.

[16] C. Quigg. *Gauge Theories of the Strong, Weak, and Electromagnetic Interactions: Second Edition*. Princeton University Press, 2014.

[17] S. Pascoli. Neutrino physics. *CERN Yellow Rep. School Proc.*, 6:213–259, 2019.

[18] C. Giunti and C.W. Kim. *Fundamentals of Neutrino Physics and Astrophysics*. OUP Oxford, 2007.

[19] C. Giunti and T. Lasserre. ev - scale sterile neutrinos. *Annual Review of Nuclear and Particle Science*, 69:163–190, 2019.

[20] Y. Fukuda et al. *Phys.Rev.Lett.*, 81:1562, 1998.

[21] S. Bilenky. Neutrinos: Majorana or dirac? *arXiv:2008.02110*, 2020.

[22] E. Majorana. *Nuovo Cim.*, 14:171, 1937.

[23] R. N. Mohapatra and G. Senjanovic. *Phys. Rev. Lett.*, 44:912, 1980.

[24] P. Minkowski. *Phys. Lett.*, B67:421, 1977.

[25] T. Yanagida. Workshop on the baryon number of the universe and unified theories. 1979. Tsukuba, Japan, 13–14 Feb 1979.

[26] B. Pontecorvo. *Sov. Phys. JETP*, 6:429, 1957.

[27] B. Pontecorvo. *Sov. Phys. JETP*, 7:172–173, 1958.

[28] B. Pontecorvo. *Sov. Phys. JETP*, 26:984–988, 1968.

[29] G. Danby et al. *Phys. Rev. Lett.*, 9:36–44, 1962.

[30] Z. Maki, M. Nakagawa, and S. Sakata. *Prog. Theor. Phys.*, 28:870, 1962.

[31] B. T. Cleveland et al. *Astrophys. J.*, 496:505–526, 1998.

[32] J. Boger et al. The sudbury neutrino observatory. *Nuclear Instruments and Methods in Physics Research Section A: Accelerators, Spectrometers, Detectors and Associated Equipment*, 449(1):172–207, 2000.

[33] S. M. Bilenky, J. Hosek, and S. T. Petcov. *Phys. Lett. B*, 94:495, 1980.

[34] J. Schechter and J. W. F. Valle. *Phys. Rev. D*, 22:2227, 1980.

[35] G. Mention, M. Fechner, Th. Lasserre, Th. A. Mueller, D. Lhuillier, M. Cribier, and A. Letourneau. *Phys. Rev. D*, 83:073006, 2011.

[36] Th. A. Mueller et al. *Phys. Rev. C*, 83:054615, 2011.

[37] F. Kaether et al. *Phys. Lett. B*, 685:47, 2010.

[38] J. N. Abdurashitov et al. *Phys. Rev. C*, 73:045805, 2006.

[39] A. Aguilar et al. *Phys. Rev. D*, 64:112007, 2001.

[40] A. A. Aguilar-Arevalo et al. *Phys. Rev. D*, 79:072002, 2009.

[41] A. A. Aguilar-Arevalo et al. *Nuclear Instruments and Methods in Physics Research Section A*, 599:28–46, 2009.

[42] A.A. et al. Aguilar-Arevalo. Significant excess of electronlike events in the miniboone short-baseline neutrino experiment. *Physical Review Letters*, 121(22), November 2018.

[43] A. Serebrov et al. 2018.

[44] A. Serebrov et al. *Phys. Rev. D*, 104:032003, 2021.

[45] P. A. N. Machado, O. Palamara, and D. W. Schmitz. *Annual Review of Nuclear and Particle Science*, 69:363–387, 2019.

[46] M. Dentler et al. *Journal of High Energy Physics*, 2018(8), Aug. 2018.

[47] R. Acciarri et al. A proposal for a three detector short-baseline neutrino oscillation program in the fermilab booster neutrino beam, 2015.

[48] M. Bonesini. The short baseline neutrino program at fermilab, 2022.

[49] P. et al. Adamson. The numi neutrino beam. *Nuclear Instruments and Methods in Physics Research Section A: Accelerators, Spectrometers, Detectors and Associated Equipment*, 806:279–306, January 2016.

[50] Krishanu Majumdar and Konstantinos Mavrokoridis. Review of liquid argon detector technologies in the neutrino sector. *Applied Sciences*, 11(6):2455, March 2021.

[51] Carlo Rubbia. The liquid argon time projection chamber: A new concept for neutrino detectors. 1977.

[52] David R. Nygren. The time projection chamber: A new 4 pi detector for charged particles. 1976.

[53] R. et al. Acciarri. Design and construction of the microboone detector. *Journal of Instrumentation*, 12(02):P02017–P02017, February 2017.

[54] ICARUS Collaboration. Icarus at the fermilab short-baseline neutrino program – initial operation, 2023.

[55] C. Adams et al. Design and construction of the microboone cosmic ray tagger system. *Journal of Instrumentation*, 14(04):P04004, apr 2019.

[56] P. et al. Abratenko. First constraints on light sterile neutrino oscillations from combined appearance and disappearance searches with the microboone detector. *Physical Review Letters*, 130(1), January 2023.

[57] Gustavo Valdiviesso. Status of the short-baseline near detector at fermilab. page 184, 03 2022.

[58] Miquel Nebot-Guinot. Status of the short-baseline near detector at fermilab. *Physical Sciences Forum*, 8(1), 2023.

[59] B. Abi et al. Deep underground neutrino experiment (dune), far detector technical design report, volume i: Introduction to dune, 2020.

[60] M. Antonello et al. (ICARUS Collaboration). Search for anomalies in the ν_e appearance from a ν_μ beam. *Eur. Phys. J.*, C73:2599, 2013.

[61] Laura Pasqualini. Status and perspective of the icarus experiment at the fermilab short baseline neutrino program. page 020, 03 2024.

[62] M. Antonello et al. (ICARUS Collaboration). Experimental observation of an extremely high electron lifetime with the ICARUS-T600 LAr-TPC. *JINST*, 9 P12006, 2014.

[63] M. Antonello et al. (ICARUS Collaboration). Precise 3D track reconstruction algorithm for the ICARUS T600 liquid argon time projection chamber detector. *Advances in High Energy Physics*, 2013:260820, 2013.

[64] M. Antonello et al. (ICARUS Collaboration). Muon momentum measurement in ICARUS-T600 LAr-TPC via multiple scattering in few-GeV range. *JINST*, 12 P04010, 2017.

[65] C. Farnese (on behalf of the ICARUS Collaboration). Atmospheric Neutrino Search in the ICARUS T600 Detector. *Universe*, 5(1), 2019.

[66] B. Ali-Mohammadzadeh et al. (ICARUS Collaboration). Design and implementation of the new scintillation light detection system of ICARUS T600. *JINST*, 15 T10007, 2020.

[67] M. Bonesini et al. An innovative technique for TPB deposition on convex window photomultiplier tubes. *JINST*, 13 P12020, 2018.

[68] Maria Artero Pons. *Study of the reconstruction of ν_μ CC QE events from the Booster Neutrino Beam with the ICARUS detector*. PhD thesis, Universita di Padova, April 2024.

[69] Javier Serrano et al. The white rabbit project. 2009.

[70] Riccardo Triozzi. *Study of the trigger system performance of the ICARUS T600 detector at Fermilab exposed to the Booster and NuMI neutrino beams*. PhD thesis, Universita di Padova, 2022.

[71] B. Behera and the ICARUS collaboration. Cosmogenic background suppression at the icarus using a concrete overburden. *Journal of Physics: Conference Series*, 2156(1):pp 012 181, Dec. 2021.

[72] Francesco Poppi. *The cosmic ray tagger of the ICARUS detector: construction, commissioning and performances in the first physics run*. PhD thesis, Universita di Bologna, June 2023.

[73] Umut Kose et al. ICARUS: new voyage to sterile neutrino search in the Short Baseline Program. *PoS*, ICRC2021:1071, 2021.

[74] Francesco Poppi. The cosmic ray tagger system of the icarus detector at fermilab. *Proceedings of 41st International Conference on High Energy physics — PoS(ICHEP2022)*, 2022.

[75] *Kuraray Wavelength Shifting Fibers*.

[76] Francesco Poppi. *The cosmic ray tagger of the short baseline neutrino experiment at Fermilab*. PhD thesis.

[77] *Hamamatsu S13360-1350CS SiPM datasheet*.

[78] M. Auger et al. Multi-channel front-end board for sipm readout. *JINST, 11, P10005*, 2016.

[79] *A 32-channel front-end ASIC designed to readout silicon photomultipliers (SiPM) for scientific instrumentation application.*

[80] L. Pasqualini. Short-baseline neutrino oscillation searches with the icarus detector at fnal. *Nuclear Instruments and Methods in Physics Research Section A: Accelerators, Spectrometers, Detectors and Associated Equipment*, 1054:168465, 2023.

[81] D. Heck, J. Knapp, J. N. Capdevielle, G. Schatz, and T. Thouw. *CORSIKA: a Monte Carlo code to simulate extensive air showers.* 1998.

[82] R. L. Workman et al. Review of particle physics. *PTEP*, 2022:pp 520–527.

[83] R. Brun and F. Rademakers. *Nucl. Inst. and Meth. in Phys. Res.*, vol. A 389:pp 81–86, 1997.

[84] E.L. Snider and G. Petrillo. Larsoft: toolkit for simulation, reconstruction and analysis of liquid argon tpc neutrino detectors. *Journal of Physics: Conference Series*, 898(4):042057, oct 2017.

[85] *ROOT Reference Guide, TTree Class Reference.*

[86] C. Adams et al. Ionization electron signal processing in single phase lartpcs. part i. algorithm description and quantitative evaluation with microboone simulation. *Journal of Instrumentation*, 13(07):P07006, jul 2018.

[87] C. Adams et al. Ionization electron signal processing in single phase lartpcs. part ii. data/simulation comparison and performance in microboone. *Journal of Instrumentation*, 13(07):P07007, jul 2018.

[88] MicroBooNE collaboration. The pandora multi-algorithm approach to automated pattern recognition of cosmic-ray muon and neutrino events in the microboone detector, 2017.

[89] B. Abi et al. Deep underground neutrino experiment (dune), far detector technical design report, volume ii: Dune physics, 2020.

[90] Stefano et al. Agostinelli. Geant4-a simulation toolkit. *Nuclear Instruments and Methods in Physics Research Section A Accelerators Spectrometers Detectors and Associated Equipment*, 506:250, 07 2003.

[91] Costas Andreopoulos et al. The genie neutrino monte carlo generator: Physics and user manual, 2015.

[92] Fermilab and Alberto Marchionni. Muon energy loss in liquid argon. 2017.

[93] DONALD E. GROOM, NIKOLAI V. MOKHOV, and SERGEI I. STRIGANOV. Muon stopping power and range tables 10 mev–100 tev. *Atomic Data and Nuclear Data Tables*, 78(2):183–356, 2001.